Improved performance of an optically pumped mid-infrared acetylene-filled hollow-core fiber laser

by

Neda Dadashzadeh

B.S., University of Tehran, 2007
M.S., University of Tabriz, 2011

AN ABSTRACT OF A DISSERTATION

submitted in partial fulfillment of the requirements for the degree

DOCTOR OF PHILOSOPHY

Department of Physics
College of Arts and Sciences

KANSAS STATE UNIVERSITY
Manhattan, Kansas

2017

Abstract

The focus of this research is improving the pulse output energy of a mid-IR pulsed acetylene-filled Hollow-core Optical Fiber Gas LASer (HOFGLAS) system. Pump pulses and acetylene molecules interact with each other inside hollow-core photonic crystal fiber that effectively confines light and allows for strong gain. This results in lasing at 3.11 μm and 3.17 μm lines based on population inversion of acetylene molecules, which are optically pumped at rotational-vibrational overtones near 1.5 μm using 1 ns pulse duration from an optical parametric amplifier (OPA). This acetylene laser operates with no cavity mirrors because of a high gain in a single pass configuration. There are few laser sources in the mid-IR region while there are many applications for having a laser source in this range such as remote sensing, hazardous chemical detection, and breath analysis. This adds to the importance of the acetylene-filled HOFGLAS system. Some of the applications like remote sensing require high power. So, we moved toward power scaling this laser system by optimizing the laser operation through maximizing the OPA alignment to improve its modal content using longer length of fiber to increase the interaction length and improving the beam quality of the mid-IR emissions. The highest pulse energy ever obtained in the 3 μm mid-IR region from the acetylene-filled HOFGLAS after applying the improvements is reported here (1.4 μJ). Higher mid-IR pulse energies can be achieved by improving the pulse energy achievable from the OPA pump source and working with longer pulse duration to decrease the bandwidth of the OPA. This operation demonstrates many novel properties of acetylene-filled pulsed mid-IR hollow-core fiber lasers. The excellent spatial beam quality at highest power and phenomenological scaling of saturation power and efficiency with pressure that we observe point to the promise of power scaling and motivate further development of numerical models of the laser for deeper insight into these effects. M^2 measurement method was used to examine spatial beam quality and it was found

to be fiber-dependent. For the improved setup, M^2 was investigated at several input pump powers in addition to the reproducibility checks. M^2 of 1.14 at the maximum output power motivates for beam combining to scale to higher power. The independence of efficiency on pressure is an evidence for reaching higher mid-IR power at a pressure where saturation behavior does not exist. achieving the highest mid-IR power to date, 1.4 μJ, encourages for building higher power OPA to produce high power mid-IR emissions. Taken as a whole, this laser exhibits novel behavior that motivates both numerical/theoretical investigation and further efforts to scale to higher powers.

Improved performance of an optically pumped mid-infrared acetylene-filled hollow-core fiber laser

by

Neda Dadashzadeh

B.S., University of Tehran, 2007
M.S., University of Tabriz, 2011

A DISSERTATION

submitted in partial fulfillment of the requirements for the degree

DOCTOR OF PHILOSOPHY

Department of Physics
College of Arts and Sciences

KANSAS STATE UNIVERSITY
Manhattan, Kansas

2017

Approved by:

Major Professor
Kristan Corwin

Copyright

Abstract

The focus of this research is improving the pulse output energy of a mid-IR pulsed acetylene-filled Hollow-core Optical Fiber Gas LASer (HOFGLAS) system. Pump pulses and acetylene molecules interact with each other inside hollow-core photonic crystal fiber that effectively confines light and allows for strong gain. This results in lasing at 3.11 μm and 3.17 μm lines based on population inversion of acetylene molecules, which are optically pumped at rotational-vibrational overtones near 1.5 μm using 1 ns pulse duration from an optical parametric amplifier (OPA). This acetylene laser operates with no cavity mirrors because of a high gain in a single pass configuration. There are few laser sources in the mid-IR region while there are many applications for having a laser source in this range such as remote sensing, hazardous chemical detection, and breath analysis. This adds to the importance of the acetylene-filled HOFGLAS system. Some of the applications like remote sensing require high power. So, we moved toward power scaling this laser system by optimizing the laser operation through maximizing the OPA alignment to improve its modal content using longer length of fiber to increase the interaction length and improving the beam quality of the mid-IR emissions. The highest pulse energy ever obtained in the 3 μm mid-IR region from the acetylene-filled HOFGLAS after applying the improvements is reported here (1.4 μJ). Higher mid-IR pulse energies can be achieved by improving the pulse energy achievable from the OPA pump source and working with longer pulse duration to decrease the bandwidth of the OPA. This operation demonstrates many novel properties of acetylene-filled pulsed mid-IR hollow-core fiber lasers. The excellent spatial beam quality at highest power and phenomenological scaling of saturation power and efficiency with pressure that we observe point to the promise of power scaling and motivate further development of numerical models of the laser for deeper insight into these effects. M^2 measurement method was used to examine spatial beam quality and it was found

to be fiber-dependent. For the improved setup, M^2 was investigated at several input pump powers in addition to the reproducibility checks. M^2 of 1.14 at the maximum output power motivates for beam combining to scale to higher power. The independence of efficiency on pressure is an evidence for reaching higher mid-IR power at a pressure where saturation behavior does not exist. achieving the highest mid-IR power to date, 1.4 μJ, encourages for building higher power OPA to produce high power mid-IR emissions. Taken as a whole, this laser exhibits novel behavior that motivates both numerical/theoretical investigation and further efforts to scale to higher powers.

Table of Contents

List of Figures

List of Tables

Acknowledgements

This work was supported by the Air Force Office of Scientific Research (AFOSR) through grant (FA9550-14-1-0024), Air Force Research Laboratory (AFRL) through grant (FA9451-17-2-0011). We thank Dr. Fetah Benabid for providing us with optical fibers and they were funded by Agence Nationale de la Recherche (ANR) (PHOTOSYNTH) and (Σ_LIM Labex Chaire). La région Limousin. They also had the support from the PLATINOM platform for the fiber fabrication. We thank Professor Wolfgang Rudolph and Dr. Vasudevan Nampoothiri for great collaboration and all useful discussions. We acknowledge staff of the James R. Macdonald laboratory for helpful technical contributions specially Kevin Carnes, Charles Fehrenbach, Mike Wells, and Al Rankin.

I would like to thank my advisor Professor Kristan Corwin for her endless support. I am so honored to have worked with her for the past six years. She has not only been my advisor but also my best friend in the United States. I would like to thank Professor Brian Washburn for his support. His lasers and nonlinear optics class notes as well as his excellent programming skills are essentials for every graduate student in AMO physics to be successful in his/her research.

A special thanks to Dr. Andrew Jones for his useful thesis and all his help. Thanks to my lab mates in the past and present: Dr. Rajesh Kadel, Dr. Shun Wu, Dr. Chenchen Wang, Dr. Manasa Thirugnanasambandam, Mary Harner, Sajed Hosseini Zavareh, Kushan Weerasinghe, Ryan Luder, Mai Ebini, Mattithyah Tillotson, and Stephen Meinhardt.

I would like to acknowledge all faculty and staff in Kansas State University. Special thanks to Dr. Mo Hosni, Dr. Michael O'Shea, Dr. Richard Yankowiak, Dr. Asad Esmaeily and Shookooh khanoom, Dr. Brett DePaola, Dr. Shahin Nayyeri, Dr. Carlos Trallero, Dr. Artem Rudenko, Kim Coy, Donnita Nelson, Kathy Van Steenis, Kim Elliot, Peggy Matthews, Lindsay Miller, Dianna, Vince Needham, Larry McFeeters, Peter Nelson, Austin Roberts, and Emily Taylor.

I also would like to thank my friends who played important roles in my success. Thanks to Derrek Wilson for always being a good friend and for his great help in revisions of this dissertation. Thanks to Dr. Barker and Dr. McKenna for saving my life. Thanks to Dr. Sahar Kassani and Dr. Reza Khazaeinezhad for taking care of me when I really needed it. Thanks to my sisters Dr. Nassim Rahmani, Dr. Hedieh Shadmani, and Dr. Shirin Sabouri. Thanks to Raha Samani and her kind family. Thanks to Dr. Shahab Shervin, and Ali Khoshkhoo for their kind heart. Thanks to Naghmeh

Moghimi, Reza Mazloom, Dr. Mo Zohrabi, Dr. Amy Rouinfar, Dr. Shuo Zeng, Aram Vajdi, Erfan Saydanzad, Bahar Modir, Dr. Sean Mcbride, Dr. Sachiko Toda, Dr. Varun Makhija, Dr. Nora Kling, Dr. Stephen Zigo, Adam Summers, Kali summers, Brandin Davis, Jeff Powell, Farzaneh Ziaee and Jalal sadeghi, Mahboobe Jassas and agha Hamid, Aleena Rafique, Dr. Yuba raj Dahal, Youliang Yu, Pratap Timilsina, Raju Pandiri, Travis Severt, Georgios Kolliopoulos, Jan Tross, Marcelo Ambrosio, Russ Averin, Dr. Matthias Kling, Dr. Kelsie Betsch, Dr. Ren Xiaoming, Dr. Bachana Lomsadze, Wes Erbsen, Dr. Maia Magrakvelidze, Dr. Mojgan Matloob, Zhanna Rodnova, Dr. Sheryll Namingit-Wales, Dr. Michael Wales, Dr. Gazi Dogan, Dr. Kamran Nasiri, Dr. Peyman Ahmadi, Dr. Reza Kheradmand, Dr. Roxana Rezvani Naraghi, Dr. Naghmeh Rezaei, Pooya Karimian, Dr. Arash Omrani, Xiaofei Song (Smilie), Sheida Nazarian and Reza Ghaffari, Sara Taheri and Ehsan Rahiminasab, Hossein Amini and Arefeh jan, Mehraz Khaleghi, Elsa Shervin, Kaveh Shervin, Sheida Parvasi, Pedram Soltanpour, Milad Yarali, Dr. Somik Mukherjee, Niloofar Fattahi, Alaleh Alivar, Efaf Mansoori, Mehrsa Khaleghi, Arash Soltani, Hazhar Sufi, Alireza Lolagar, Alireza Afiat, Alireza Shams, Dr. Nassim Sabahfar, Ali Masihi, and many other great friends.

Finally, I would like to thank my amazing family members. I am so blessed to have the most caring and supportive family in the world. Special thanks to my mom (Parvin Veyssi), my dad (Anoshirvan Dadashzadeh), and my brother (Nima Dadashzadeh) for their emotional and financial support during my entire life. Thanks to Arezoo Alaghbandha, Shahla Amiripour, and my most caring uncle, Afshin Dadashzadeh. I am feeling so lucky for having the best people in my life.

Dedication

این پایان نامه تقدیم می شود به:

مامان پروین و بابا انوش و یکی یکدونه داداش، نیما جانم

و همچنین آرزو خانم و عمو افشین و زن عمو شهلا.

This dissertation is dedicated to my mother (Parvin Veysi), my father (Anoshiravan Dadadashzadeh), and my brother (Nima Dadashzadeh). It is also dedicated to Arezoo Alaghebandha, Shahla Amiripoor, and Afshin Dadashzadeh.

Chapter 1 - Introduction

The first Continuous Wave (CW) beams started with gas lasers and they were used to make the first holograms and weld metals. Today, they have wide variety of applications such as in medicine and photolithography [1]. Gas lasers work based on population inversion between energy states of gas, which is the active media of the laser system. The laser medium is kept in a plasma tube. In electrically pumped cases, two electrodes for electrical discharge are installed at two ends of the tube and are followed by dielectric mirrors to form the cavity. Gas lasers may be defined as atomic gas lasers, molecular gas lasers, ionized gas lasers, etc. A good example for atomic gas lasers is He-Ne laser. Examples of molecular gas lasers are CO_2, CO, and N_2 gas lasers. Argon ion lasers and krypton ion lasers are examples of ionized gas lasers. In this introduction, He-Ne, Ar+, and CO_2 lasers are explained briefly as examples of atomic, ionized, and molecular gas lasers. The newest generation of gas lasers operate in hollow optical fibers and are discussed in this dissertation [2-8]. Gas lasers have many distinct advantages such as their cheap active medium, high damage threshold, widely tunable wavelength range, and high efficiency especially in optically pumped gas lasers. By selecting the appropriate gas for the active medium, it is possible to create lasers with emission wavelengths ranging from the UV to the IR. This is possible due to the large range of emission lines in atomic, molecular, and ionized gasses.

Despite many advantages, conventional gas lasers do have a few detriments. Although heat mitigation techniques specific to gases like gas flow have been developed, gas lasers still suffer from heat management at high pump powers. An additional challenge of using a gas as the laser medium is the relatively short interaction length between the pumping source and the gas. Gas lasers, operating in hollow optical fibers have the exciting potential to overcome these challenges.

The first successful gas lasers created was the helium-neon laser (He-Ne laser). Ali Javan, Bill Bennett, and Don Herriott worked on developing the first He-Ne laser for about two years at Bell Labs [1]. The first He-Ne laser emitted at 1153 nm. However, at that time a laser that could operate in visible wavelength range was more desirable. So, other neon transitions were carefully investigated to find emissions in the visible region from He-Ne laser. The 633 nm emission line in He-Ne laser was found to have the highest gain in the visible range. Alan White and Dane Rigden made the first 632.8 nm red He-Ne laser in 1962 and it was the first visible CW laser [1]. The gain medium of the laser is a mixture of helium and neon gases, in the ratio of 10:1 respectively [9]. By pumping the system, helium atoms can be excited because the gas mixture is mostly helium. Due to collision of the excited helium atoms with neon atoms, some of neon atoms get excited to certain energy levels that could then radiate in three lasing lines (633 nm, 1.15 μm, and 3.39 μm) as shown in Figure 1.1. So, the population inversion and light amplification processes in a He-Ne laser starts with inelastic collisions of energetic electrons from the pump with the ground state of helium atoms in the gas mixture. The collisions excite helium atoms from the ground state to excited states. Collisions between these excited helium atoms and neon atoms in the ground state result in an efficient transfer of excitation energy from helium to neon. Excitation energy transfer increases the population of two upper levels in Neon and population inversion between Neon energy levels occurs. The medium then amplifies light in two narrow bandwidths at wavelengths of 633 nm and 1.15 μm. The lower laser level is emptied by fast radiative decay to another lower energy state and reaching the ground state eventually [9]. The highly reflecting mirrors at two ends of the amplifying media produces lasing in particular spatial modes. Radiation in these modes will build up until gain saturation occurs and it results in a continuous laser beam output. The gain bandwidth of the He-Ne laser is dominated by Doppler broadening rather than pressure broadening because

of low gas pressure; therefore, produces a quite narrow bandwidth, e.g. only about 1.5 GHz full width half-max for the 633 nm transition [9]. A neon laser without helium can be constructed but its demonstration is difficult because with no helium, the neon atoms would be excited to lower excited states that won't result in lasing lines. The laser was electrically pumped in early demonstrations i.e. the pump source of the laser was a high voltage electrical discharge between electrodes at two ends of the gas tube.

The He-Ne laser was commercialized in 1965. The original He-Ne lasers could produce only around one milliwatt of output power and the main use of this laser was limited to holography. In 1965, the first 3D holograms were made by Emmett Leith and Juris Upatneiks at the university of Michigan [1].

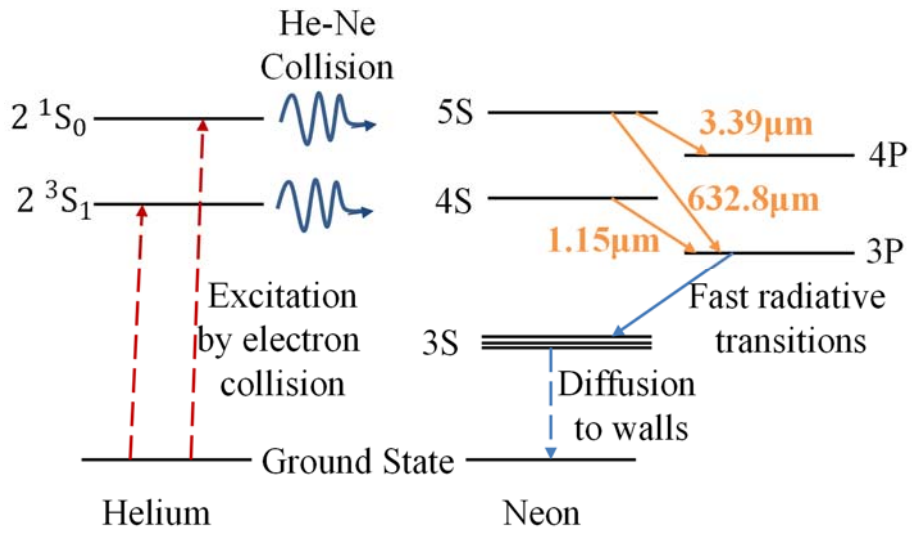

Figure 1.1: Energy level diagram for He-Ne laser, is reproduced from Ref. [9].

The gas in the vacuum tube can be replaced by a different gas to produce new effects. Earl Bell demonstrated a mercury-ion laser in 1963 and Bill Bridges reported demonstration of the first argon-ion laser at Hughes Research Labs in 1964 [1].

An ion laser is a gas laser that uses an ionized gas as its lasing medium [10]. The energy level transitions that contribute to lasing come from ions as shown in Figure 1.2. A downside is the large amount of energy required for the gas to be ionized and excitation between energy levels to happen. So, in electrically pumped cases, high current is required. Therefore, heat sinking and cooling mechanisms are needed. Applications of argon-ion lasers include uses in retinal phototherapy (for diabetes), lithography, and pumping other lasers. Argon-ion lasers can emit at several wavelengths ranging from the ultraviolet, to the visible, and though the near-visible light region, some of them are shown in Figure 1.2. Argon ion lasers can be designed to produce continuous-wave output of milliwatt levels to tens of watts. In 1965, a commercial 1 W argon ion laser by Raytheon's Research Division was developed.

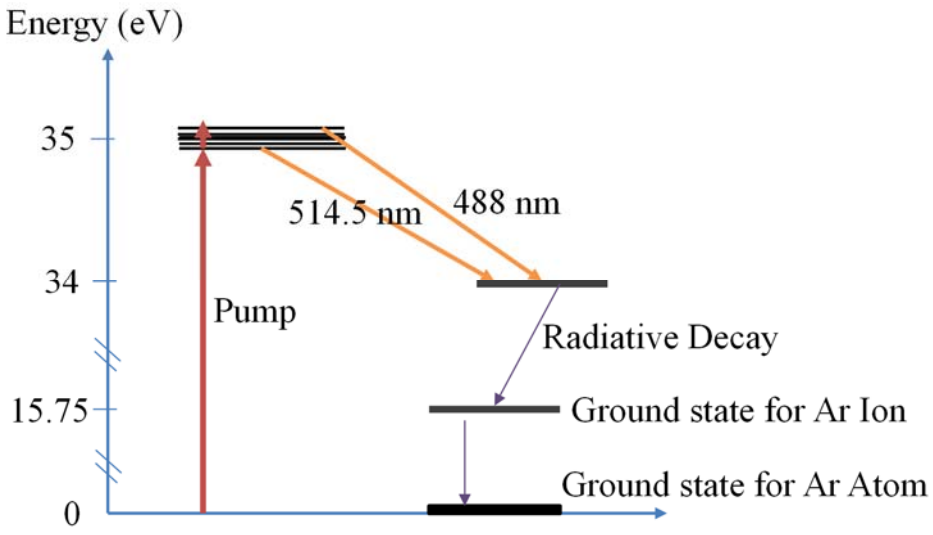

Figure 1.2: Argon ion laser's energy level diagram, is reproduced from Ref. [9].

Using carbon-dioxide as the laser gain medium allows for the production of the highest achievable CW power levels. CW output power at 130 W and efficiency of ~14% was achieved by the inventor of the CO_2 laser, Kumar N. Patel of Bell Labs in 1965. Also, CO_2 lasers have high slope efficiency, i.e. the ratio of output power to input pump power. The CO_2 laser have emissions at 9.6 μm and 10.6 μm. The active medium consists of ~ 20% CO_2, ~ 20% N_2, a few percent H_2 or Xe and a few percent of He. The proportions may vary in each particular CO_2 laser. An energy level diagram of a CO_2 laser is shown in Figure 1.3.

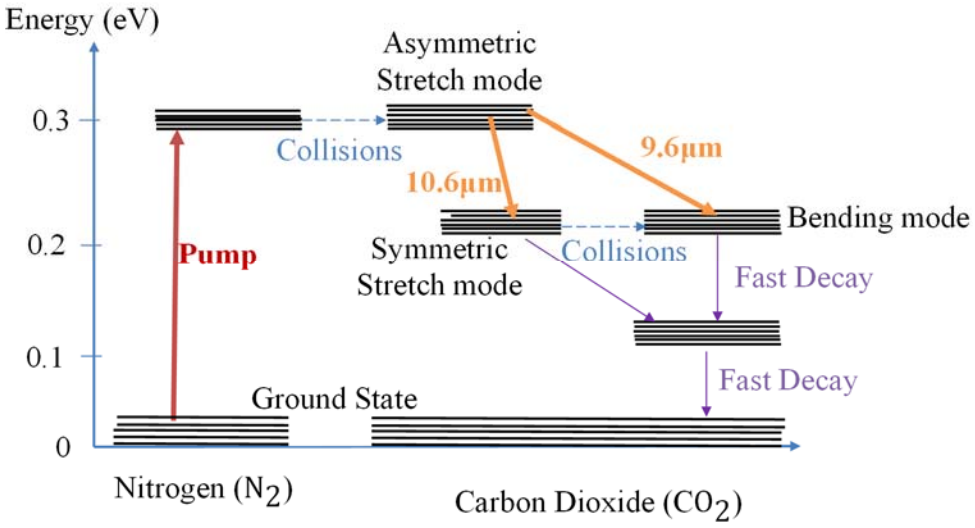

Figure 1.3: Carbon-dioxide energy level diagram, is reproduced from Ref. [9].

The population inversion is achieved in the nitrogen molecules as the media is pumped. Collisional energy transfer between the excited nitrogen molecules and the carbon dioxide molecules excites carbon dioxide molecules from ground state to an excited state and lead to population inversion for laser operation between carbon dioxide molecules. On the other hand, the transition of nitrogen molecules to ground state happens through collision with cold He atoms. The remaining hot He atoms must still contribute in producing population inversion in carbon dioxide

molecules; so, they should be cooled down and the walls of the gas tube help in cooling process. CO_2 laser can also be used in pulsed operation as well as in the CW operation. The 9.6 μm and 10.6 μm wavelengths emission lines of CO_2 lasers are useful because they are in a window for high atmospheric transmission and also many materials have strong absorptions in this range of wavelengths.

In 1974, other gas lasers such as Helium-cadmium lasers, Nitrogen lasers, and helium-xenon laser pumped by neutrons from pulsed nuclear reactors were announced [1]. In 1975, rare-gas halide excimer lasers were demonstrated. For example, the first discharge-pumped xenon fluride laser at 351 and 352 nm and 130 mJ pulses from krypton fluoride laser were reported [1]. In 1987, top five gas lasers based on market sales were reported in Laser Focus World magazine: 1) CO_2 lasers 2) Ion lasers, 3) He-Ne lasers, 4) Excimer laser, and 5) He-Cd lasers. They also announced the top 4 laser devices: 1) Green He-Ne (543 nm), 2) Tunable He-Ne (632.8, 612, 604, 594 nm), 3) a battery-powered handheld 1 mW red He-Ne, and 4) a red He-Ne laser pointer [1].Today, CO_2 and excimer lasers are still being used due to the fact that no good competitors exist in their important range of wavelengths. On the other hand, He-Ne and ion lasers are being used today in the applications that require long coherence length and single-mode operation.

Progress toward power scaling of the laser systems began in 1970 when US military researchers scaled two gas lasers to impressive power levels. The Air Force's Airborne Laser Laboratory scaled CO_2 lasers to 400 kW level and Navy built the mid-IR chemical laser up to two Megawatts power level. In 1981, a multi-megawatt hydrogen-fluoride laser from DARPA was reported [1]. In 2010, military researchers continued working on diode-pumped alkali vapor lasers, that are still the best options for megawatt power levels and could offer optical conversion efficiency of ~ 90%. The first demonstration of Diode Pumped Alkali Lasers (DPAL) took place

at Lawrence Livermore National Laboratory in 2002. Afterwards, many other developments are reported toward power scaling, achieving good efficiency, and improving beam quality. DPALs combine features of both solid-state lasers and gas lasers. They work based on diode excitation of atomic alkali vapors. Therefore, they have the ability to be pumped by a source with wide spectral emissions and this characterization distinguishes DPALs from previous demonstrations of alkali lasers since alkali lasers used to be pumped by coherent and narrow-band pump source [11]. DPALs solve problems of heat dissipation that limited the beam quality of kilowatt-class solid-state lasers. In 2003, it was reported that commercially available near-infrared laser diodes could pump alkali vapors very efficiently. Afterwards, DPALs have been demonstrated for potassium, rubidium, and cesium vapors. In rubidium and cesium DPALs, slope efficiencies are about 50% [12, 13].

There has been a number of optically pumped gas lasers demonstrations such as [14-22] that some of them can be pumped on resonance with the wavelength range that is covered by commercial pump sources. HBr gas cell, that was pumped at 1.3 μm, emits light at 4 μm with slope efficiency of 25% [20]. Later, 50% slope efficiency was obtained from HBr 4 μm cascade laser [23]. In main problem in using conventional gas cells in optically pumped gas lasers is the very short interaction length between pump and media. So, the system can be bulky and this limits their applications. Research has continued on new types of gas lasers that operate inside hollow-core optical fibers. Researchers are taking confinement and energy transfer techniques developed for solid-state lasers and applying them for gas lasers [1]. In 2010, the first time demonstration of this new generation of gas lasers happened in our research group where Kristan Corwin, Brian Washburn, and Wolfgang Rudolph lead the team. These lasers are named HOFGLAS, which stands for Hollow Optical Fiber Gas LASers [8, 24]. The first HOFGLAS, exciting 3 μm lasing

from acetylene with 1.5 μm nanosecond pump pulses and gain was so high in acetylene-filled HOFGLAS that lasing was observed, despite the fiber's loss of 20 dB/m at 3 micron [6]. Then, Fetah Benabid, from Xlim research institute at university of Limoges (France) developed the hollow core fibers with hypocycloidal core shape, which reduces loss at 3 μm. As in solid-core fibers, the long interaction length improves energy transfer from pump to active media; however, the laser beam is guided in the hollow core (free space) rather than in a solid core. Host materials in solid core fibers are replaced by a gas in gas-filled hollow-core fibers. The threshold for nonlinear effects such as Stimulated Brillion Scattering is higher in gas-filled hollow fibers and they offer higher damage threshold and better heat management than solid core fiber lasers. By improving operation of the acetylene-filled HOFGLAS setup and using lower loss fibers in mid-IR, near diffraction-limited beam quality and higher mid-IR pulse energy are obtained. A phenomenological study of the laser system promise further power scaling with maintaining good beam quality [25]. The group has demonstrated CW operation at 1280 to 1340 nm in a hollow-core fiber filled with molecular iodine and pumped at 532 nm in University of New Mexico in 2015 [5].

In chapter 2 of this dissertation, mid-IR solid core fiber lasers are discussed briefly and then all existing HOFGLAS systems up to this date including the mid-IR acetylene-filled HOFGLAS are introduced. Chapter 3 starts with an introduction on history of optical fibers. Then, loss measurement of optical fibers in mid-IR are discussed and the results of performing mid-IR cut-back measurements are presented for a hypocycloidal core Kagome hollow fiber. In chapter 4, the characteristics of the OPA pumped acetylene-filled HOFGLAS and the improvements on its setup are discussed in details. The published results of laser operations and beam quality measurements are investigated in chapter 5. Our attempts toward first time demonstration of

continuous wave HCN-filled HOFGLAS are discussed in chapter 6. Finally, future work plans on HOFGLAS systems in our lab are presented in chapter 7.

Chapter 2 - From fiber lasers to gas fiber lasers

2.1. Introduction to fiber lasers

Fiber lasers have many applications in medicine, remote sensing, and security because of their excellent properties such as compactness, portability, good beam quality, high efficiency, and convenient heat management. Fiber lasers are replacing traditional gas lasers and solid-state lasers.

Solid-core fiber lasers are lasers with optical fibers as their gain medium. They can be pumped from one side or from both sides and may have one of the architectures shown in Figure 2.1. Usually solid-core fiber lasers are diode-pumped. To form a resonator, mirrors are placed at two ends of the fiber. Mirrors can be placed perpendicular to the fiber ends or one of them can be placed at an angle with respect to the beam propagation direction to detect laser output in a separate beam path. In laboratories, usually dichroic mirrors are used in front of the cleaved fiber ends and in commercial products, Fiber Bragg Gratings (FBG) at two ends of the fiber act as cavity reflectors.

In most solid-core fiber lasers, the gain medium is a fiber doped with rare earth ions such as erbium (Er^{+3}), ytterbium (Yb^{+3}), thulium (Tm^{+3}), neodymium (Nd^{+3}), or praseodymium (Pr^{+3}). Although the medium in solid-core fiber lasers are similar to traditional bulky solid-state lasers, the effects of small mode area and waveguiding result in achieving different laser properties such as obtaining higher gain or good beam quality.

There are a few nonlinear processes that limit the power of fiber lasers such as Stimulated Brillouin Scattering, Stimulated Raman Scattering, surface damage, self-phase modulation, and self-focusing. For example, Brillouin scattering effect is related to the $\chi^{(3)}$ medium nonlinearity and it causes an incident photon to be converted into a scattered photon with lower energy, that usually propagates in backward direction, and a phonon. If input power will be above a certain

threshold value, Stimulated Brillouin Scattering may reflect most of input beam's power. Because there will be a strong nonlinear optical gain for the beam which propagates in the backward direction. Therefore, the generated weak counter-propagating beam, which is at a certain frequency, can be amplified strongly. As another example, Stimulated Raman Scattering may happen in a nonlinear medium, where pump and signal wavelengths propagate together. The signal wavelength, which is the longer wavelength beam (Stoke beam), can be amplified. In addition, excitation of lattice vibrations happens and increases the temperature inside the media. In other words, one pump photon can be converted to one lower-energy signal photon, and the difference of the photon energies is carried away by a phonon, which is a quantum of the lattice vibrations. It is also possible that an already existing phonon interacts with a pump photon to generate one higher-energy photon at a shorter wavelength (anti-stoke beam) but this process is usually weak especially at low temperature.

Fundamentals and power scaling of a 2 μm Tm-doped silica fiber laser was reported [26]. This is a good example to understand the lasing mechanism in fiber lasers. The pump laser was at 790 nm for this laser system. Using a 25 μm diameter silica fiber with NA of 0.08, laser efficiency of 64.5% was reported. In this laser operation, near diffraction limited output beam had 300W power for 500 W of launched pump power. An operation of this laser system using a 35 μm diameter silica fiber with NA of 0.2 resulted in a multimode output beam with 885 W power. Today, these lasers produce more than 1kW of CW power. The pump quantum efficiency in this laser is 1.84, which is more than 1. The reason can be found in the investigation of the importance of Cross Relaxation (CR) and Energy Transfer Upconversion (ETU) processes to the operation of Tm-doped silica fiber lasers. The slope efficiency of this laser is proportional to the Tm^{+3}

concentration. ETU from the lower laser level recycles excitation as shown in Figure 2.2 [27] and CR is operating in the silica host efficiently because of a strong spectral overlap feature.

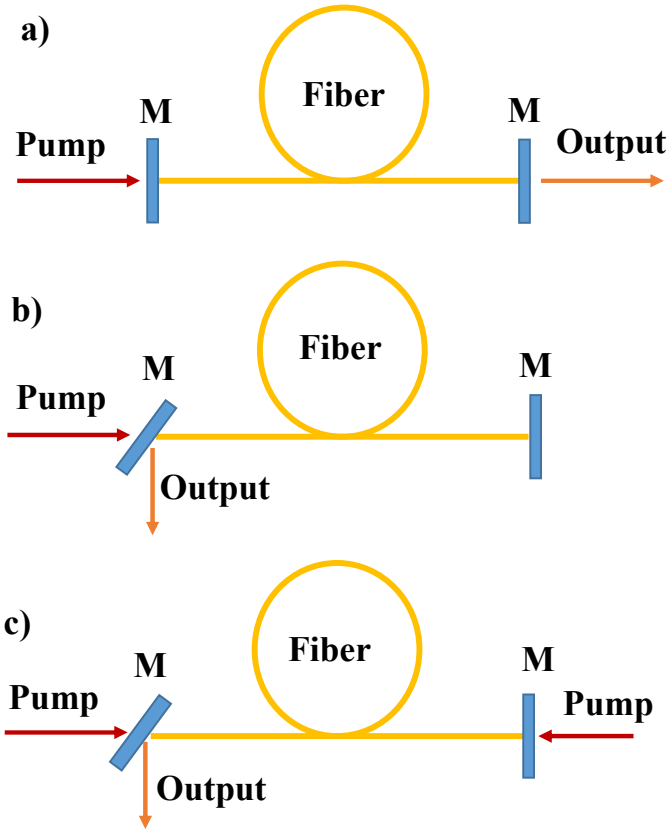

Figure 2.1: Pumping architectures in fiber lasers: a) pumping from one side and cavity mirrors are placed perpendicular to the beam propagation direction. b) pumping from one side and one of the cavity mirrors is placed at an angle with respect to the beam propagation direction. c) bidirectional pumping and one of the cavity mirrors is placed in an angle with respect to the beam propagation direction.

ETU, which is the energy transfer between different dopant ions, happens particularly in highly doped solid-state gain media. The mechanism behind this is usually the dipole–dipole resonant interaction between ions that are located very close to each other. Emission and reabsorption of fluorescence photons are also other mechanisms behind ETU over longer distances

inside media because the strength of the dipole–dipole interaction rapidly vanishes with increasing distance between the ions. ETU importance depends on the doping concentration strongly.

In Cross Relaxation effect, an excited ion transfers part of its energy to another ion in the ground state. Therefore, both ions end up in some intermediate level. This process is helpful in the Tm-doped 2-μm laser as mentioned above but in other cases the laser efficiency can be degraded.

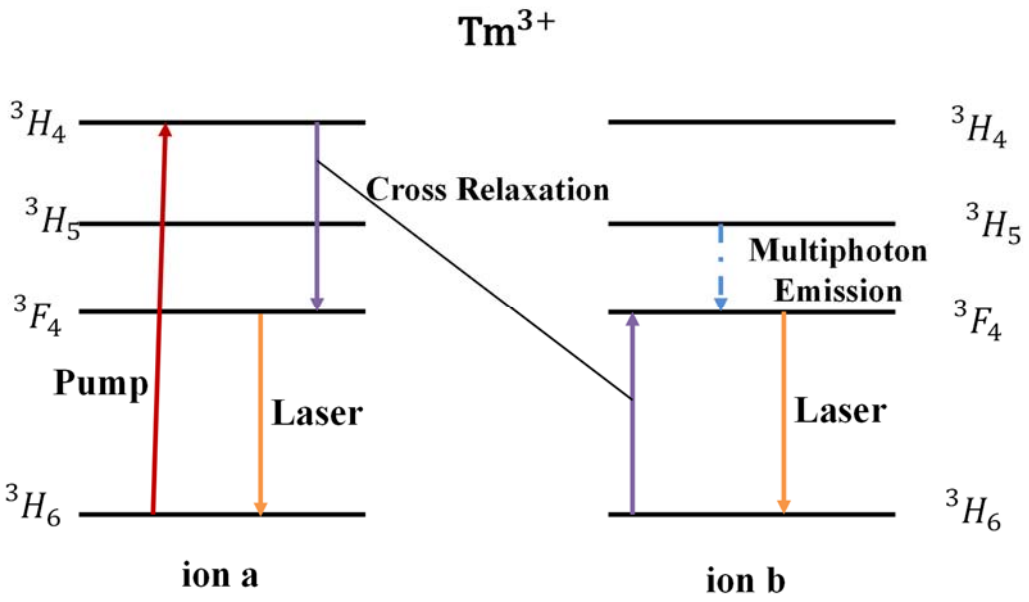

Figure 2.2: Simplified energy level diagram of two Tm3+ ions (ions a and b). The main cross relaxation process between ions a and b and the laser transitions are shown, reproduced from Ref. [27].

The main cross relaxation for two Er^{3+} ions and laser transition as also shown in Figure 2.3. Upper and lower lasing levels in Er-doped fiber lasers is different from Tm-doped fiber lasers but the lasing mechanism follows the same concepts. Silica fibers can not go far beyond 2 μm in wavelength because they get absorbing above this wavelength.

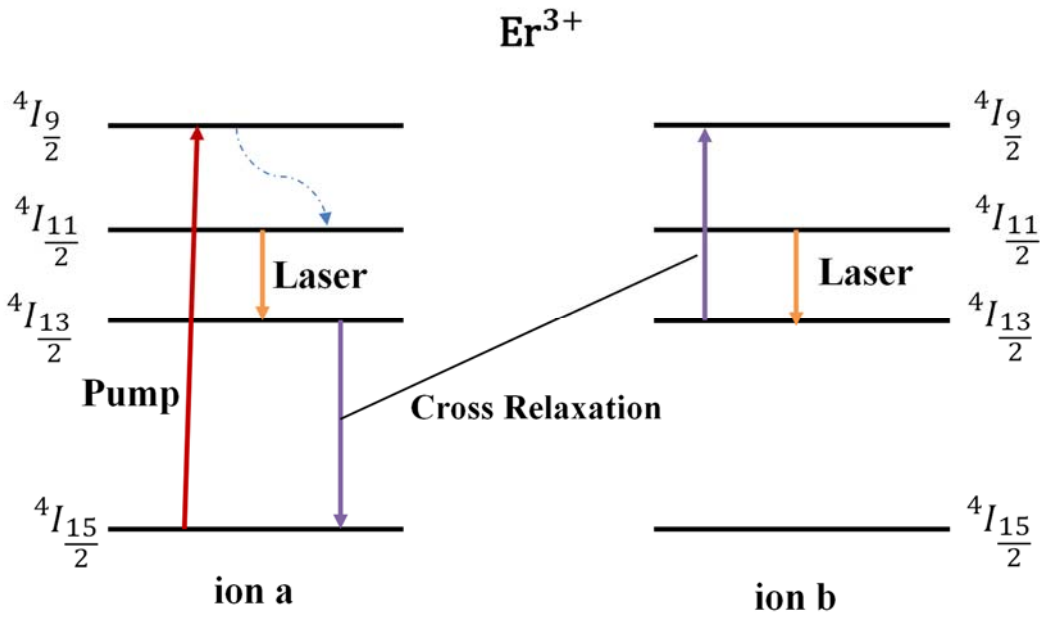

Figure 2.3: Simplified energy level diagram of two Er^{3+} ions (ions a and b). The main cross relaxation and laser transitions are shown in the figure.

ZBLAN fiber lasers, ZBLAN= ZrF4-BaF2-LaF3-AlF3-NaF, and chalcogenide fiber lasers are the most important mid-IR fiber lasers. Chalcogenide fiber lasers have made great progress in operation in the mid-IR range of wavelength but Chalcogenide fibers have drawbacks such as nonlinearity, fiber strength, and stability.

Ho^{3+}:Pr^{3+}-doped ZBLAN fiber laser may generate 2.94 μm output. At an operation where 1150 nm strained InGaAs diode pump and 10 μm fiber with NA of 0.2 are used, this laser may produce around 2.5 W output power at slope efficiency of 32% [28].

Er-doped ZBLAN fiber laser may produce tunable 2.7 to 2.9 μm stable output. The 975 nm diode pump at 100 W power can be used to pump a 25 μm fiber with NA of 0.12 and the laser may produce up to 10 W output power [29].

In addition to the lasers mentioned above, Er:fluoride fiber laser may emit 2.8 μm beam. 0.976 μm pump can be used to generate 2.5 W output power from Er:fluoride fiber laser [30, 31].

Due to the low damage thresholds, usually solid-core fiber lasers lack the ability to provide the same power levels as conventional gas lasers or solid-state bulk lasers. On the other hand, at high powers, the output from solid-state fiber lasers usually have broad spectral linewidth because of nonlinear effects. Also, since the number of rare earth materials is limited, only certain laser wavelengths can be achieved from these lasers.

The advent of hollow-core photonic crystal fiber (HC-PCF) and its ability to host gas for long interaction length enabled new generation of fiber lasers called gas-filled fiber lasers. There are nonlinear optical processes that limit power scaling in solid core fiber lasers as mentioned earlier in this chapter. Hence, in gas-filled fiber lasers, there is no solid host material and gain is provided by gas inside a hollow fiber core; thus, more power scaling is predicted. These lasers take advantage of both fiber and gas laser features.

In the following section, gas-filled hollow core fiber lasers are discussed including 3 μm acetylene-filled fiber laser. There are not many laser sources in this range of wavelength because silica fibers get absorbing above 2.5μm and on the other hand quantum cascade lasers have difficulty in operation bellow 3.5 μm. Also, as mentioned earlier in this chapter, chalcogenide fiber have made great progress in operation in this range of wavelength but they have drawbacks such as nonlinearity, fiber strength and stability. So, there are not many laser sources in this range other than some conventional bulky gas lasers; however, there are many applications in medicine, hazardous gas detection, remote sensing, and defense. This fact makes the acetylene-filled hollow fiber laser that is discussed in this dissertation so special.

2.2. Hollow-core Optical Fiber Gas LASers (HOFGLAS)

Hollow-core Optical Fiber Gas Lasers (HOFGLAS) offer the possibility of producing the high average power and very good slope efficiency of gas lasers [13, 32-35] along with the merits of a fiber-based laser [36]. The first successful demonstration of acetylene-filled HOFGLAS by Jones *et al.* [8, 24] began a new chapter in gas and fiber laser research. Since then, HOFGLAS in a variety of gasses including HCN, CO, CO_2 and I_2 have been demonstrated [5-7, 24, 37], spanning a wide wavelength range, and even demonstrating CW operation [4, 5]. All existing HOFGLAS system are summarized in Table 2.1.

Table 2.1: Existing HOFGLAS systems.

HOFGLAS	Year	Pump / Wavelength (µm)	Lasing lines (µm)	Slope efficiency (%)	Max output energy	Fiber	University
pulsed C_2H_2-filled	2010	OPA: 1.532	3.114 & 3.17	12	0.5 µJ	Hypocycloid Kagome HC-PCF	KSU+UNM
pulsed C_2H_2-filled	2016	OPA: 1.532	3.114 & 3.17	20	1.4 µJ	Hypocycloid Kagome HC-PCF	KSU
pulsed C_2H_2-filled	2014	Amplified Modulated diode laser: 1.432	3.12 & 3.16	30	0.8 µJ	Hypocycloid Kagome HC-PCF	Bath
CW C_2H_2-filled	2016	Diode-laser: 1.530	3.1-3.2	8.8	4 mW	Hypocycloid Kagome HC-PCF	Bath
Pulsed CO_2-filled	2010	OPO: 2	4.37 & 4.3	20	100 µJ	Silver-coated capilary	UNM
Pulsed HCN-filled	2010	OPA: 1.5413	3.146 & 3.092	4	0.056 µJ	Hypocycloid Kagome HC-PCF	KSU
CW I_2-filled	2015	CW Nd:YVO4: 0.532	1.2-1.35	4	8 mW	Hypocycloid Kagome HC-PCF	UNM

Much of this success is owed to the progress in fabricating low loss hollow-core photonic crystal fibers (HC-PCF) that have formed the basis of efficient HOFGLAS systems. The fibers will be discussed in details in chapter 3 of this dissertation.

Acetylene-filled HOFGLAS is very special because it can operate in 3 μm where there are not many laser sources [7, 35]. An improved demonstration of acetylene-filled HOFGLAS by Jones et al. was reported [6, 7] in which a ns optical parametric amplifier (OPA) pump was used to launch an acetylene-filled HOFGLAS. Consequently, a 3 μm laser was achieved with more than 20% slope efficiency. Improved performance at 3 μm has also been demonstrated using a modulated, fiber-amplified diode laser as the pump at the university of Bath [3]. Hassan et al. [4] added a feedback fiber to the traditional HOFGLAS system; hence, the pump power required to produce 3 μm output is reduced. My report in this dissertation, highlights the power scalability and beam quality that can be achieved from a stable acetylene-filled HOFGLAS configuration using the OPA as the pump source [25]. The highest 3 μm pulse energy output of 1.4 μJ was achieved from an acetylene-filled pulsed HOFGLAS [2] using a 10.9 m length of hypocycloidal-core Kagome fiber filled with acetylene at 9.8 torr and in this operation, acetylene absorbed 8.2 μJ of OPA pump pulse energy along P(13) absorption line at 1.53 μm. This output laser pulse energy is nearly two times higher than the pulse energy reported in [3]. By increasing the pump power, higher power can be obtained from the setup. The laser operated at a constant slope efficiency of ~ 20% with respect to the absorbed pump pulse energy, independent of the acetylene pressure. Also, the beam quality of the laser output was investigated using the scanning slit method described in [38, 39] to measure the beam waist along the focus to obtain the M^2 of the 3 μm laser output. The characterization of the beam quality yields M^2 of 1.15 ± 0.02 for the 3 μm output which reflects the near-diffraction limited performance of the laser. Since $M^2 \leq 1.2$ results in ideal beam

combining [40, 41], the measured M^2 of our HOFGLAS system makes it a perfect choice for coherent beam combining. The good beam quality also makes this laser an excellent source for applications such as machining, medicine and telecommunications [40-42].

A.V.V. Nampoothiri, et al. demonstrated the first continuous wave I_2-filled HOFGLAS in 2015 [5]. Continuous wave I_2-filled HOFGLAS system consists of a negative-curvature hypocycloidal-core kagome hollow-core fiber filled with molecular iodine, $^{127}I_2$. The fiber is chosen based on its low loss at laser wavelengths, ~1.3 μm, which is measured to be 30 dB/km. Although it is desirable to work with a hollow-core fiber which has low loss at both pump and lasing wavelengths, this fiber has relatively high loss, 42 dB/m, around pump wavelength, 532 nm, because of the sharp resonance in transmission spectrum that occurs at certain wavelengths due to overlapping of core mode and cladding modes [5]. The pump laser is a tunable frequency-doubled Nd:Vanadate laser at 532 nm for this demonstration and curved mirrors are used to build the cavity.

Absorption features of iodine molecules in the visible spectral regions has been studied [43] and the emissions based on the excitation wavelengths may occur from ~500 nm to 1340 nm. Previously, a pulsed version of lasing in I_2 molecules has been observed in conventional fiber as well as continuous wave lasing. But, there is hope for more power scaling in gas-filled hollow-core fibers compared to solid core fibers because of replacing the host materials with the gas. So, attempts were made toward demonstration of continuous wave I_2-filled HOFGLAS. By tuning the pump laser on resonance with the desired molecular transition in I_2 gas, lasing at three wavelengths around 1.3 μm are observed using an Optical Spectrum Analyzer (OSA). It is demonstrated that laser power is a function of outcoupler's reflectivity and at the output mirror reflectivity of ~ 85%, maximum output power of ~ 8 mW has been obtained. Maximum efficiency of ~ 4% is reported

for this demonstration. Alignment of these lasers is a big challenge and makes them difficult to be demonstrated.

HCN-filled HOFGLAS system was pumped with 1 ns pulses from the homebuilt OPA. A 45 cm long kagome-structured HC-PCF was installed in the laser setup [7]. Pumping on P(10) , which is the transition from ground state to an overtone state of C-H asymmetric stretch mod, results in lasing at P(10) and R(8) lines correspond to ~3092 nm and ~3146 nm. The maximum of 56 nJ laser pulse energy was produced at 8 torr of HCN pressure which was about a factor 10 lower than the maximum laser pulse energy produced by acetylene laser under the same condition.

CO and CO_2-filled HOFGLASs were operated using 5 ns pulses from an OPO with 3.5 GHz bandwidth and maximum energy of ~ 1 mJ at 2 μm. 1.5 m of a silver-coated capillary fiber with inner core diameter of 500 μm was used in the setup. Fused silica HC-PCFs were not transmitting in the spectral emission region (~4 μm) and chalcogenide fibers were not available at that time [7] In CO-filled HOFGLAS pumping on resonance with R (7) from ground state to an excited state results in lasing in R(7) and P(6) lines related to ~4.65 μm and ~4.75 μm. In CO_2-filled HOFGLAS, pumping at R(22) results in lasing in multiple lines around 4.3 μm. The maximum laser pulse energy of ~ 100 μJ was obtained along with the laser efficiency of ~ 20 % and lasing threshold occurs around 40 μJ. The optimum pressure for lasing around 4.3 μm is ~ 100 torr.

Chapter 3 - Mid-IR fiber loss measurement

This chapter provides an introduction to the history of optical fibers and their propagation mechanism. Then, fiber loss measurements in the mid-IR are discussed. Finally, the results of mid-IR fiber loss measurements are used to choose the best fiber for acetylene-filled HOFGLAS.

3.1. Optical fibers

Optical fibers are famous for their outstanding waveguide properties. Their theory have been studied since the law of Total Internal Reflection (TIR) was discovered in the nineteenth century [44] and in early 1980s, telephone companies used them to rebuild their communications infrastructure. The first optical fiber had a higher refractive index core that was surrounded by a lower refractive index cladding, as shown in Figure 3.1. Afterwards, progress in fabricating low loss optical fiber influenced the telecommunication industry and in 2009, C. K. Kao received the Nobel Prize in Physics "for ground-breaking achievements concerning the transmission of light in fibers for optical communication" [45].

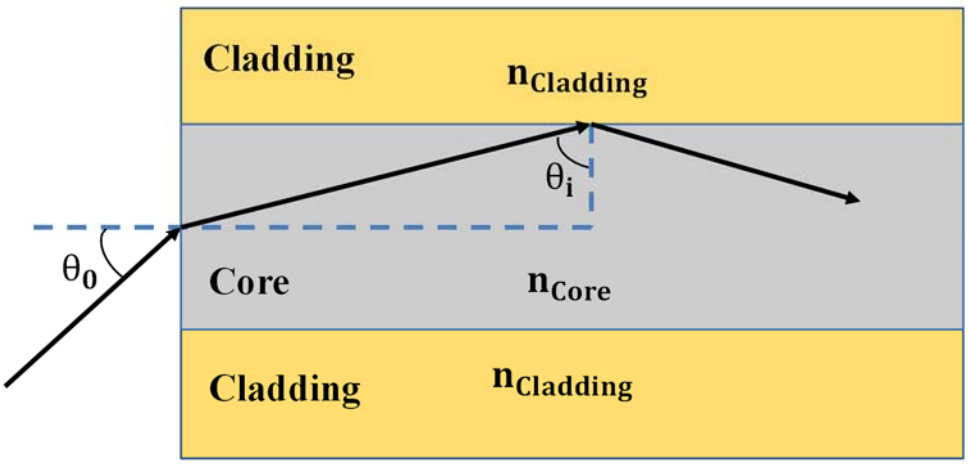

Figure 3.1: Light guidance in an optical fiber based on total internal reflection.

Light guidance in an optical fiber is described theoretically in Figure 3.1. n_0 is the index of refraction of the surrounding area that could be air, n_{core} is the index of refraction of the fiber core and $n_{cladding}$ is the refractive index of the cladding. θ_0 is the angle of the incident light and θ_i is the angle of internally reflected light. Other than the fact that refractive index of the core should be higher than the refractive index of the cladding, θ_0 should be within the angle defined by the Numeric Aperture (NA) of the fiber. Using the Snell's law and fiber geometry, fiber NA can be defined as Equation 3.1 [46].

$$\mathrm{NA} = n_0 \mathrm{Sin}\theta_0 = \sqrt{{n_{\mathrm{core}}}^2 - {n_{\mathrm{cladding}}}^2} \tag{3.1}$$

The NA for a Single Mode Fiber (SMF) is 0.12-0.14 and it is related to θ_0 of 15 degree, this information can be found on Thorlabs company's website [47]. In Figure 3.2, the cross-section of a standard telecom fiber along with the Gaussian electric field's fundamental mode distribution in the fiber is shown. It is clear that the electric field may penetrate into the cladding area but decreases very quickly in this region. The portion of the electric field that propagates in the cladding area is called the evanescent field. The telecom fibers are mainly based on fused silica and typically have a germanium-doped core.

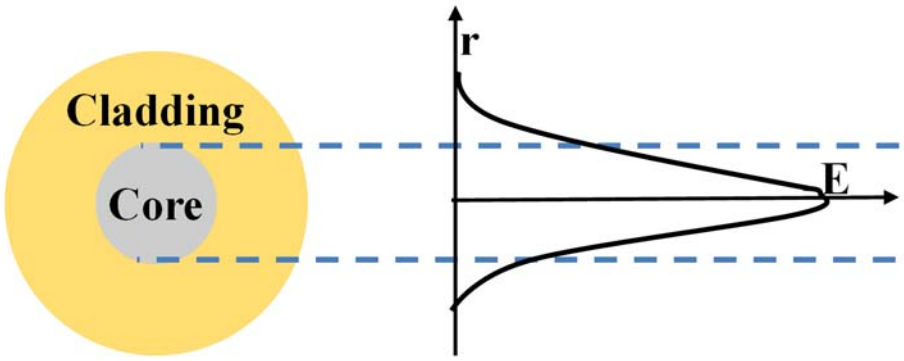

Figure 3.2: Fiber cross-section and fundamental mode of the electric field distribution in a single mode optical fiber.

Another fiber design involves the introduction of an array of microstructural elements. These so called microstructured fibers are also made of silica and they are similar to telecom fibers from the aspects of core diameter, cladding diameter, and NA. In particular, microstructured silica fibers have longitudinal holes in the cladding area. These fibers are index-guided fibers and guiding is obtained by effect of TIR. Microstructured fibers are built of one material (exp. Silica) and light guiding is obtained by the presence of air-holes in the area surrounding the solid-core. Fabrication of honeycomb microstructured optical fiber of this kind enabled John L. Hall and Theodor W. Hansch to receive the Nobel Prize in 2005 for " their contributions to the development of laser-based precision spectroscopy, including the optical frequency comb technique" [48].

Figure 3.3 shows some sketches of a few types of photonic crystal fibers cited from [49].

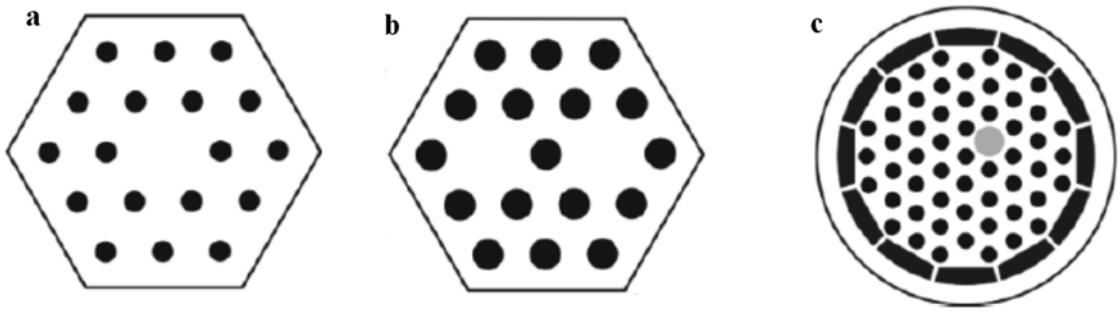

Figure 3.3: Sketches of a few types of photonic crystal fibers. a) Endlessly single mode solid core photonic crystal fiber. b) Dual core photonic crystal fiber. c) Double-clad photonic crystal fibers. Sketches are reproduced from reference [49].

Capillary fiber is another fiber design and it is also made of silica but it is different from telecom fiber because its core is not a waveguide. Loss of capillary fibers goes as $\sim \frac{\lambda^2}{{w_0}^3}$, where λ is the incident light's wavelength and w_0 is the free space beam waist of the incident light [50, 51].

So, the loss in capillary fibers is high. The holes in Capillary and microstructured fibers can be filled with various materials which enable their use in tuning, switching, and nonlinear optics [52-54].

So far, I have mainly discussed optical fibers that confine light in the core region based on TIR. There is another important type of fibers called Hollow Core Fibers (HCF). Because the solid core in conventional fibers is the main factor that affect the fiber loss (e.g. Rayleigh scattering and phonon absorption), research was undertaken to demonstrate HCF as a means to produce a lower loss fiber. [55]. Theoretically, HCF may guide light with several orders of magnitude lower loss than conventional fibers [55] but thermal excitation at the fabrication process causes roughness at the core boundary and that increases their loss [56]. In a HCF, light can be confined in the air or vacuum core and transmitted with low loss. TIR is not a valid explanation of the light propagation in these fibers because the refractive index of air or vacuum is lower than the solid cladding. The Bell Telephone Laboratories developed the first commercial hollow-core waveguide system (WT4/WT4A millimeter-wave transmission system) for telecommunication in 1970s for microwave electromagnetic signals [57]. Later in 1980s, the first metal hollow-core waveguide was developed that was capable of working at optical frequencies [58].

Research on the development of dielectric HCFs resulted in the demonstration of hollow-core Photonic Band Gap Fibers (PBGF) [59, 60]. Dielectric materials have very good transparency at optical wavelengths making them attractive candidates as guiding media for gaseous amplifiers [61]. Unfortunately, dielectric HCF only have high reflectivity over a narrow bandwidth because most dielectric materials have strong phonon absorption at long wavelengths. Dielectric HCF also have lower transmission because of their leaky confinement, making them unsuitable for use in long distance optical transmission. For PBGFs, there is a gap in frequency range, where light is

forbidden to propagate in the media. A typical SEM image of a PBGF and its guiding mechanism are shown in Figure 3.4. The term “bandgap” comes from solid state physics, which refers to an energy gap in a solid where electron states are forbidden to propagate. The first PBGF was demonstrated in 1999 [59]. PBGFs are independent of TIR and light mainly propagates in the air/vacuum core regardless of the difference between refractive indices of core and cladding. There is small overlap between core mode and cladding modes. Figure 3.5 summarizes the process of fabricating PBGFs by pressurization [62].

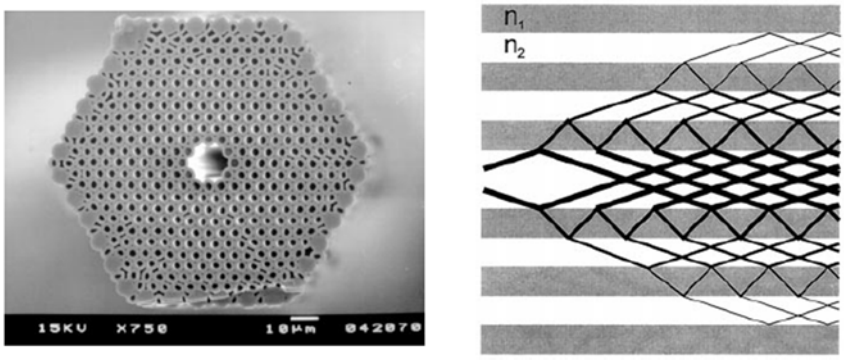

Figure 3.4: SEM image of a PBGF and its guiding mechanism based on constructive and destructive interference of the core mode and cladding modes [59].

To summarize PBGFs, they are low loss but narrow bandwidth, limiting their widespread application. As an example, PBGF’s have been demonstrated to operate around 3 μm, but their bandwidth is limited to less than an octave. As we need more than this for our acetylene-filled HOFGLAS, we must look to a different fiber design for our application.

In 2002, a new type of HCFs called Kagome-structured HCFs was demonstrated by Benabid et. al. [63]. Figure 3.6 shows a typical Kagome-structured HCF. They contain a periodic lattice in the cladding area and no photonic bandgap. They guide light through a mechanism akin

to Von Neumann and Wigner states [64] allowing both the core mode and cladding modes to exist at a certain wavelength with very low coupling.

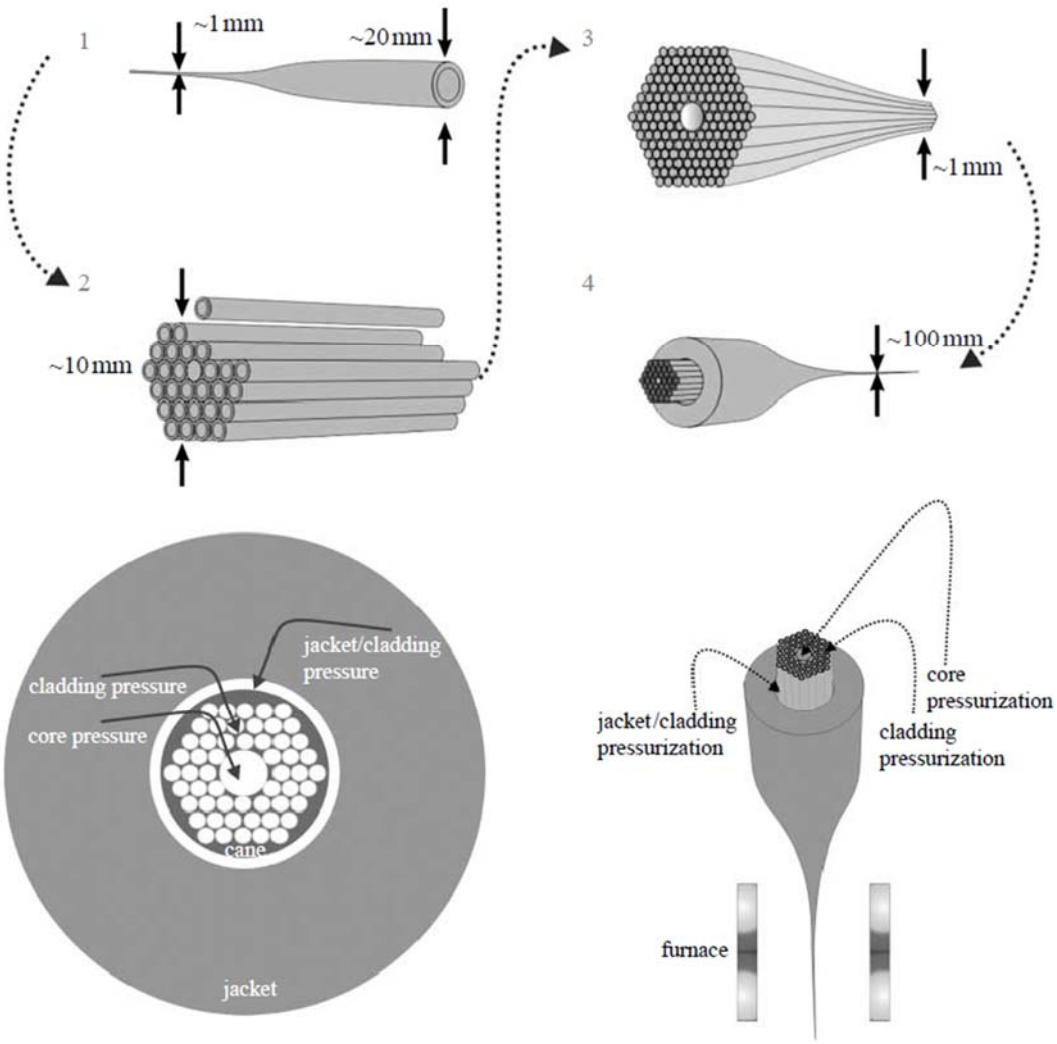

Figure 3.5: Fabrication and pressurization of PBGF, picture is cited from reference [62].

The name "Kagome" is related to their cladding structure which looks like a Kagome basket. These fibers can be spliced to solid-core fibers as well. Kagome HCFs are ultra-broad bandwidth and they have several transmission bands. This and the fact that we can pump in near-

IR and see lasing in mid-IR is the main reason we use these fibers in our acetylene-filled HOFGLAS system. Since there is no PBG in the cladding, these fibers have higher loss than conventional fibers. The main contributor to the loss in a Kagome fiber is the core size, and it has been found that a smaller core increases the loss [65].

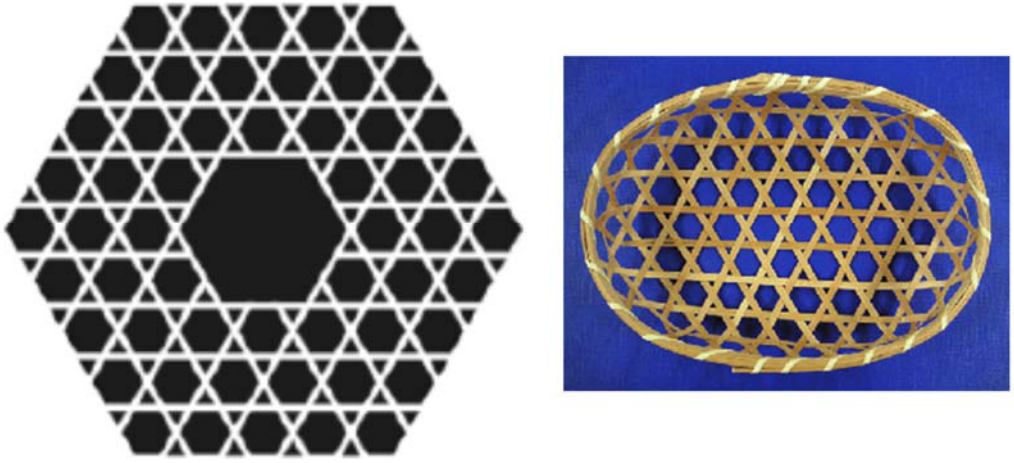

Figure 3.6: Kagome HC-PCF sketch, cited from reference [49] Kagome basket is shown on the right which is the reason for the name of these fibers, reproduced from reference [66].

In 2010, Wang et. al. [67] discovered that designing a kagome-structured HCFs with a negative curvature core boundary reduces the loss compared to a regular kagome fiber. A typical SEM image of negative curvature kagome HCF is shown in Figure 3.7.

A few months later, Gerome et. al. [68] reported that negative curvature Kagome fibers decrease the overlap of the core mode with the cladding modes and allow for their higher propagation transmission. The first fused silica kagome fiber with negative curvature was fabricated in 2011 [69] and the SEM image of this fiber is shown in Figure 3.8. Later, Chalcogenide glass kagome fiber with negative curvature was fabricated [70].

Attempts were later made to fabricate lower loss silica kagome fibers with negative curvature for the mid-IR [8, 71]. These fibers have been used for many applications such as surgical laser procedures and high precision micro machining applications [72, 73].

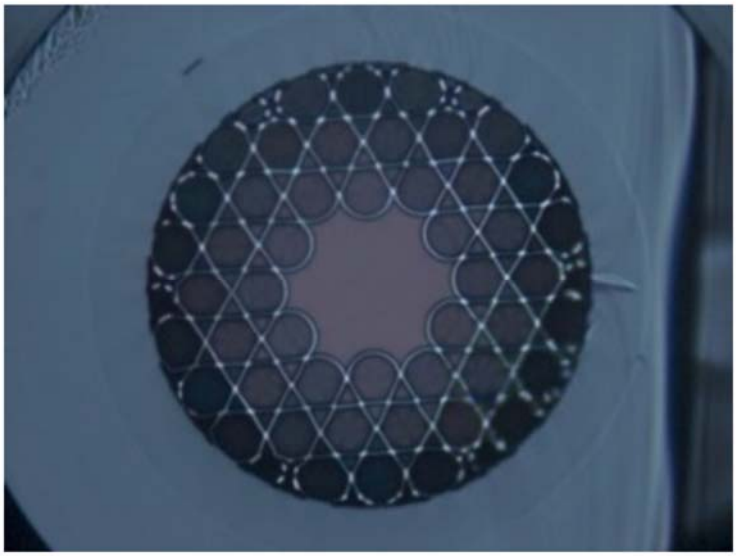

Figure 3.7: SEM image of negative curvature Kagome HCF. This picture is the cross section of a seven-cell three-ring fiber, which was sent to us from Xlim research institute.

HC-PCFs are used in nonlinear optical phenomena such as high energy soliton formation, precision saturated absorption spectroscopy, the development of a gas-filled fiber Raman laser, and multi-octave spanning Raman frequency combs. In this dissertation, their application in demonstrating gas-filled hollow fiber lasers is highlighted.

Our collaborator, Dr. Fetah Benabid from Xlim research institute in France, provide us with low loss negative curvature kagome fibers in the mid-IR. Since these fibers are made from silica, they begin absorbing above ~ 2.5 μm. So, these fibers have been optimized for operation at visible and near infrared wavelengths. Fiber fabricators have been using finite element analysis

software, like JCMwave, to optimize fiber loss in mid-IR region. Since it is computationally challenging to calculate the loss for these fibers, the fabricators use empirical rules to engineer new designs for low loss fibers. Therefore, they only have an estimation on the loss of these silica kagome HCFs.

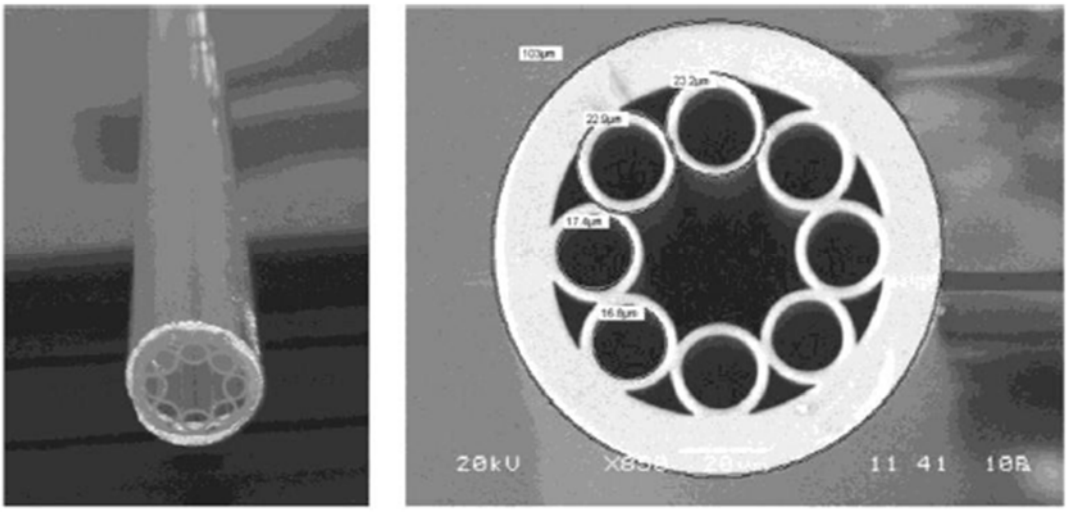

Figure 3.8: SEM image of the first silica negative curvature kagome HCF with less complicated cladding structure [69].

In order to choose the best fiber to run our acetylene-filled HOFGLAS system, the loss of our negative curvature kagome HCFs in the mid-IR was measured by performing fiber loss cut-back measurements. Also, we provide our collaborators with the mid-IR loss spectrum so they can compare our measurements to their estimations. So, in addition to choosing the best fiber to run our acetylene HOFGLAS, we have also contributed indirectly to the fabrication of lower loss fibers in the mid-IR.

3.2. Mid.IR fiber loss measurements

Results of mid-IR fiber loss measurements for a 2011 batch of Kagome HC-PCF using the idler of our homebuilt OPA are reported in reference [74]. Observing a few negative values for fiber loss during these measurements, a strong indication that our measurements are flawed, indicates problems in performing loss measurements using the idler source. Later, a blackbody radiation source was used to perform mid-IR loss measurements and some technical problems on the set up such as observing a water absorption peak in the monochromator or facing monochromator broken gear were reported [75]. Later, problems were fixed and mid-IR fiber loss measurements were performed using this method for some fibers. For smaller core size fibers, this method was not responsive because the light from the thermal source with extended area did not couple well for them. For the rest of the fibers, the output of our acetylene-filled HOFGLAS was used, which works at two mid-IR wavelengths, for the cut-back measurements. In the following sections, my contribution in each of these methods of mid-IR fiber loss measurements are explained.

3.2.1. Mid-IR fiber loss measurements using idler of OPA

The HC-PCFs were received from our collaborators, Dr. Fetah Benabid, at Xlim research institute joint between the CNRS and the University of Limoges in France. The loss in mid-IR can be predicted based on estimations and scaling methods by our collaborators. Their characterizations of the fiber losses are for the near-IR and visible regions of light while we provide the measurements for the mid-IR. We could then provide them with the fiber's mid-IR loss information for them to compare to their estimated loss spectrum. Once the fibers loss information is known, the lowest loss fibers can be used for our HOFGLAS systems and better experimental results can be obtained. Table 3.1 is a list of Kagome HC-PCFs and negative curvature Kagome

HC-PCFs with hypocycloidal core shape that were used in mid-IR loss measurements using the idler of the OPA.

The results of these measurements are published in reference [74] and fiber #6, the highlighted row, was installed in acetylene-filled HOFGLAS later since the measured loss at mid-IR was lower than the rest of the fibers.

Table 3.1: List of Kagome HC-PCFs received in 2011 from Dr. Fetah Benabid. Some of the fibers are Kagome with 7 missing cells and 3 rings in the cladding area and some are Kagome with 1 missing cell and 1 ring in the cladding area with hypocycloidal core shape.

#	Fiber Structure & Part Number	Year	Inner Core Diameter (μm)	Initial length (m)	Loss at 1.5 μm (dB/m)	Loss at ~3.1 μm (dB/m)
1	110727-CFD-K7C3RC11J11/ Kagome	2011	85	2	0.122	2.5
2	110903-CFD-K7C3RC20J8/ Kagome	2011	112.5	10	0.267	10
3	110727-CFD-K7C3RC3J16/ Kagome	2011	85	10	0.3	5
4	110708-CFD-K7C3RC5J5/ Kagome	2011	87.5	10	0.237	3
5	110811-YYW1RD1C6B2/ Hypocycloid	2011	58	3	-	5
6	110811-YYW1RD1C6B1/ Hypocycloid	2011	64	5	4	2

The approach to measure mid-IR fiber loss is the standard cut-back measurement technique. It is important to choose a source covering the mid-IR range and a detector with a good responsivity in the mid-IR. In the cut-back measurement method, the transmission of the light source through the initial length of the fiber is measured first. Then, without changing the light coupling into the fiber a specific amount of fiber from the exit port of the fiber is cut and the light transmission through the fiber is measured again, as shown in Figure 3.8.

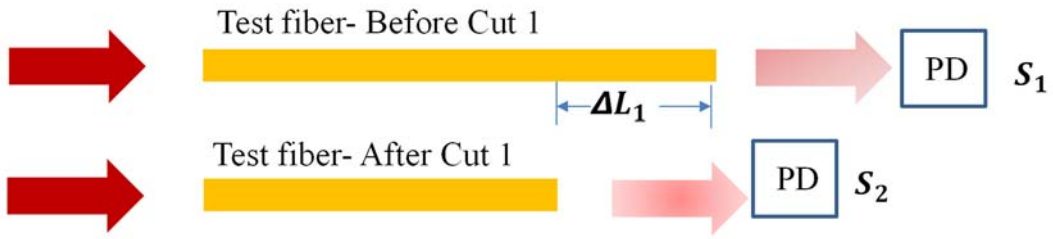

Figure 3.9: Cut back measurement technique with one cut. ΔL_1 is the first cut. PD is the photodetector. S_i where "i" is 1, 2 are the transmitted signal measurements.

Then, the fiber loss in terms of dB/m can be calculated [76] using Equation 3.2.

$$\alpha = -\frac{10}{\Delta L_1} \times log_{10}(\frac{S_2}{S_1}) \tag{3.2}$$

The error bars can be calculated [75] using Equation 3.3.

$$\text{error bar} = \sqrt{(\frac{d\alpha}{dS_1})^2(\Delta S_{1,\text{error}})^2 + (\frac{d\alpha}{dS_2})^2(\Delta S_{2,\text{error}})^2 + (\frac{d\alpha}{d\Delta L_1})^2(\Delta L_{1\ \text{error}})^2} \tag{3.3}$$

By taking the differential from Equation 3.2 in terms of S_1, S_2, and ΔL_1 the terms in Equation 3.3 are found.

$$\frac{d\alpha}{dS_1} = \frac{10}{\Delta L_1 \times S_1 \times \text{Ln}(10)} \tag{3.4}$$

$$\frac{d\alpha}{dS_2} = \frac{10}{\Delta L_1 \times S_2 \times \text{Ln}(10)} \tag{3.5}$$

$$\frac{d\alpha}{d\Delta L_1} = -\frac{10}{\Delta L^2} \times \log_{10}\left(\frac{S_2}{S_1}\right) \tag{3.6}$$

The fiber loss in terms of dB/m and the error bars were calculated for each wavelength in the mid-IR and were plotted in Origin software.

The OPA is explained in section 4.3 in details. The idler of the OPA can cover the range of wavelengths from 2.3 µm to 3.6 µm depending on the crystal poling period (**Λ**) and temperature as shown in Figure 3.10.

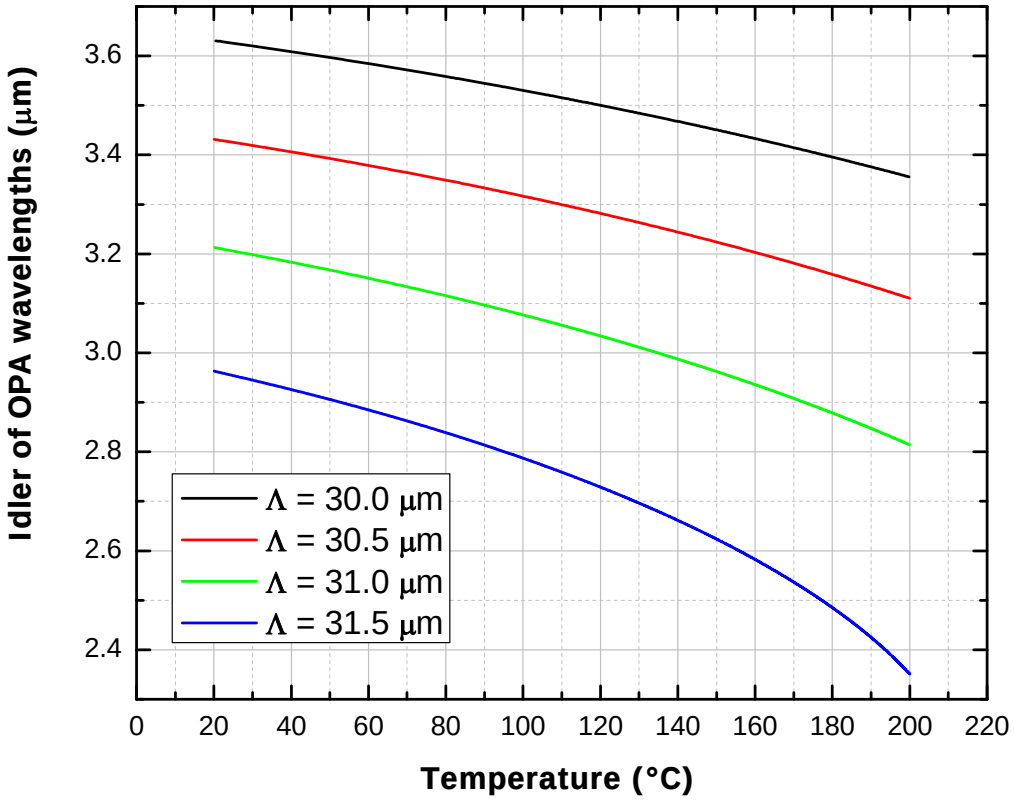

Figure 3.10: Idler of OPA may generate nanosecond pulses from almost 2.3 µm to 3.6 µm at various combinations of crystal poling period and temperature. Crystal poling period is Λ. The figure is reproduced from Ref. [74].

The mid-IR loss spectrum of a number of fibers from 2011 using the idler of the OPA were measured. Later, a tested hypocycloidal core shape kagome-structured fibers with measured loss of less than 5 dB/m in the mid-IR was used in the acetylene HOFGLAS system. This fiber had a 64 μm inner core diameter and 4 dB/m loss at 1.5 μm pump wavelength. The longest remaining piece of this fiber after cut-back measurements was used to operate the acetylene-filled HOFGLAS laser.

A schematic of the fiber loss cut-back measurement using idler is shown in Figure 3.11. Although the cut-back measurements were performed very carefully, the input light coupling into the fiber is changed by tuning the crystal temperature and poling period. This is against the principle of cut-back measurements. The coupling loss must be separated from fiber loss and to do so the light coupling efficiency should remain constant during the measurements. The observation of some negative values for fiber loss during these measurements were an evidence of the above statement. So, a thermal light source was used later to perform mid-IR cut-back measurements.

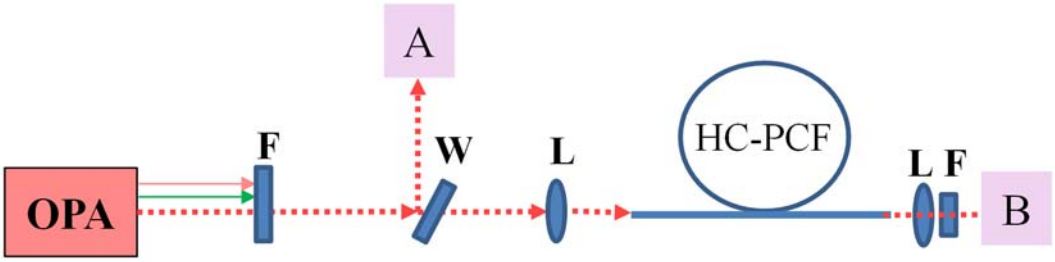

Figure 3.11: Fiber loss measurement setup using the idler of the OPA. The idler of the OPA is separated from other OPA outputs using appropriate long pass filter (F). We used a window (W) to keep track of idler fluctuations using a PD (HgCdTe IR PD, PVI series, Boston Electronics). Beam has been focused on the HC-PCF and at the output we used a collimating CaF_2 lens and appropriate ND filters. IR PD, PVI-2TE series, from Boston Electronics was used at B and measured the transmitted light, appendix A (a).

3.2.2. Mid-IR fiber loss measurements using Blackbody commercial source

Another batch of Hypocycloidal core-shape negative curvature Kagome fibers was received from Dr. Fetah Benabid in 2012. The fibers are listed in Table 3.2.

Table 3.2: List of Kagome HC-PCFs received in 2012 from Dr. Fetah Benabid. Some of the fibers are Kagome with 7 missing cells and 3 rings with hypocycloidal core shape in the cladding area and some are Kagome with 1 missing cell and 1 ring in the cladding area with hypocycloidal core shape.

#	Fiber Structure & Part Number	Year	Inner Core Diameter (μm)	Initial length (m)	Loss at 1.5 μm (dB/m)	Loss at ~3.1 μm (dB/m)
7	120221-CFD-K7C3R-C15J03-fibre-1 Hypocycloid	2012	82	10	-	-
8	fiber: 120223-CFD-K7C3R-C32J03-fibre-3 Hypocycloid	2012	84	10	-	-
9	12023-CFD-K7C3R-C32J03-fibre-2 Hypocycloid	2012	80	10	-	-
10	120221-CFD-K7C3R-C15J03-fibre-2 Hypocycloid	2012	80	10	0.0966	0.8
11	120314-CFD-K1C6R-C15J16 (fiber1) Hypocycloid	2012	29	5	0.1	-
12	120314-CFD-K1C6R-C15J16 (fiber2) Hypocycloid	2012	28	5	2	-
13	120314-CFD-K1C6R-C14J14 (fiber 1) Hypocycloid	2012	29	5	2	-

A commercial blackbody radiation source was purchased from Ocean Optics, called Coolred, and the spectrum of this source is shown in Figure 3.12. This blackbody radiation source

covers the mid-IR wavelength range of interest. We couple the light emitted from this source into the test HC-PCFs and put the exit port of the fiber in front of our monochromator, as shown in Figure 3.13. The collimated beam enters the monochromator through the entrance slit and propagates all the way through the monochromator.

A Bragg Grating inside the monochromator selects a certain wavelength and a photo detector (PDA20H model from Thorlabs) at the exit slit of the monochromator detects the light. The photosensitivity of this PD is for the range of 1.5 μm to 4.5 μm.

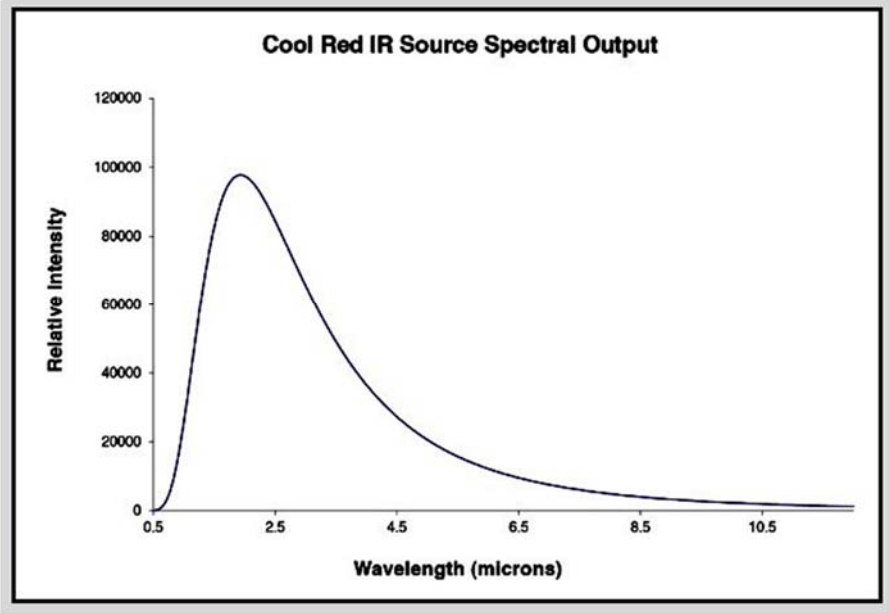

Figure 3.12: Ocean Optics's Coolred spectrum taken from company's website. This blackbody radiation source covers the mid-IR range (http://www.acalbfi.com/uk/Photonics/Spectroscopy/Light-sources-and-accessories/p/Infrared-Light-Sources--Cool-Red/0000001W1T_).

The Monochromator's grating can move by 23 steps per nanometer and it is controlled by a HyperTerminal program on a laptop so that we can scan over a range of wavelengths, appendix A(b).

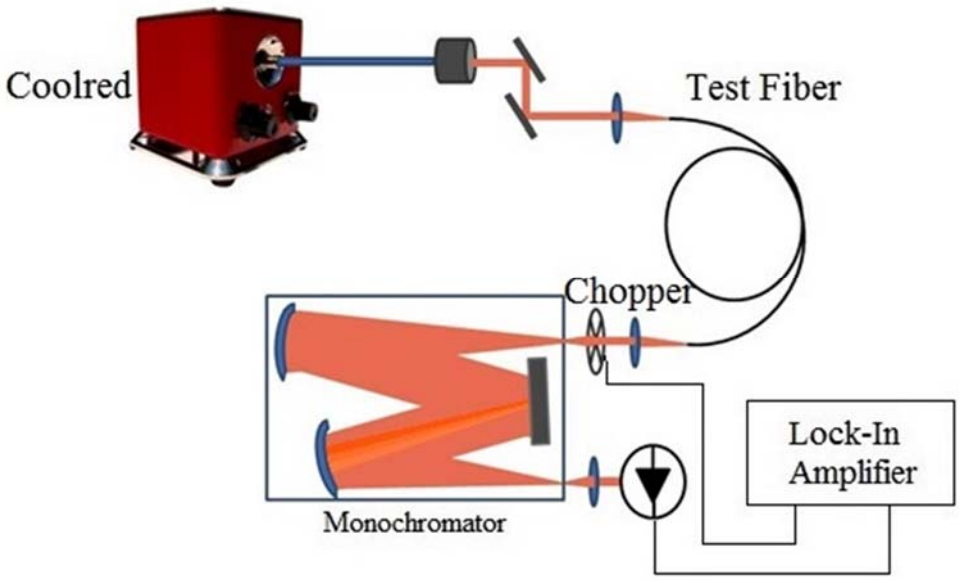

Figure 3.13: Fiber loss measurement setup using a blackbody radiation source (Coolred from Ocean Optics). See text for details.

As it is shown in Figure 3.13, the beam is coupled into the fiber using a CaF_2 plano convex lens of focal length 25 mm in a two-axis lens mount from Thorlabs. The focusing lens focal length matches the test fiber's NA and is optimized for coupling the fundamental mode of the 3 μm wavelength from the Blackbody source into the Kagome HC-PCF. The exit port of the fiber is supported two times by V-grove fiber holders from Newport company so that the entrance side of the fiber remains unchanged as we cut and cleave the fiber from that side. We also make sure not to put too much tension on the fiber. The fibers are coiled on a fiber spool to minimize bending loss of the fibers. A CaF_2 lens is used to collimate the exit beam and send it to the monochromator. The fiber entrance and exit ends are on three-axis fiber stages from Newport. The collimating lens is also in a two-axis lens mount from Thorlabs. The NA of the fiber, collimating lens focal length, monochromator's slit opening, and f/10 monochromator all are in agreement to have perfect beam

propagation inside the monochromator. Since there is only a small amount of coupling of the blackbody radiation source into a single mode HC-PCF, we use a lock-in detection system to measure the weak signal after the monochromator. We used a lock-in amplifier, SR510 model, from "Stanford Research Systems". The lock-in amplifier filters out the noise and amplifies the signal that is in phase with the chopper frequency (reference frequency), as shown in Figure 3.14.

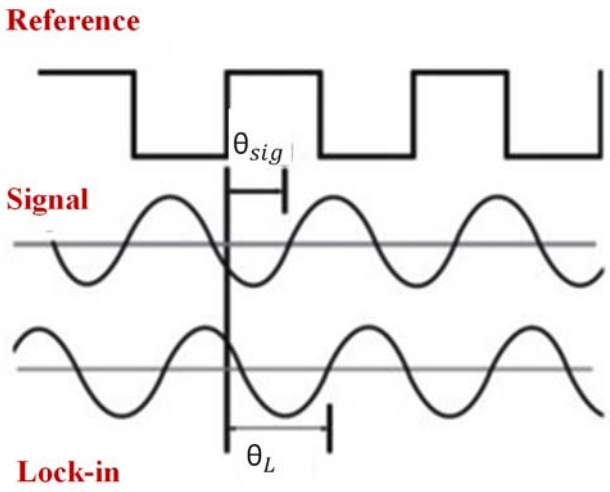

Figure 3.14: Lock-in amplifier: the "Reference" signal is a square wave with frequency ω_r that comes from a chopper in our set up. The "Signal" is S_{sig} Sin ($\omega_r t+\theta_{sig}$) where θ_{sig} is the signal phase and ω_r is the signal frequency defined by the chopper too. Lock in amplifier generates its own internal reference signal which is S_L Sin ($\omega_L t+\theta_L$).

The way a lock-in works is that it amplifies the signal and then multiplies it by the lock-in internal reference signal using a multiplier as shown here:

$$S_{output} = S_{sig} S_L \mathrm{Sin}(\omega_r t + \theta_{sig}) \mathrm{Sin}(\omega_L t + \theta_L) \tag{3.7}$$

$$S_{\text{output}} = \frac{1}{2} S_{\text{sig}} S_L \text{Cos}\left((\omega_r - \omega_L)t + \theta_{\text{sig}} - \theta_L\right) - \frac{1}{2} S_{\text{sig}} S_L Cos((\omega_r + \omega_L)t + \theta_{\text{sig}} + \theta_L) \quad (3.8)$$

Then the output goes through a low pass filter and both of the AC signals will be removed unless ω_L will be equal to ω_r . In this case, a DC signal, as shown in Equation 3.9, remains. Otherwise, no signal will be measured.

$$S_{\text{output}} = \frac{1}{2} S_{\text{sig}} S_L \cos(\theta_{\text{sig}} - \theta_L) \quad (3.9)$$

I performed the cut back measurement from the side of the fiber, which is in front of monochromator so input beam coupling efficiency remains constant during all measurements. We used this method for fibers with #s 7 to 10 from Table 3.2. After fixing the setup problems, the mid-IR loss spectrum for the hypocycloidal fiber #10 with core size of 80 μm is measured and it is shown in Figure 3.15. The initial length of the fiber was 490 cm. I performed the first cut for 146 cm and the second cut for 136 cm (Green and Blue curves in Figure 3.15). We also consider a total cut of 282 cm (136cm+ 146 cm) shown as the black curve in Figure 3.16.

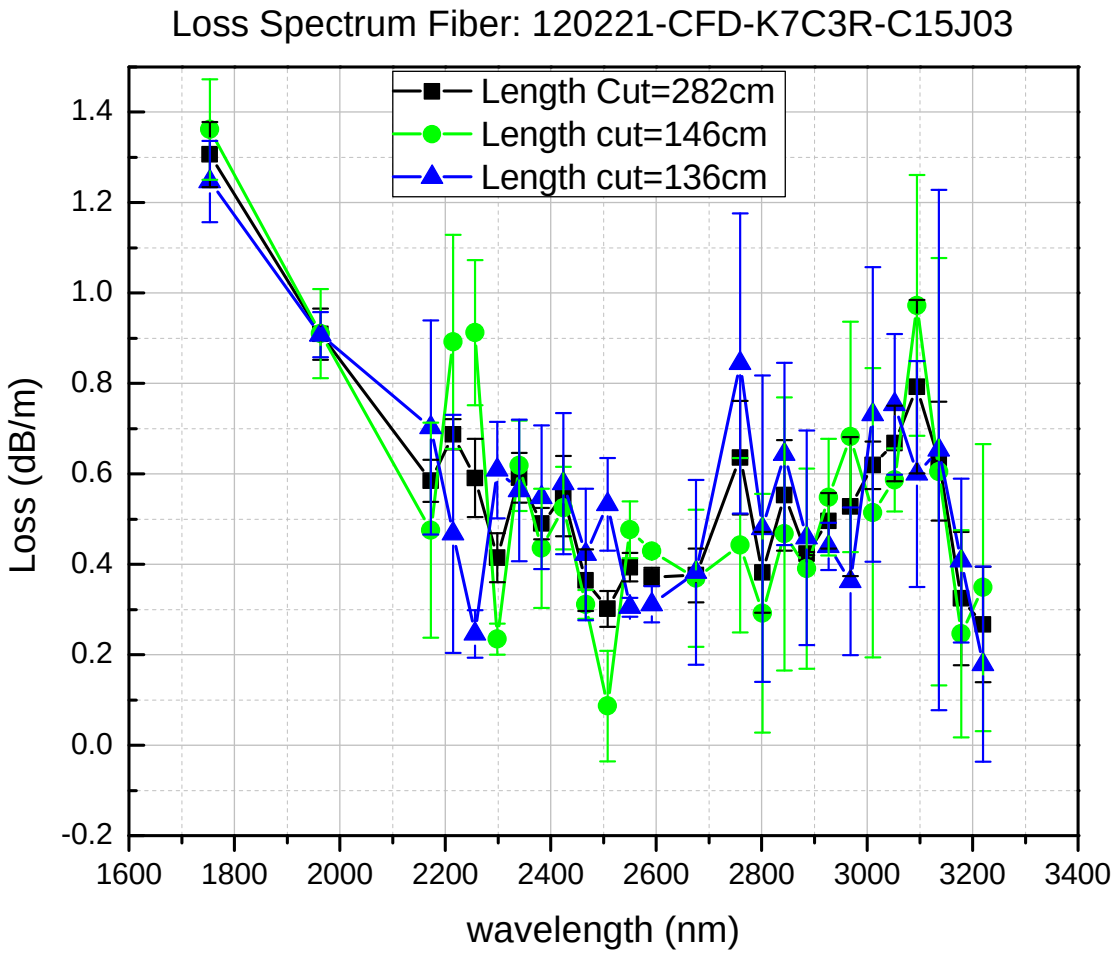

Figure 3.15: mid-IR fiber loss spectrum for a negative curvature Kagome fiber with core size of 80 µm. The fiber part number is: 120221-CFD-K7C3R-C15J03. Two cut-backs were performed (green : 146 cm and blue: 136 cm) and the black is the fiber loss spectrum for the overall cut between initial length of fiber and final length (146 cm + 136 cm= 282 cm).

By looking at the spectrum of mid-IR fiber loss after the total amount of fiber cut in Figure 3.16, no negative value has been observed and the coupling efficiency stayed constant during the measurements.

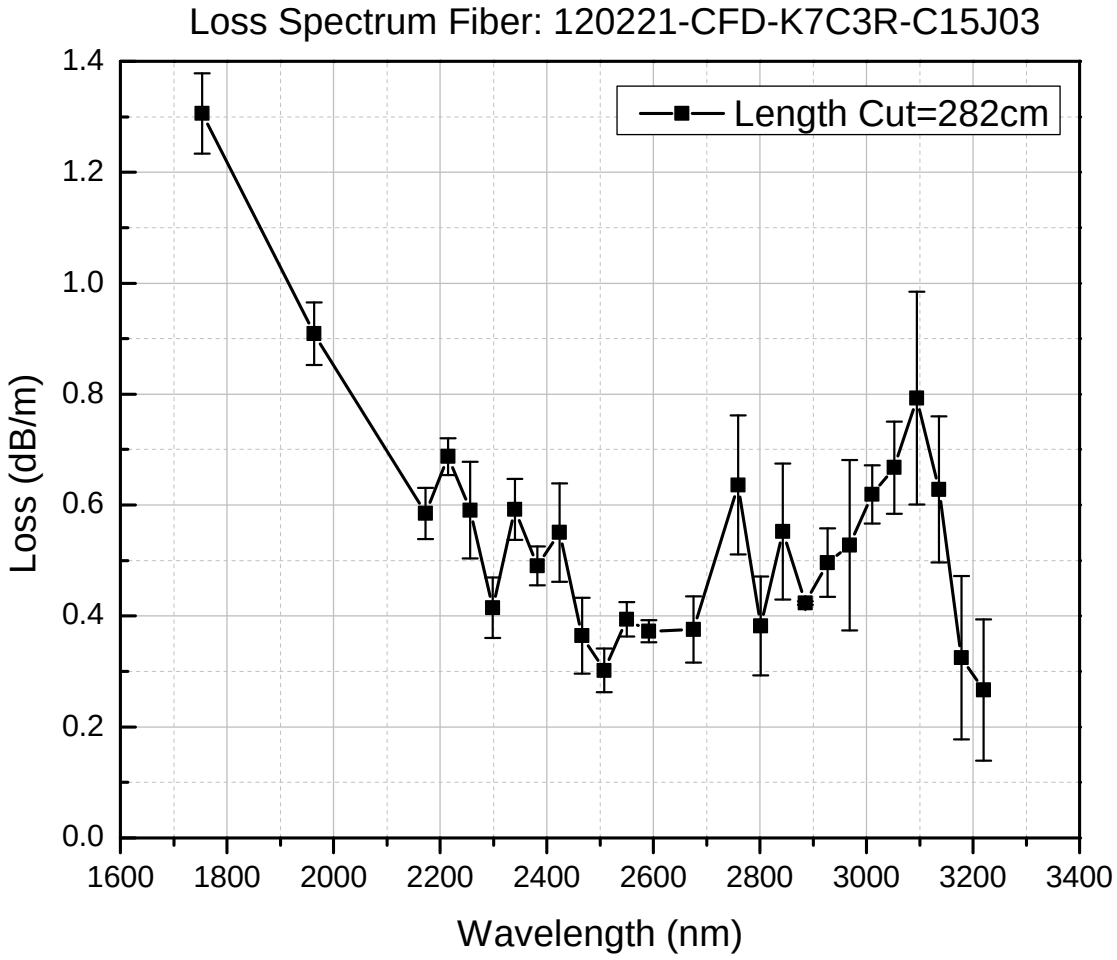

Figure 3.16: mid-IR fiber loss measurement for the negative curvature Kagome fiber with core size of 80 µm. The fiber part number is: 120221-CFD-K7C3R-C15J03. This shows the fiber loss spectrum for the overall cut between initial length of fiber and final length (146 cm + 136 cm= 282 cm).

Fibers with #s of 11, 12, and 13 from Table 3.2 have a core size of about 29 µm and it was not possible to get enough coupling of the blackbody source into these fibers so we used the output of our acetylene-filled HOFGLAS, as explained in section 3.2.3., to measure the mid-IR loss for these very single mode fibers.

3.2.3. Mid-IR fiber loss measurements using Acetylene HOFGLAS output

For Kagome fibers with Inner core size of less than 80 µm, we use the output of our acetylene-filled HOFGLAS as the source to perform mid-IR cut-back measurements. We received two fibers in 2015 as listed in Table 3.3. The fiber #15, with the Inner core size 60/72 µm, was immediately installed in acetylene-filled HOFGLAS setup because it had an 11 meter length and we wanted to study the effect of fiber length on the HOFGLAS operation. As the mid-IR loss of this fiber was needed, another piece of similar fiber was requested from collaborators. In 2016, fiber #17 with similar characteristics was received.

Table 3.3: List of received hypocycloidal core-shape Kagome fibers from France in 2015 and 2016.

#	Fiber Structure & Part Number	Year	Inner Core Diameter (µm)	Initial length (m)	Loss at 1.5 µm (dB/m)	Loss at 3 µm (dB/m)
14	I1501 Hypocycloid	2015	49/62	10+11	-	-
15	H6510 Hypocycloid	2015	60/72	11	0.08	1.13
16	I9610B2 Hypocycloid	2016	30	10	0.14	-
17	J1601B2 Hypocycloid	2016	63/75	10	0.06	1.13

The loss of fiber #15 (& #17) was measured using mid-IR output of Acetylene-filled HOFGLAS as shown in Figure 3.17. We keep track of the mid-IR beam fluctuations as well. The measured loss for fiber #17 is measured to be 1130 dB/km at 3.1 µm (Kushan Weerasinghe performed this loss measurement).

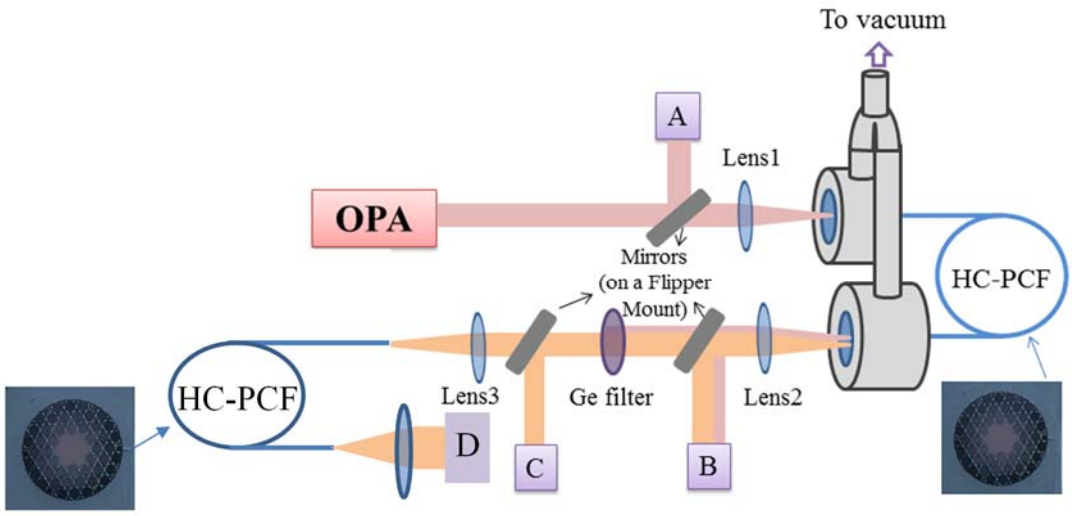

Figure 3.17: fiber loss measurement using mid-IR output of acetylene-filled HOFGLAS. Residual pump is filtered out from the mid-IR produced beam using a germanium filter and fluctuations of the beam can be tracked at C. A CaF_2 lens was used to couple the beam into the test HC-PCF and the transmitted exit beam can be collimated and detected at D.

3.2.4. Conclusion of mid-IR loss measurements

To summarize this chapter, the biggest challenges in performing cut-back measurements in the mid-IR are the source and the detection system. A TEC-cooled IR photo detector (PVI-2TE series, Boston electronics) was used as the detection system. The main challenge is having a light source that covers the mid-IR light region. Three different mid-IR sources were used. The first method, which was using OPA idler, gives an estimation for fiber loss in the mid-IR, but is imprecise for cut-back measurement since the coupling into the fiber entrance changes as the OPA's temperature and poling period are tuned. Second round of cut-back measurements in the mid-IR was performed using a black-body radiation source (Coolred from Ocean Optics company) that covers the mid-IR range along with a monochromator at the exit port of the fiber. This method works well for larger core fibers but measurement of the loss of more single mode fibers was

difficult using this method due to a low amount of light coupling from the thermal source into a nearly single mode fiber. Finally, the stable output from the acetylene-filled hollow-core fiber laser system was used as the mid-IR source to measure fiber loss for all the small core size hollow-core photonic crystal fibers and this method was successful when we kept track of laser stability by looking into the input mid-IR beam fluctuations before the entrance of the test fiber.

Chapter 4 - Operation of the acetylene HOFGLAS

Our group has created a new class of lasers known as Hollow-core Optical Fiber Gas LASer (HOFGLAS) which are based on population inversion [8]. I continued exploring HOFGLAS by studying the performance and scalability of gas-filled hollow-core photonic crystal fiber lasers [25, 77-80]. In particular, I was able to improve the stability, efficiency, and output power of an OPA pumped acetylene-filled HOFGLAS based on population inversion. The power scalability of this system from only a few nJ to μJ level is highlighted. We also demonstrated many novel properties of acetylene-filled pulsed mid-IR hollow-core fiber lasers. The phenomenological scaling of saturation power and efficiency with pressure promise higher power sources in the future. This is a motivation to develop numerical models of the laser for deeper insight into these effects. In this chapter, we take steps toward characterizing and improving the performance of acetylene-filled HOFGLAS.

4.1. Acetylene-filled HOFGLAS Setup Overview

The OPA-pumped acetylene-filled HOFGLAS setup is shown in Figure 4.1. The 1.5 μm OPA pulses with pulse duration of ~ 1 ns and repetition rate of 30 Hz are coupled into the hollow-core photonic crystal fiber while both ends of the fiber are inserted inside vacuum chambers so they can be filled with acetylene gas at the desired pressure. The seed laser for the OPA is tuned on resonance with the P(13) absorption line of acetylene. Population inversion between the rotational-vibrational states of the molecular gas results in lasing at 3.11 μm and 3.17 μm wavelengths. Sensitive pyroelectric energy meters measure the 1.53 μm and produced 3 μm pulse energies at different points of the laser configuration. A germanium (Ge) filter is used for filtering off the residual 1.53 μm pump from the produced 3 μm output laser. The performance of the laser

is characterized for various acetylene pressures in the fiber at different input pump energies in terms of the output mid-IR energy.

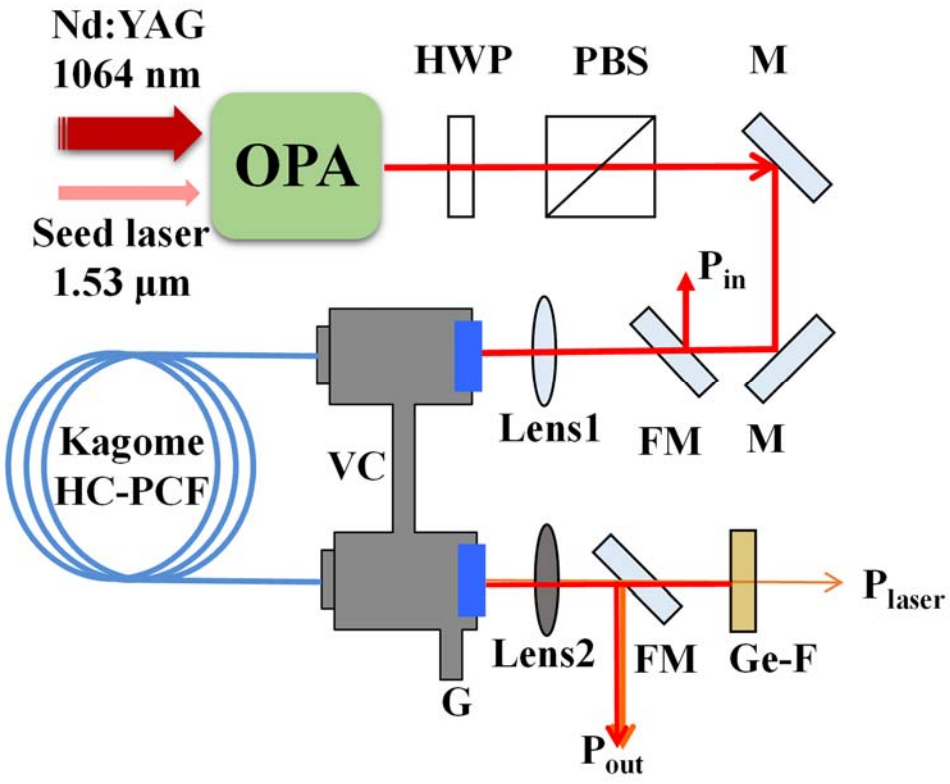

Figure 4.1: Pulsed HOFGLAS setup. The OPA is used as the pump source for HOFGLAS. The seed laser to the OPA is a continuous wave diode laser at 1532 nm and the pump laser to the OPA is a Q-switched Nd:YAG laser at 1064 nm. The HWP and PBS are used to control the input power that is sent to the vacuum chambers. Gas is contained inside hollow-core photonic crystal fiber. Mid-IR light passes through a 2-mm thick, uncoated germanium filter at 90 degree and is detected by pyroelectric energy meter. Two flipper mirrors are used to keep track of pump power and superposition of residual pump and 3 µm power before and after the vacuum chambers. Lens2 is from CaF_2 material and Lens1 is a BK7 lens.

The gas is allowed to reach equilibrium through the length of the fiber over a span of a few hours. I will explain in section 4.2. of this chapter how we estimate the time for reaching the equilibrium condition.

4.2. Equilibrium condition for Acetylene molecules in HC-PCF

The hollow core fiber is filled with gas and the pressure gauge is initially constant. This value changes with time as the distribution of gas inside the fiber reaches equilibrium. Afterwards, the pressure slowly decreases because of flows inside the vacuum chambers. The pressure value at equilibrium is reported as the exact pressure value. An example of this is shown in Figure 4.2. We show the change in pressure with time using a capacitance manometer (Baratron manometer, MKS Instruments). Initially, the pressure gauge shows a value of 1.77 torr. After about one and a half hours, the pressure drops to 1.6 torr. Later, the changes in pressure are slow with a small increase after reaching full equilibrium. We observe that the fiber is immediately filled with gas, which makes sense because the volume of the fiber is small in comparison to the volume of the vacuum chambers, Equation 4.1 and Equation 4.2.

$$\frac{V_{Fiber}}{V_{VC}} = \frac{\pi {r_{Fiber}}^2 L_{Fiber}}{\pi {r_{VC}}^2 L_{VC}} \tag{4.1}$$

$$\frac{S_{Fiber}}{S_{VC}} = \frac{2\pi\, r_{Fiber}\, L_{Fiber}}{2\pi\, r_{VC}\, L_{VC}} \tag{4.2}$$

For a typical fiber with outer radius of 180 μm and 10.9 m length and two vacuum chambers each with radius of 15 centimeters and 30 cm length, the ratio of fiber volume to vacuum chambers volume is only ~ 0.0025 %. The ratio of fiber surface area to vacuum chambers surface area will be ~ 2.2 %.

On the other hand, it takes time for the gas to reach equilibrium condition inside 10.9 m of the fiber since acetylene molecules stick to the walls of tubes, vacuum chambers, and the fiber. We tried estimating the time it takes for this to happen.

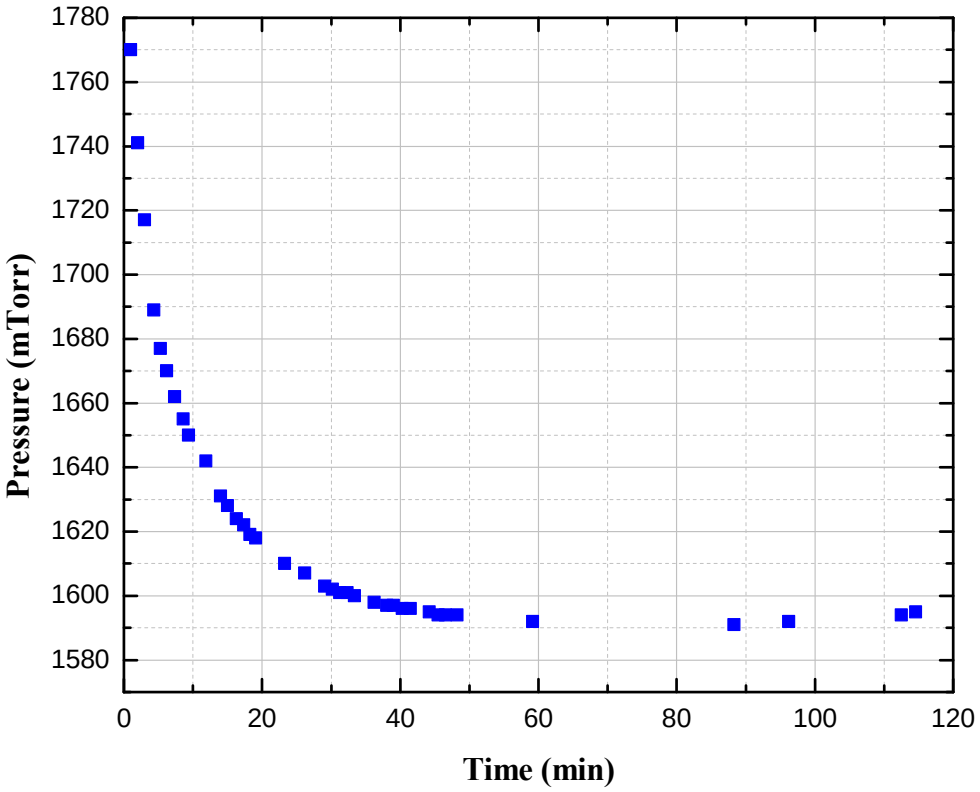

Figure 4.2: Recorded pressure from the front panel of a capacitance manometer (Baratron pressure gauge from MKS instruments) versus time recorded by stopwatch from the moment the speedy valve toward vacuum chambers gets closed and the fiber is filled with gas for about 120 minutes.

There were several experimental attempts to measure the time needed to fill the fiber with gas. One way to answer this is to monitor the Full Width Half Maximum (FWHM) and amplitude of the absorption signal of a continuous wave laser at 1532 nm (Santec, Tunable semiconductor laser, TSL-210) passing through acetylene-filled HOFGLAS. The apparatus for this measurement

is shown in Figure 4.3. We apply a ramp voltage to the fiber laser's piezo-electric transducer (PZT) which linearly scans the laser's frequency over the P(13) acetylene transition at ~1532 nm. Figure 4.4 is an example of the data recorded on an oscilloscope for applied ramp voltage (purple) to the PZT of the diode laser, transmission signal through HOFGLAS (yellow channel), and a Fiber Ring Cavity (FRC) as we scan the laser frequency for frequency calibration purposes (blue channel). The free spectral range (FSR) of the FRC is ~97 MHz for the particular FRC. As we expected, the fiber is immediately filled with gas and FWHM and amplitude of absorption values jump from zero to a certain value. This happens much faster than we can record with our setup.

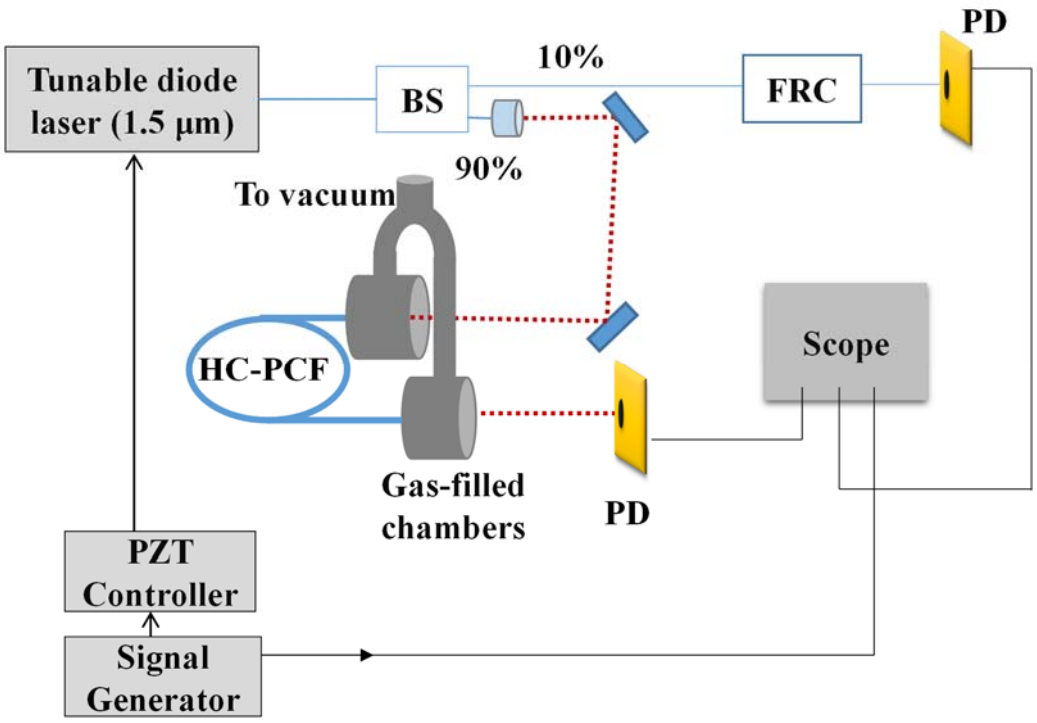

Figure 4.3: Schematic setup for measuring FWHM and amplitude of 1532 nm absorption signal by acetylene molecules, BS: Beam Splitter, FRC: Fiber Ring Cavity, PD: Photo Detector.

We were able to estimate the amount of time it takes to reach equilibrium inside the gas-filled fiber by recording the change in FWHM and amplitude of absorption signal of a 1532 nm continuous wave laser passing through the gas-filled fiber as we evacuate the fiber. The measured pressure falls to zero as the fiber is evacuated but the absorption signal remains for hours and its FWHM and amplitude change reasonably with time. Figure 4.5 is the amplitude of transmission signal through 10.9 m of acetylene-filled hollow-core fiber from the moment the speedy valve was opened over the course of 3 hours while Figure 4.6 shows the change in FWHM over the same time period.

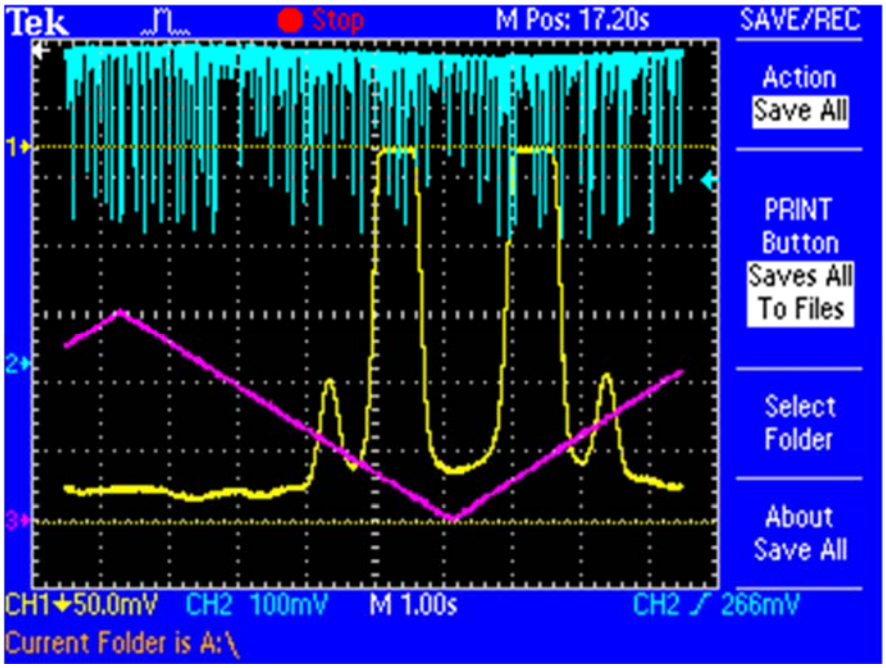

Figure 4.4: Transmission through 10.9 m acetylene-filled hollow-core fiber at 1.77 torr along with the recorded ramp voltage and fiber ring cavity data with FSR of 97 MHz.

We concluded that it takes about 160 minutes for acetylene molecules at ~1.6 torr to reach equilibrium for this particular fiber. The acetylene in the fiber is then pumped using an OPA to produce a maximum pulse energy of 21 μJ with ~1 ns pulse duration, spectral width of 440 MHz

based on the time-bandwidth product, and a repetition rate of 30 Hz at 1.53 μm. I will explain the details of the OPA pump in the following section.

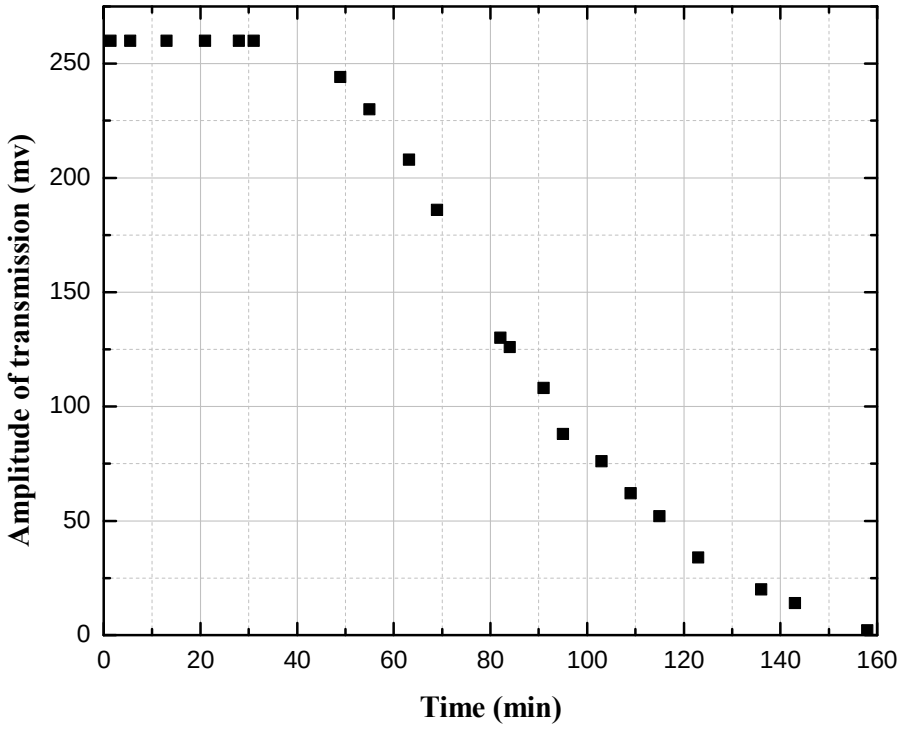

Figure 4.5: amplitude of transmission signal versus time recorded by stopwatch over the course of 3 hours.

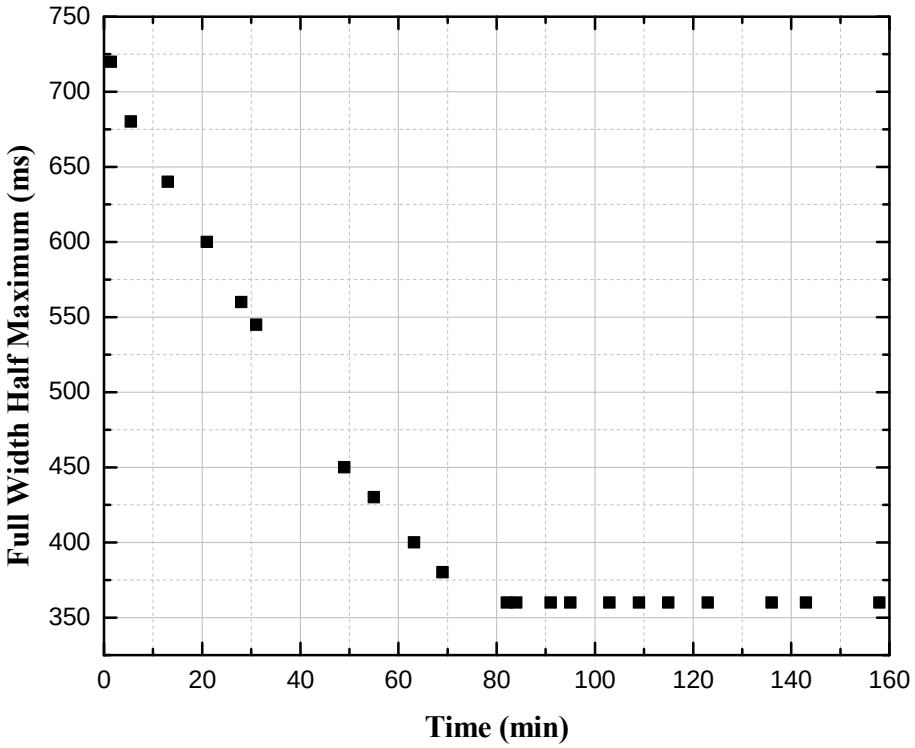

Figure 4.6: FWHM of transmission signal from 1532 nm continuous wave laser through 10.9 m acetylene-filled fiber decreases over 3 hours from the evacuation moment.

4.3. Optical Parametric Amplification

4.3.1. Nonlinear optics introduction

To pump our pulsed HOFGLAS system, a high power pump source is needed. Tunability of the high power pump source is a plus since it enables us to work with different gases and pump at the desired wavelength. An Optical Parametric Amplifier (OPA) is a convenient choice since it fulfills these requirements. This section provides a brief introduction to nonlinear frequency conversion and, specifically to the OPA .

Nanosecond laser pulses can achieve high intensities inside a media. At low intensities, the polarization depends linearly on the electric field, $P = \varepsilon_0 \chi^{(1)} E$, where $\chi^{(1)}$ is the electric

susceptibility. At high intensities, the polarization depends on higher orders of electric field as well [81],

$$P = P_1 + P_2 + P_3 + \cdots = \varepsilon_0 \chi^{(1)} E + \varepsilon_0 \chi^{(2)} E^2 + \varepsilon_0 \chi^{(3)} E^3 + \cdots \tag{4.3}$$

For simplicity, both the electric field and polarization are written as scalar quantities. The second and third terms are the nonlinear parts of the polarization. The coefficients $\chi^{(2)}, \chi^{(3)}, \ldots, \chi^{(n)}$ are higher-order nonlinear susceptibilities and these are the source terms for nonlinear processes. Consequently, new frequencies can be generated through the dependence on higher orders of the susceptibility. The simplest nonlinear process can be generated through the second-order susceptibility, $\chi^{(2)}$. Our OPA can be described entirely by second-order effects as shown in Equation 4.4 and we will focus on this term for the rest of our calculation.

$$P_2 = \varepsilon_0 \chi^{(2)} E^2 \tag{4.4}$$

The electric field can be assumed as having two components as shown in Equation 4.5.

$$E = E_0 e^{-i\omega_1 t} + E_0 e^{-i\omega_2 t} \tag{4.5}$$

If we plug this into the polarization definition, the second-order polarization becomes

$$P^2(E) = \frac{\varepsilon_0}{4} \chi^{(2)} {E_0}^2 (e^{-i2\omega_1 t} + e^{-i2\omega_2 t} + e^{-i(\omega_2+\omega_1)t} + \boldsymbol{e^{-i(\omega_1-\omega_2)t}} + 2 + c.c.) \tag{4.6}$$

Each term in Equation 4.6 describes a particular second order process. The highlighted term in the above Equation 4.6 describes difference frequency generation. Difference frequency generation is the way of generating frequency component at longer wavelength from two shorter wavelengths components. Parametric amplification can be seen as stimulated difference frequency generation. All terms of Equation 4.6 are summarized in Table 4.1.

Table 4.1: Well-known nonlinear processes

Nonlinear Processes	Phase Matching Condition
Second-harmonic generation (SHG)	$\omega_s = 2\omega_1$ or $\omega_s = 2\omega_2$
Sum-frequency generation (SFG)	$\omega_s = \omega_1 + \omega_2$
Difference-frequency generation (DFG)	$\omega_s = \omega_1 - \omega_2$
Optical parametric amplification (OPA)	$\omega_s = \omega_p - \omega_i$

In the nonlinear optical crystal, the pump photon (ω_p) decays into two less energetic photons called signal (ω_s) and idler (ω_i) so that the sum of their energies is equal to that of the pump photon, as shown in Figure 4.7.

When a specific nonlinear process is favored, we say it has been phase matched. We can determine phase matching by performing a simple calculation. First, the magnitude of wavevector, k, of an optical field is as follows:

$$k = \frac{n(\omega)\omega}{c} = \frac{2\pi n(\omega)}{\lambda} \tag{4.7}$$

Where n(ω) is the index of refraction of the nonlinear optical media at a frequency, ω. λ is the wavelength of the applied field in vacuum.

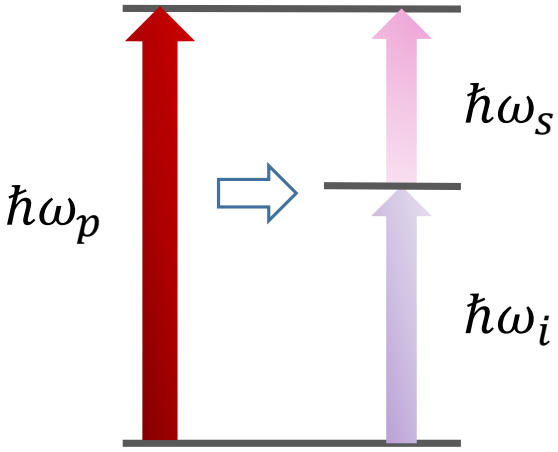

Figure 4.7: Optical Parametric process, 3-wave process.

Energy and momentum should be conserved, therefore,

$$\omega_i + \omega_s = \omega_p \tag{4.8}$$

$$\boldsymbol{k}_i + \boldsymbol{k}_s = \boldsymbol{k}_p \tag{4.9}$$

Figure 4.8 shows a schematic of phase matching in a PPLN crystal that leads to producing a pulsed signal, idler, and residual pump at the output.

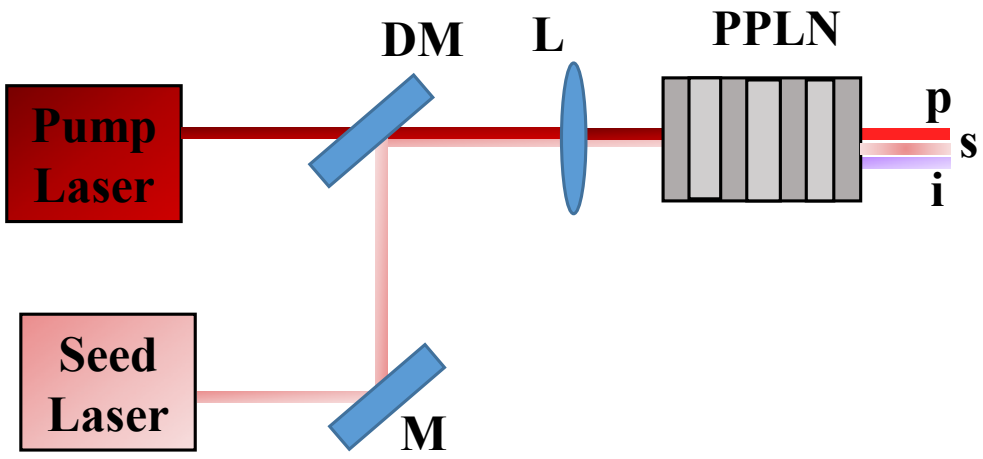

Figure 4.8: Simple schematic of Optical Parametric Amplification (OPA) using PPLN crystal.

Usually $\boldsymbol{k_i + k_s < k_p}$ because index of refraction of the media grows with ω. Therefore, this phase matching condition can never be fulfilled in isotropic crystals. However, we can fulfill this condition by using a birefringent crystal. There are two indices of refraction in different directions in birefringent crystal and by setting an appropriate temperature, they can be used for phase matching of ordinary polarized beam and extraordinary polarized beam.

Quasi-phase matching is a method in which a periodic structure of the nonlinear medium allows a positive flow of energy from higher power pump to lower power signal and idler beams described in Figure 4.9. In quasi-phase-matched crystals with periodically-modulated sign of the nonlinearity, e.g. Periodically-Poled Lithium Niobite, the artificially created grating compensates for the wave-vector mismatch. We may write the magnitude of phase mismatch for quasi-phase matching condition as shown in the Equation 4.10 and Equation 4.11,

$$k_p - (k_s + k_i) = \Delta k \tag{4.10}$$

$$\Delta k = \frac{2\pi}{\Lambda} = \frac{n(\omega_s)\omega_s}{c} + \frac{n(\omega_i)\omega_i}{c} - \frac{n(\omega_p)\omega_p}{c} \tag{4.11}$$

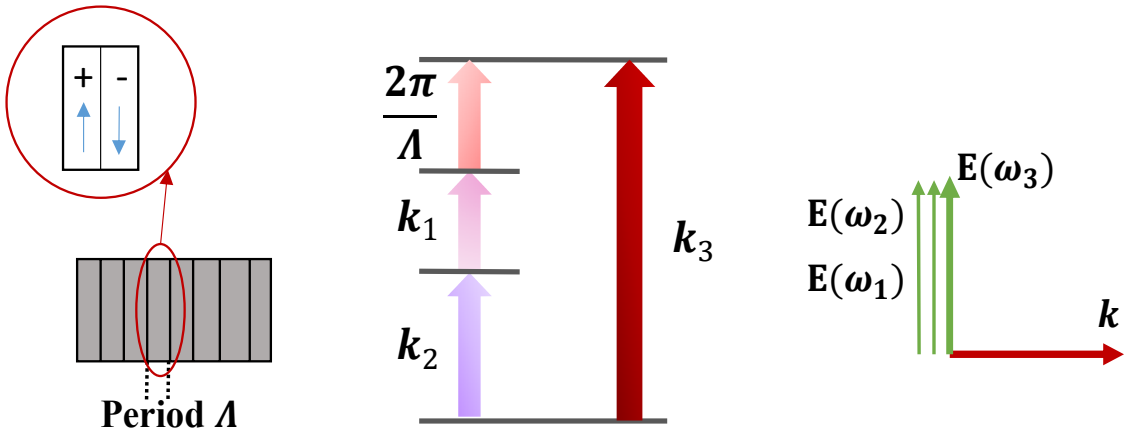

Figure 4.9: Quasi-phase matching condition, where can be related to pump frequency (ω_p), ω_2 can be related to signal frequency (ω_s) and ω_1 can be idler frequency (ω_i) in Optical Parametric Amplification and Λ is the poling period of the crystal.

Optical parametric gain is a function of $\cosh^2$ for the phase-matched condition ($\Delta k = 0$) under the undepleted-pump approximation, as shown in Figure 4.10. In fact from second order nonlinear interaction term, Equation 4.4, in Maxwell's wave equation solution in frequency domain, under the slowly varying amplitude approximation, weak nonlinear interaction, if ($\Delta k = 0$), optical parametric gain has a function of $\cosh^2$ [82].

$$G = \cosh^2(\Gamma L) \tag{4.12}$$

Where G is parametric gain coefficient and the definition for Γ comes from

$$\Gamma^2 = \left(\frac{{d_{\text{eff}}}^2}{n^3}\right)\frac{2\,\omega_1\omega_2 I_{\text{pump}}}{\varepsilon_0 c^3} \tag{4.13}$$

Where d_{eff} is a nonlinear coefficient (pm/V) and I_{pump} is pump intensity or power density (W/cm^2).

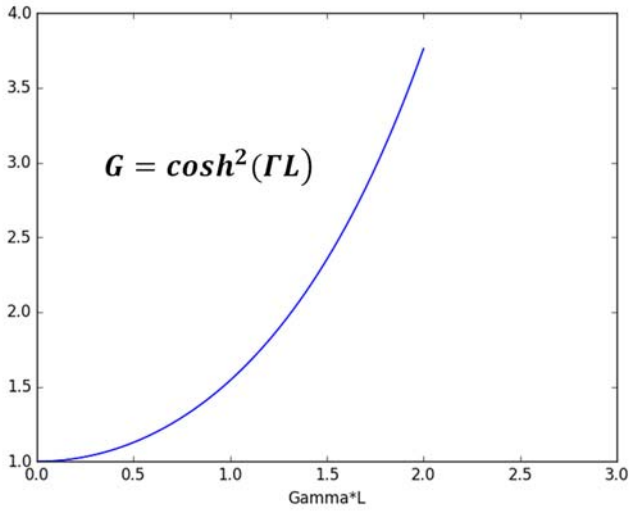

Figure 4.10: Optical Parametric Gain coefficient under a weak nonlinear interaction

Table 4.2 list some OPAs that can generate 1532 nm and may be used in an acetylene-filled HOFGLAS system. In our homebuilt OPA, we used a 5 cm long magnesium oxide periodically poled lithium niobate crystal (MgO:PPLN). Quasi-phase matching happens inside this crystal between nanosecond 1064 nm Nd:YAG laser with ~ 200 μJ pulse energy and continuous wave 1532 nm laser with ~ 70 mW power. Figure 4.11 shows the signal wavelength versus MgO:PPLN temperature for four poling periods. At a temperature of 105 centigrade degree and with the first poling period of the crystal (Λ=30 μm), the OPA produces 1532 nm pulses with about 23 μJ and almost 21 μJ of it is the measured maximum pulse energy at the surface of the HOFGLAS fiber

(after it passes through several optics). Using an appropriate long pass filter we can filter out the mid-IR idler and Nd:YAG pulses after the PPLN crystal. The homebuilt OPA has been described in detail in the next section.

Table 4.2: List of some OPAs that generate 1532 nm [83, 84]

Nonlinear Optical Crystal	Pump (μm)	Tunability range (μm)	Regime	Ref.
PPLN	1.064	1.25-5.4	cw	Breunig, Appl. Phys. B 105,99 (2011)
PPLN	1.064	1.36-4.83	ns	Meyers, Opt. Lett. 21, 591 (1996)

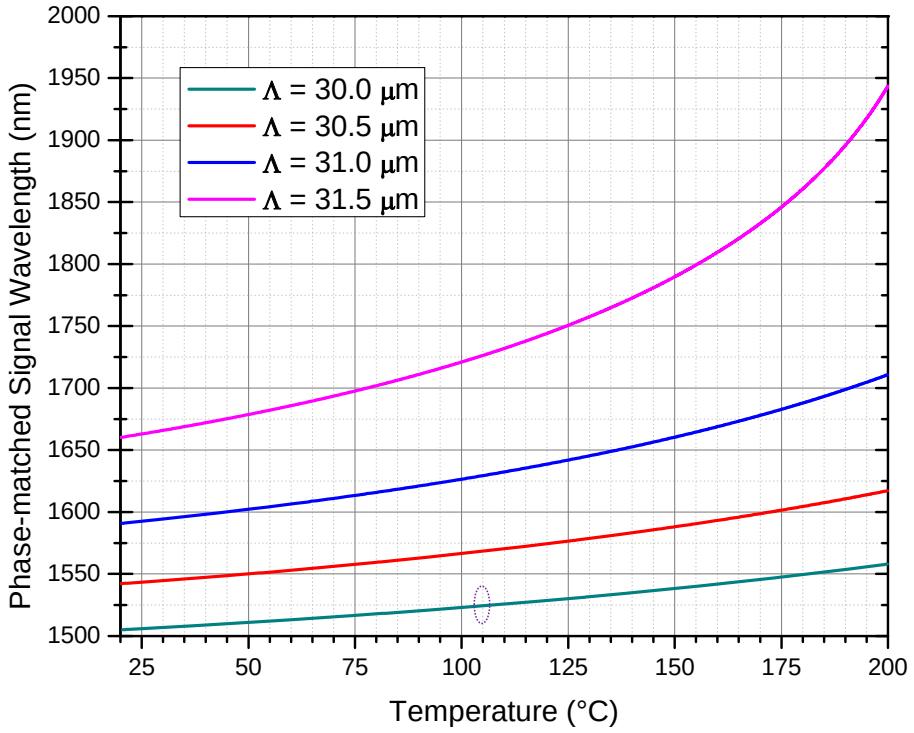

Figure 4.11: Phased-matched signal wavelength versus MgO:PPLN crystal temperature, reproduced from Ref. [74].

4.3.2. Optical Parametric Amplification

The OPA has three main elements which are a high-power pump laser, a seed laser which can be low power, and a nonlinear crystal satisfying the quasi-phase matching condition as shown in Figure 4.12.

We use a Diode-pumped single mode passively Q-switched Nd:YAG laser at 1064 nm (Crylas FTSS 355-50, Serial#: 13978C1030-08110) to pump our home-built OPA. The Q value (or quality factor) quantifies the ability of a laser to store input light photon energy in laser cavity. Q-switching is a technique of increasing Q value to generate energetic pulsed light from (~ 0.1 ns to a few hundred ns).

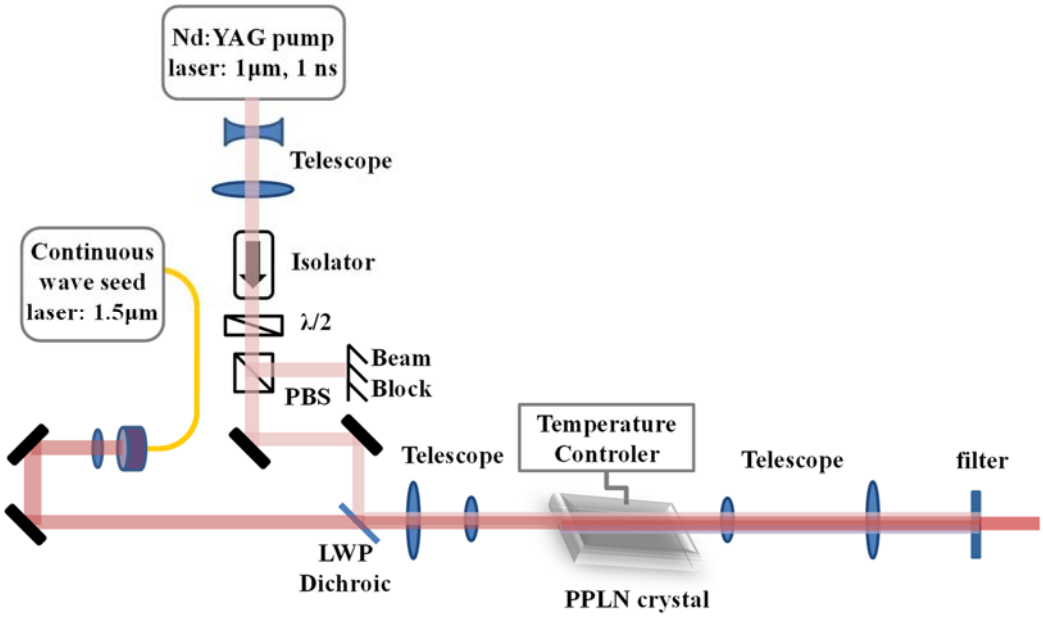

Figure 4.12: OPA setup that may produce 1532 nm pulses at 105 centigrade degree of the crystal's temperature and the pulses can be used to pump in acetylene-filled HOFGLAS.

There are several methods for Q-switching but our Nd:YAG is a passively Q-switched laser. This method uses saturable dyes inside the laser cavity medium and the losses are

automatically modulated with saturable dyes. The Dye material has its own energy levels matching those of the laser medium. Electrons of the lasing medium are pumped to higher energy levels. The dye atoms are excited to the same energy level and stay there for a short duration. During this short interval of time, photons emitted by de-excitation of laser medium atoms are not absorbed by the dye and exit the laser cavity. When the dye is in the ground state, it strongly absorbs the photons so no laser output is obtained. Thus, the Q value of the laser cavity is high or low depending on the state of dye atoms.

4.3.2(a). Seed Spectrum

We seed our OPA with a narrow linewidth, continuous wave extended-cavity tunable diode laser (Orbits Lightwave, model: ETH-25-1532.83-2-PZ10-T). The seed laser has a single-mode operation at the wavelength of 1532 nm. We use a commercial Optical Spectrum Analyzer (OSA) to measure the spectrum of the seed laser, as shown in Figure 4.13. The maximum output power of the seed laser is 20 mW.

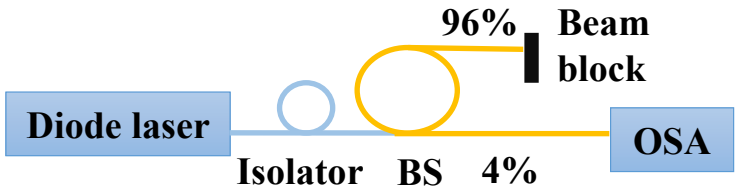

Figure 4.13: Setup to measure the spectrum of the seed laser. An isolator has been used to protect the seed laser from any light reflection. A beam splitter sends only a small fraction of light to the OSA to work bellow the damage threshold of the OSA.

The measured spectrum of the seed laser by the OSA is shown in Figure 4.14. The central wavelength is ~1532 nm as expected. The minimum resolution of the OSA is about 0.05 nm.

SNLO is a free software from AS-Phtonics designed to simulate nonlinear mixing processes. Based on SNLO calculations, if we increase the power of the seed laser, the amplified energy of the signal from the OPA will increase without reaching the damage threshold of our PPLN crystal.

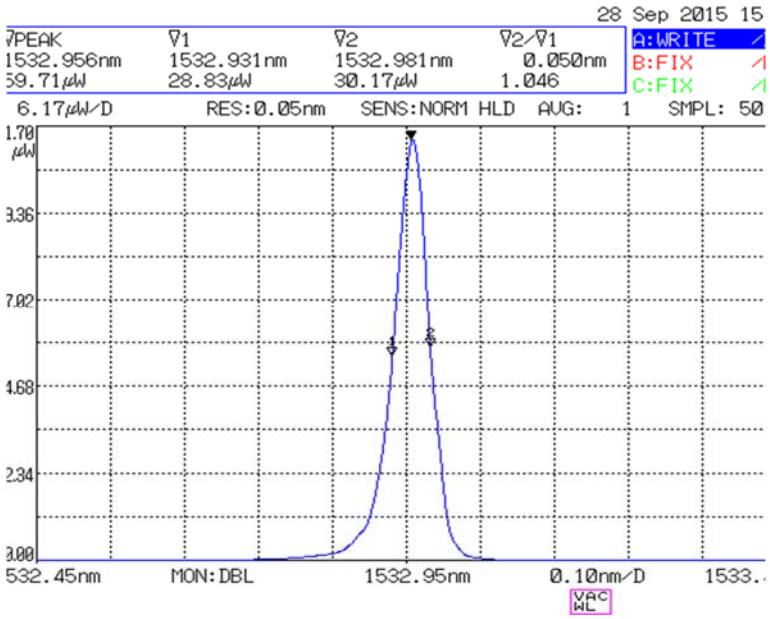

Figure 4.14: Measured spectrum of the cw extended-cavity tunable diode laser.

To increase the output power of our OPA, we incorporated an IPG-Photonics Erbium Doped Fiber Amplifier (model number: EAR-0.5-C-LP) with a maximum power of 500 mW, as shown in Figure 4.15. We have to run the laser below 300 mW to work below damage threshold of the isolator after the EDFA, which protects the EDFA from back reflections. Unfortunately, there was significant loss at the connection of the EDFA output fiber with the isolator because of damaged SNLO is a free software from AS-Photonics designed to simulate nonlinear mixing processes (PM) fiber ends. This resulted in a maximum cw power input to the OPA to be 50 mW.

The setup is ultimately fiber coupled. A beam splitter has been used after the combination of an isolator and diode laser to prevent from exceeding the maximum input power to the EDFA. Since the input fiber of the EDFA is Polarization Maintaining fiber, a fiber coupled polarization controller has been used as well. The zoomed in version and zoomed out versions of the measured spectrum after the EDFA using the above setup have been shown in Figure 4.16.

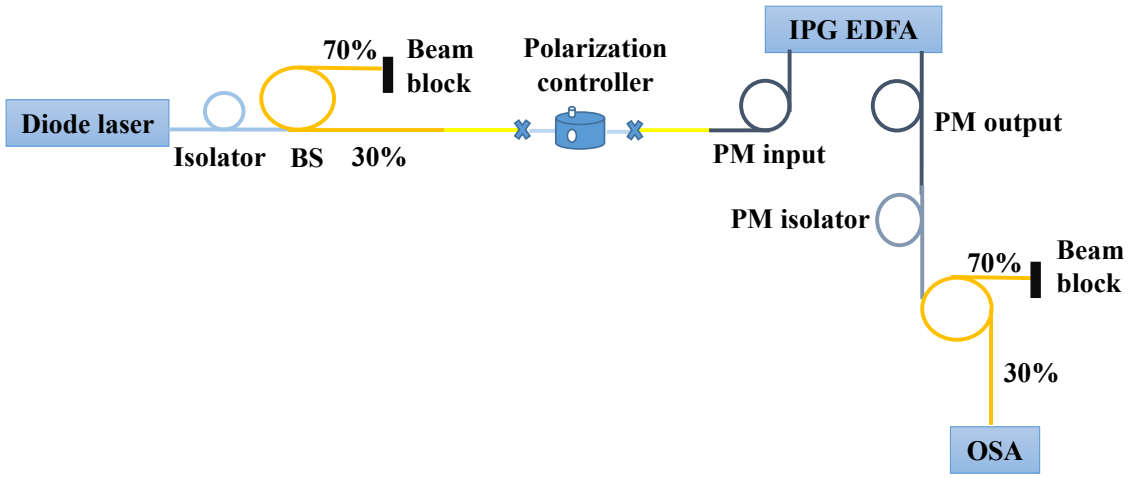

Figure 4.15: Schematic of the setup for measuring EDFA spectrum. BS: beam splitter, PM fiber: Panda Mode fiber.

From Figure 4.16 (b) it is obvious that some power is not at the peak wavelength but since the vast majority of the power is at the peak wavelength, we can use this setup to seed our OPA.

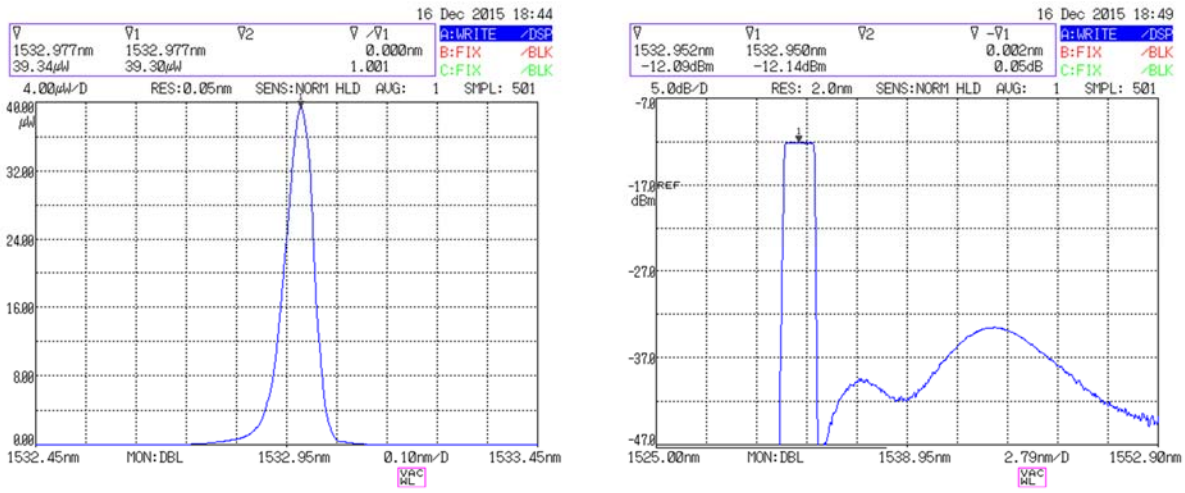

Figure 4.16: (a) Zoomed in version of the measured EDFA spectrum (b) Zoomed out version the measured EDFA spectrum.

4.3.2(b).Optimizing OPA output's wavelength

The MgO:PPLN crystal temperature is fixed at a temperature of 105 centigrade degree. The generated nanosecond amplified signal from OPA has ~ 23 μJ pulse energy that is measured with a Ophir photonics power meter. We then look at the output spectrum of the OPA. This is done by coupling the OPA output into a free-space monochromator and measure the spectrum. But, there is a faster way to check the wavelength, as shown in Figure 4.17. We couple the OPA into a Single Mode Fiber (SMF) and then couple this into a broad bandwidth (~1 GHz) Fiber Bragg Grating (FBG) at 1532 nm. The transmission port of the FBG is fiber-coupled into a 25GHz PD and the nanosecond pulses at 1532 nm can be detected by a fast 4GHz Oscilloscope from Tektronix. If the OPA has no spectral component at 1532 nm then the transmission through the FBG will be zero. We can then optimize the observed transmission signal through the FBG on an oscilloscope by tuning the crystal temperature around 105 centigrade or tuning the poling period around 30 μm (first Λ of the MgO:PPLN) and keeping track of the reflection and transmission ports of the FBG. Figure 4.17 shows how we use the same 25 GHz PD to look at both reflection

and transmission from a FBG on different channels of the fast scope using a beam splitter and creating time delay between the two sets of pulses. We used appropriate length of single mode fiber in the reflection port to create time delay.

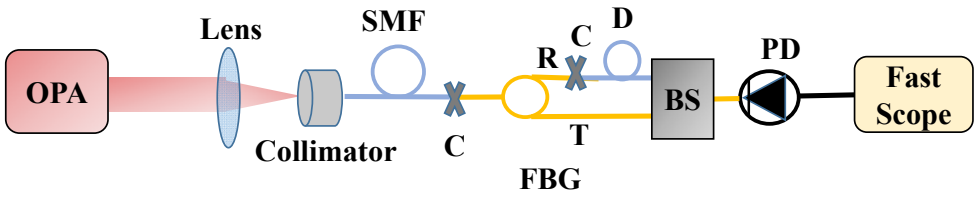

Figure 4.17: Schematic of the set up to optimize OPA output at 1532 nm. SMF: Single Mode Fiber, R: reflection port, T: Transmission port, C: connector, D: Delay fiber stage, BS: Beam splitter, PD: 25 GHz photodetector.

4.3.2(c).OPA pulse duration

To measure the exact pulse duration of the 1532 nm signal from the OPA, we coupled the beam into the 25 GHz IR photodetector (New Focus, model: 1414) and recorded the data for a single shot using a fast oscilloscope, as shown in Figure 4.18.

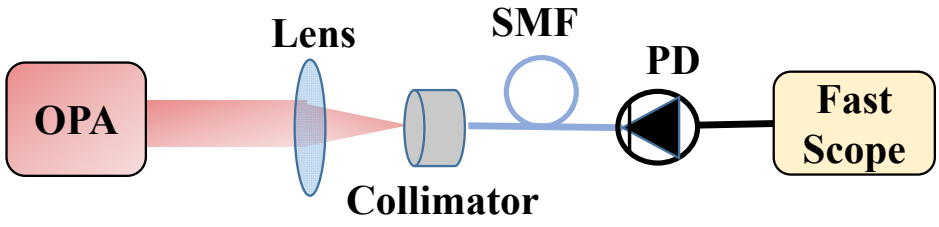

Figure 4.18: Setup for measuring pulse duration of OPA output.

The OPA pulse duration was measured to be ~ 1 ns, as shown in Figure 4.19. Data is recorded using a New Focus 25 GHz photodetector and a 4 GHz scope (Tektronix, CSA7404). Using the time bandwidth product for a Gaussian beam ($\Delta\nu \times \Delta t \sim 0.44$), the minimum bandwidth of the OPA is calculated to be ~ 440 MHz. In the section 5.1.1., the minimum bandwidth of the OPA will be compared to the calculated absorption bandwidth of the Acetylene at the desired fiber length and pressure.

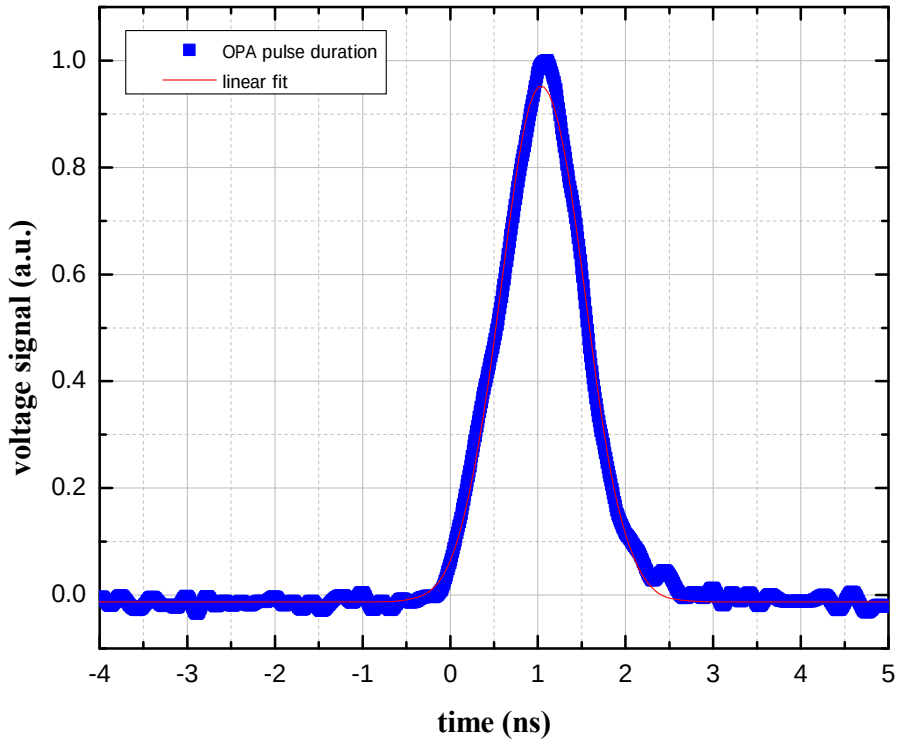

Figure 4.19: Measured pulse duration of OPA output.

4.3.3.OPA alignment improvement

The OPA was used for a couple months with several hollow-core optical fibers. In all of these attempts, the coupling into hollow-core fiber was power dependent, a typical data set for OPA pulse energies before and after a hollow-core fiber is shown in Figure 4.20. We double-

checked the coupling into hollow-core fiber by backward coupling and overlapping the input and output beams. Multiple apertures were used along the optical set up to ensure the beam passed through the center of all optics. The focal length of the lens was matched with the numeric aperture of the fiber. We began suspecting the mode quality of the OPA since these efforts did not pay off. Cameras that work well at low repetition rate and low energy costs more than 80k. So, I tried spatial filtering the OPA mode with pinholes at the focus of the telescopes before and after the PPLN crystal in Figure 4.12. Unfortunately, the pinholes burned at the OPA's maximum power.

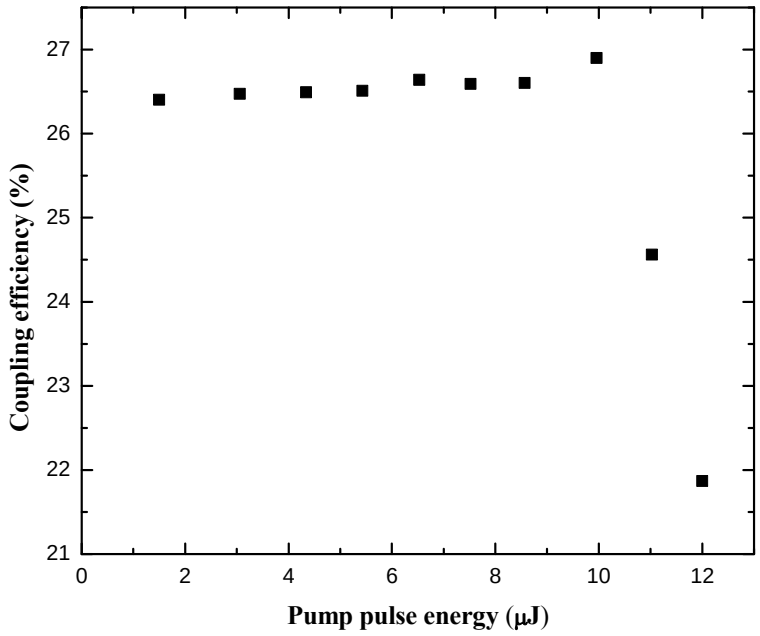

Figure 4.20: Coupling efficiency into HC-PCF as a function of input pump pulse energy.

At this point, I decided to rebuild the OPA from scratch. The crystal was removed from the setup to allow for proper adjustment of the YAG and seed laser. In particular, they must have roughly the same beam sizes and be spatially overlapped for a couple meters on the optical table.

Then I replaced the optics and the crystal and realigned the set up. The telescope before the crystal was made for compactness and consists of a +150mm focal length concave lens and a -50 mm biconcave. I replaced the -50 mm biconcave lens with a +50 mm concave lens to improve the beam overlap within the 5 cm PPLN crystal. An Ophir energy meter and FBG setup (explained in section 4.3.2(b)) were used to optimize the power and wavelength at 1532 nm, respectively. I also kept track of the beam shape on an IR card while optimizing the OPA alignment. Afterward, the OPA output was coupled into the hollow-core fiber. This eliminated the power dependent Coupling efficiency into HC-PCF, as shown in Figure 4.21. I concluded that this was mainly a result of improving the beam quality of the OPA.

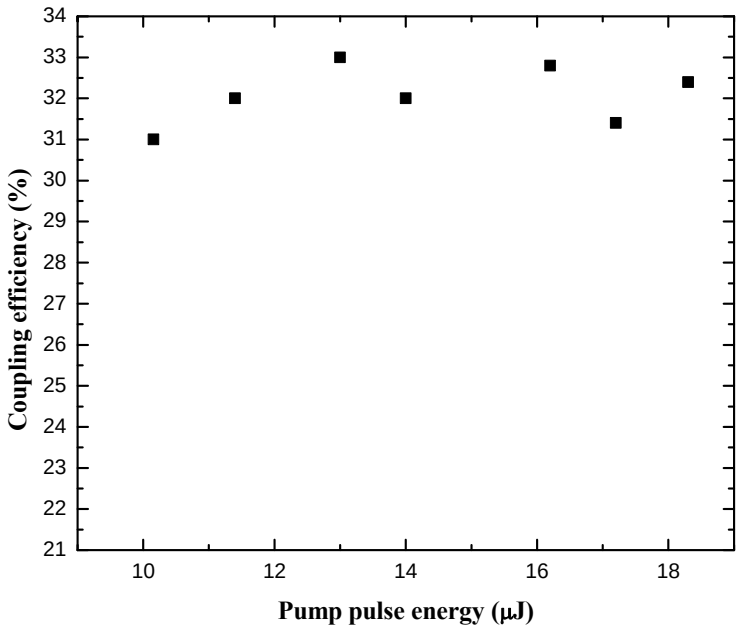

Figure 4.21: Coupling efficiency as a function of pump pulse energy after improvements of OPA alignment.

We block the ND:YAG pump and idler with the appropriate filters and send the amplified signal and cw seed laser, both at 1532 nm, into the HOFGLAS set up. We perform knife edge

measurements of both of the signal and seed to determine their beam profiles. The Gaussian beam is narrowest at the waist ($z = z_{waist}$) and away from the waist, the beam spreads with a hyperbolic outline. To determine the spot size as at each distance (z), knife edge measurement can be performed. These measurements are shown in Figure 4.22 and Figure 4.23 for the horizontal direction. In performing the horizontal knife-edge measurement, transmitted voltage signal was recorded after a razor blade at each transverse position as the razor blade is scanned across the beam using a translation stage from Newport Company. The spatial Gaussian intensity profile has a $\frac{1}{e^2}$ beam waist (ω). The transmitted power is related to the total power using Equation 4.14, where x is the transverse position defined by translational stage's micrometer, P_{tot} corresponds to maximum power, and x_0 is related to the initial micrometer position:

$$P(x) = \frac{1}{2} P_{tot} \left[1 + Erf\left(\frac{x - x_0}{\omega}\right)\right] \tag{4.14}$$

The error function, Erf, is defined as

$$Erf(x) = \frac{2}{\sqrt{\pi}} \int_0^x e^{-x'^2} dx' \tag{4.15}$$

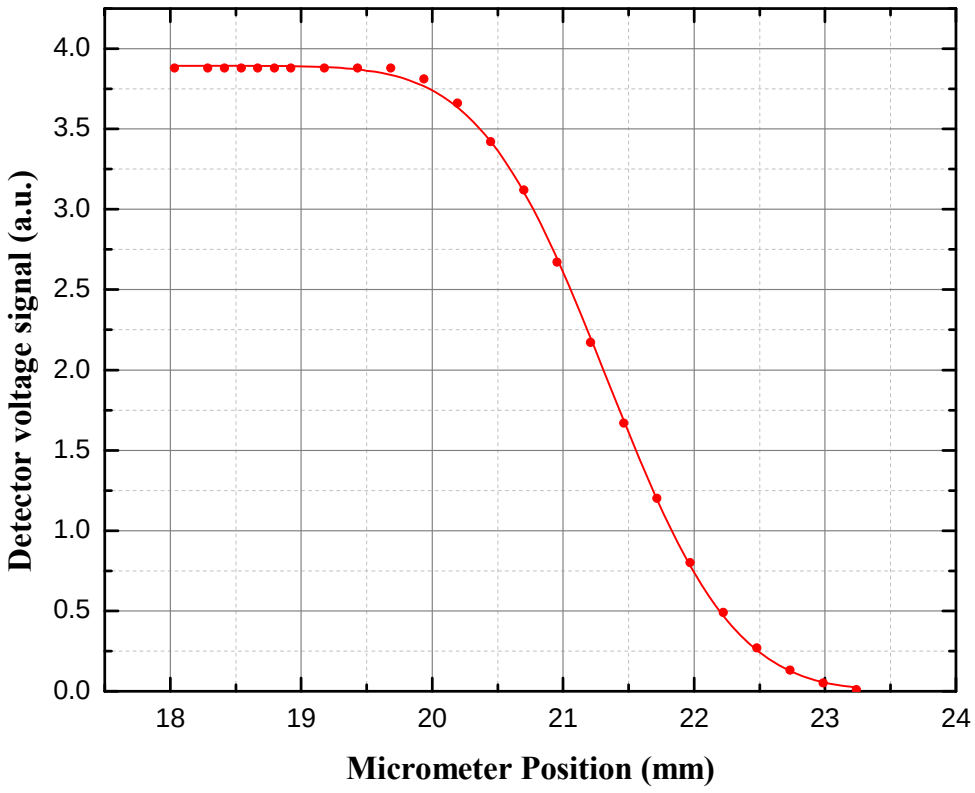

Figure 4.22: Horizontal Knife edge measurement for the seed laser before HC-PCF. Beam size is ~ 3mm and center of the beam is at 21.34 mm micrometer position. Vertical knife edge measurement is in agreement with these results.

Based on our knife-edge measurements, the center of the seed laser and signal are well overlapped and their beam sizes are different. The beam size of the signal is 6.8 mm, more than twice the size of the seed laser, which is 3 mm. This changes our choice of focusing lens for coupling into the HC-PCF. The selected focusing lens provides a perfect match between the input OPA beam size and the numeric aperture of the fiber.

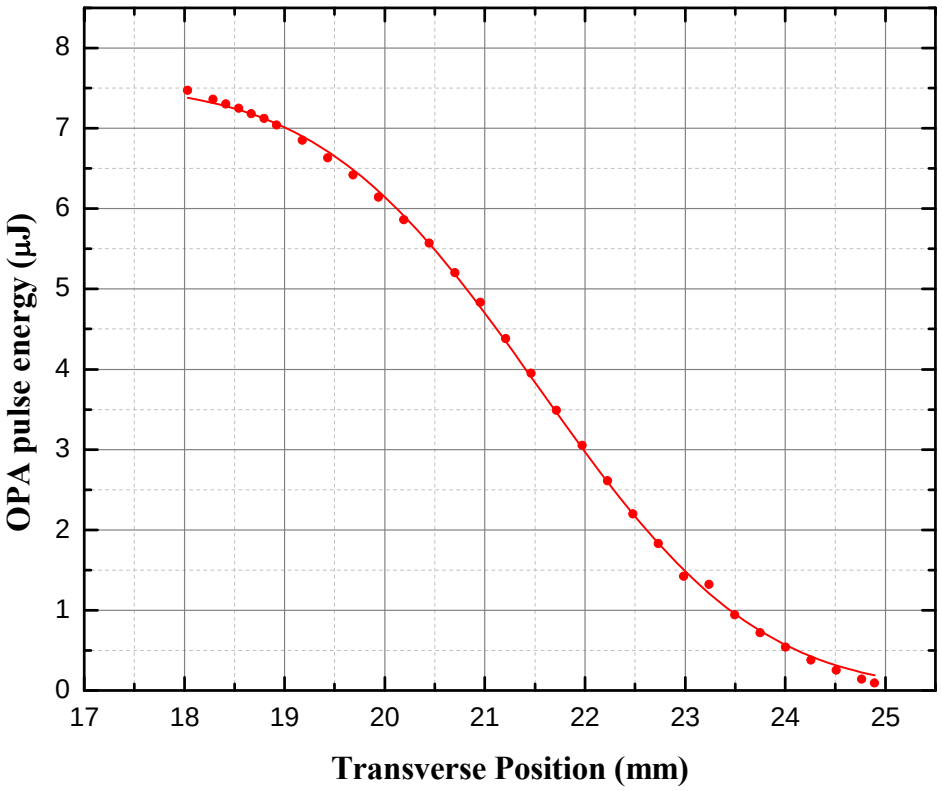

Figure 4.23: Horizontal Knife edge measurement for the OPA output beam at 1532 nm before HC-PCF. Beam size is ~ 6.8 mm and center of the beam is at 21.54 mm micrometer position.

4.4. Energy level diagram and spectrum

Acetylene is a linear molecule with seven normal modes with two of them being doubly degenerate, as shown in Figure 4.24. Among these modes are a vibrational C-H symmetric stretch mode (ν_1) and a vibrational C-H antisymmetric stretch mode (ν_2). Their frequencies are shown in Table 4.3 in terms of cm^{-1} and Hz. One cm^{-1} is equal to 2.99793×10^{10} Hz. So, I can convert frequencies corresponding to the modes of our interest ν_1 and ν_3 to Hertz and put them in the third column of Table 4.3.

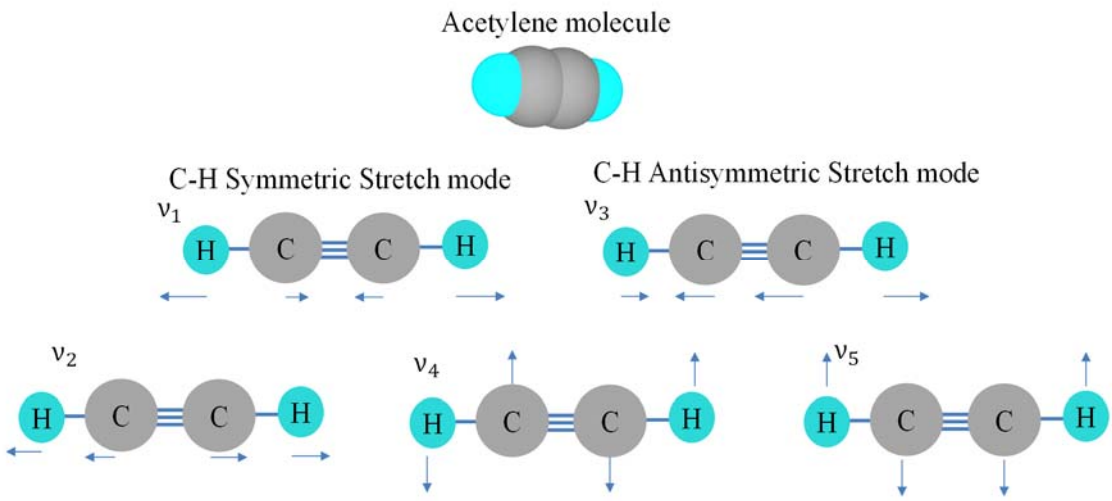

Figure 4.24: Acetylene molecule and its normal modes. ν_1 is the C-H symmetric stretch mode and ν_3 is the C-H antisymmetric stretch mode. The relative motions of the atoms in the acetylene molecule are shown with small arrows under the atoms.

An Acetylene molecule occupying a particular molecular vibrational and rotational state may absorb (emit) light to excite (decay) into other states. Fundamental molecular vibrational transitions can happen when the selection rules ($\Delta v_i = \pm 1$) are satisfied, this is similar to the simple harmonic oscillator problem. However, molecules do not behave exactly as independent simple harmonic oscillators as weak additional transitions, called overtones, are allowed. We are interested in the Transition from ground vibrational state to the overtone vibrational state of ν_1+ ν_3, referred to as P(13).

Table 4.3: Frequencies related to the vibrational normal modes of interest of Acetylene molecule [85, 86].

Vibrational normal mode	Frequency in $^{12}C_2H_2$ (cm^{-1})	Frequency in $^{12}C_2H_2$ (Hz)
ν_1	3397.12	101.84×10^{12}
ν_3	3316.86	99.44×10^{12}

The seed diode laser for the OPA allows tunability of the pump wavelength on and off resonance with the P(13) transition of acetylene at 1.53 μm. The seed laser for the OPA is tuned on resonance with the P(13) transition line. This results in laser emission along the P(13) and R(11) transitions, as shown in Figure 4.25. The P branch is related to transitions between rotational levels with $\Delta J = -1$ while the R branch is related to rotational transitions with $\Delta J = +1$. The Q branch is related to $\Delta J = 0$ which can only happen if the vibrational angular momentum of either the initial or final levels is non-zero in order to conserve total angular momentum. This is not the case for us, so we observe no lasing in the Q branch. The R branch (left side) and P branch (right side) absorption spectrum of acetylene molecules, borrowed from NIST, are shown in Figure 4.26. The measurements are from a 5 cm long gas cell at a pressure of 50 torr. The two lasing transitions that lead to emission around 3 μm are shown in the inset of Figure 4.25.

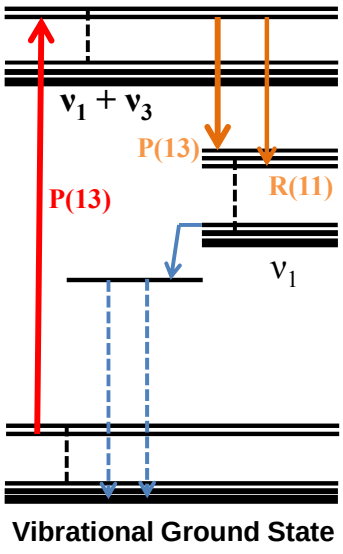

Figure 4.25: Rotational-vibrational energy levels related to C-H symmetric stretch mode ν_1 and a C-H antisymmetric stretch mode ν_2.

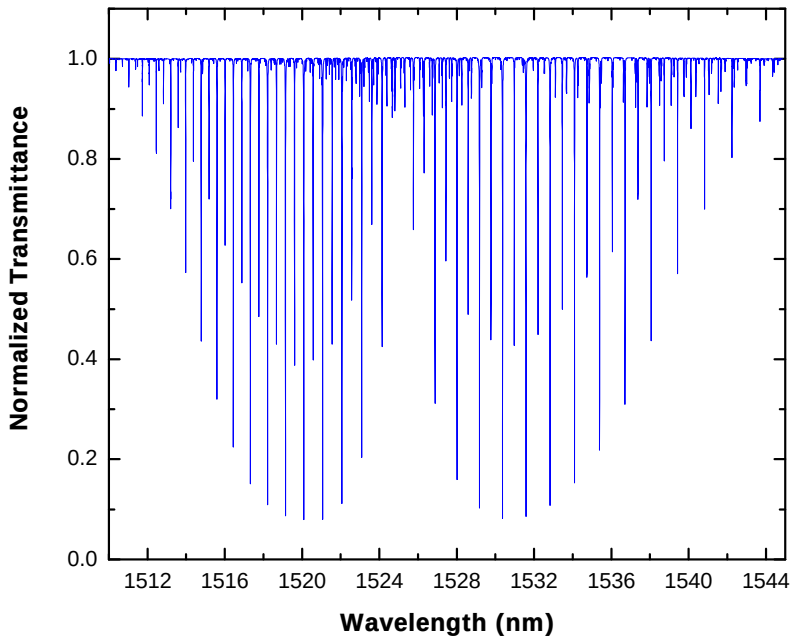

Figure 4.26: Data from NIST measurements for a 5 cm gas cell at 50 torr acetylene pressure. The R branch (left side) and P branch (right side).

The spectrum for our laser is shown in Figure 4.27 at the highest pump pulse energy as we tune the seed on resonance with 1532 nm.

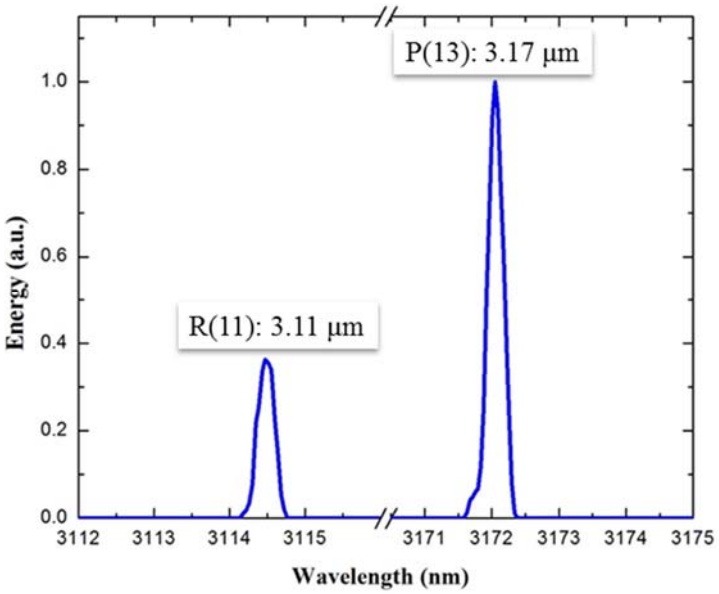

Figure 4.27: Spectrum of the OPA-pumped Acetylene-filled HOFGLAS at the highest laser pulse energy. It is consistent with the data presented in chapter 5.

The R(11) laser line is at 3.11 μm and the P (13) lasing line is associated with the 3.17 μm wavelengths. Since P(13) is related to longer wavelengths, we assumed it must have lower energy than the R(11) lasing line. However, the observed spectrum does not agree with this assumption. The reason could be different polarizations of the lasing lines that affected the spectral measurment on using a polarization dependent monochromator.

4.5. Maximum theoretical efficiency calculation

The maximum theoretical efficiency is 33% and it comes from simultaneous saturation for pump and lasing transitions. A steady state condition for the laser energy levels can be assumed to prove the maximum theoretical efficiency, as shown in Figure 4.28.

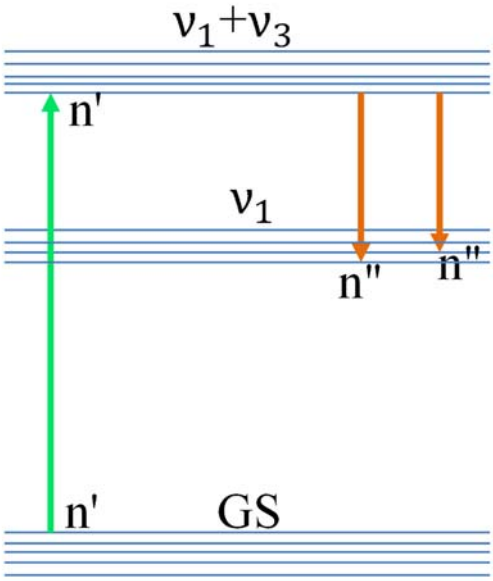

Figure 4.28: Steady state condition for simultaneous saturation of pump and lasing transitions. n' is the number of molecules in the Ground State (GS) and also rotational-vibrational overtone state symmetric and antisymmetric stretch of C-H mode while pump transition is saturated and n" is the number of molecules in the destination energy level for R(11) and also P(13) lasing transition lines while these lasing transitions are saturated.

In the steady state condition while pump transition is saturated, n' is the number of molecules in the ground state and it is equal to number of molecules in the excited state. n'' is the number of molecules in the destination energy level for R(11) and also P(13) lasing transition lines while these lasing transitions are saturated. When the pump and lasing lines are saturated simultaneously, n' must be equal to n''. In this case, the number of absorbed photons equals to $3n'$E where E is the pump energy and number of lased photons equals 3 $n''E'$ where E' is the laser energy and E' equals to half of the pump energy. So, slope efficiency can be calculated as shown in Equation 4.17 and it results in 33% maximum theoretical efficiency.

$$\frac{E_{out}}{E_{in}} = \frac{2\,n'\frac{E_{pump}}{2}}{3n'E_{pump}} = \frac{1}{3} \tag{4.16}$$

4.6. Detection system

As shown in the simplified version of the laser setup in Figure 4.29, we can measure the pump pulse energy before the HC-PCF and both the mid-IR and residual pump pulse energies after the HC-PCF. We measure the mid-IR laser pulse energy using a Germanium filter inserted perpendicular to the beam path.

Figure 4.29: Simplified version of the setup of pump coupling into HC-PCF and measuring pump pulse energy as well as residual pump and mid-IR laser pulse energies.

Andrew Jones used the voltage signal of a photodetector to compute pulse energy. In this method, he measured the integrated pump voltage signals before and after the fiber as well as the signal after the Ge filter all in units of (V×ps). The voltage signal is recorded by a LabVIEW-controlled oscilloscope and the calculation of the area is done in MATLAB. The code is in Appendix E of his PhD dissertation [74]. He used a "Coherent" Pyroelecteric energy meter to calibrate the integrated voltage signal and convert it to pulse energy. He was using the pyroelectric energy meter at A & B & C, shown in Figure 4.29, for both on and off resonance laser operations at each pump pulse energy. The measurements are usually done at seven pump pulse energies. The pump pulse energy incident on the fiber can be controlled with variable attenuators after the OPA. The calibration factor in terms of $\frac{nJ}{V \times ps}$ is determined by applying a linear regression on the data and finding the slope. Although his method of calculating calibration factors is performed with upmost accuracy, the 3 μm pulse energy versus absorbed pump pulse energy usually appeared noisy [74].

We went through a sequence of measurements to check linearity in response of the HgCdTe Photo Detector as well as energy meter linearity check at low energies. Finally, we noticed energy meter is noise sensitive and we may reduce this effect by using a rubber sheet under the power meter holder where it is in contact with optical table. But still at low energies the noise level was of the same order as the detected signal. So, we switched our energy meters to newer energy meters from Ophir that work better at lower pulse energies. We also used the external triggering to trigger the energy meters and this was helpful as well. By applying these corrections and measuring pulse energies directly at A & B &C in Figure 4.29 and taking data in relatively quiet lab, the amount of fluctuations on the produced 3 μm pulse energy was reduced and more stable laser system was obtained.

4.7. Calculating absorption by the gas

As shown in Figure 4.29, We measure input pump pulse energy at “A”, mid-IR laser pulse energy at “B” and combination of any residual pump and produced mid-IR laser pulse energy at “C”. Then, corrections must be applied for propagation through several optical components, coupling efficiency into the HC-PCF and fiber loss at pump wavelength to be able to reach the accurate measured pulse energies at the surface of fiber. We must account for the losses between measurement point “A” and the entrance of the fiber to know the exact pulse energy entering the fiber. A correction factor of 0.99 was applied for the transmission through a silver flat mirror, a BK7 plano-convex lens, and a BK7 window (all from Thorlabs). On the right hand side of Figure 4.29, the measured mid-IR pulse energy at “B” is lower than the actual mid-IR pulse energy at the exit of the fiber by a factor of (0.9481× 0.8821), where 0.8821 stands for transmission through CaF_2 window and a CaF_2 collimating lens and 0.9481 stands for transmission through Germanium Filter perpendicular to the beam. Finally, the measured pulse energy at “C” should be divided by (0.8821×0.99), where 0.8821 stands for transmission through CaF_2 window and a CaF_2 collimating lens and 0.99 stands for transmission through a flipper silver flat mirror. All optics are from Thorlabs.

With the reflective and transmissive components accounted for, we turn our attention to the coupling efficiency into the hollow core fiber. On the right hand side of Figure 4.29, we assume 100% output coupling, meaning the measured pulse energies at the surface of the fiber is equal to the pulse just inside the fiber. At the entrance of the fiber, i.e. left hand side of Figure 4.29, there is loss of pump coupling into the HC-PCF. We may quantitatively find the coupling efficiency in addition to calculating the absorbed pump pulse energy only by gas.

The first step toward calculating absorption by only gas inside the fiber is in calculating pump coupling efficiency into HC-PCF. To do so, I used off resonance measurements for the residual pump at the exit port of the fiber (P_{out} in Figure 4.30) along with a pump ratio value calculated from the Equation 4.17.

$$\frac{P_{out}}{P_{in}} = e^{-\alpha L} \tag{4.17}$$

Where α is the absorption coefficient by fiber and L is the length of the fiber.

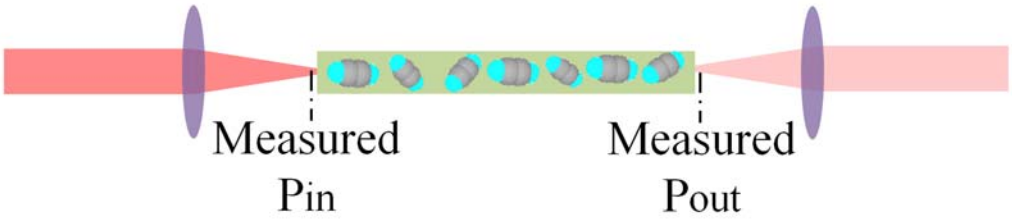

Figure 4.30: Gas-filled fiber. "Measured P_{in}" is the input pump measured value of the outside surface of the fiber after applying all the corrections of transmission through optics in the set up. "Measured P_{out}" is the measured residual pump at the exit port of the fiber after applying the corrections related to transmission through all optics in the set up.

We are provided with α in terms of dB/m. So, the Equation 4.17 is used for a certain length of fiber. The ratio of $\frac{P_{out}}{P_{in}}$ in terms of dB is used and the residual pump is measured at the exit port of fiber for off resonance case and it is divided by the calculated ratio of $\frac{P_{out}}{P_{in}}$ to find coupled input pump energy at the inner surface of entrance port of the fiber. The coupled input pump at the inner surface of the fiber can be divided by measured input pump at the outer surface of the fiber and the coupling efficiency can be obtained as shown in Equation 4.18.

$$\text{Coupled } P_{in} = \text{Coupling efficency} \times \text{Measured } P_{in} \tag{4.18}$$

Now, using the calculated coupling efficiency and on resonance data we can calculate the absorbed pump pulse energy only by gas as it has been summarized in Figure 4.31.

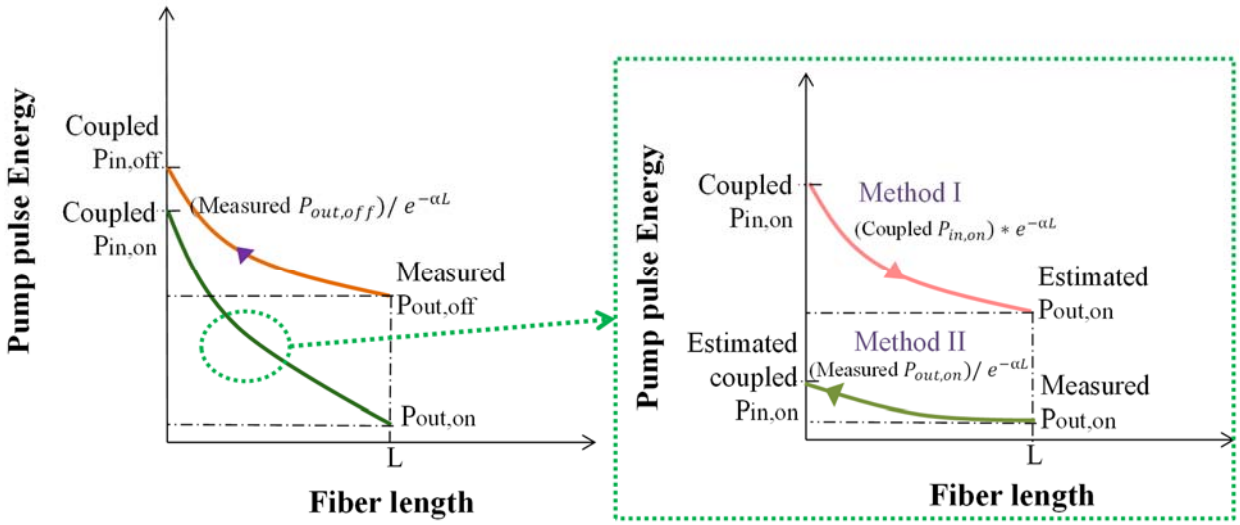

Figure 4.31: Summary of coupling efficiency calculation on the left side and absorption by gas calculation through averaging of method I and method II on the right side.

In order to do so, two methods have been used that are described in this section and Brian Washburn noticed that the result of the average of these two methods matches very well with solving a z dependent absorption differential equation and finding the absorption by gas. The two methods are summarized in Figure 4.31 for better clarification. Both methods use on resonance data to calculate power lost due to imperfect fiber guidance and then calculating the absorbed pump pulse energy by the gas is possible from Equation 4.19.

(4.19)

$$Absorbed\ power\ by\ gas = Coupled\ P_{in,on} - P_{out,on} - Power\ lost\ in\ fiber$$

Where "Coupled $P_{in,on}$" is the on resonance data for input power at the inside surface of the fiber, " $P_{out,on}$" is the residual pump power at the surface of the exit port of the fiber and "Power lost in fiber" is the calculated pump power lost due to imperfect fiber guidance from method I or method II. In method I, we use the coupling efficiency, found from off resonance data as explained above, to measure coupled input pump power for the on resonance case and then multiply it with the power ratio from Equation 4.17 to estimate residual pump power at the exit port of the fiber. Then we calculate "power lost in fiber" by subtracting "estimated $P_{out,on}$" from "Coupled $P_{in,on}$" and use Equation 4.19 to calculate absorbed power by gas. In method II, we take the "Measured $P_{out,on}$" data and move backward along the fiber length and divide this value by the power ratio from Equation 4.17 to find "estimated coupled $P_{in,on}$". Then we calculate "power lost in fiber" by subtracting "Measured $P_{out,on}$" from "estimated coupled $P_{in,on}$" and use Equation 4.19 to calculate absorbed power by gas.

The improvements described in chapter 4 were applied to the acetylene-filled HOFGLAS system and the experimental results for laser operation are presented and discussed in chapter 5.

Chapter 5 - Improved acetylene HOFGLAS operation results

The improvements on the pulsed acetylene-filled HOFGLAS system were discussed in chapter 4 in detail. In this chapter, the improved output pulse energy of the mid-IR pulsed acetylene HOFGLAS system is reported. Some of the applications of this laser system like remote sensing require high power. So, power scaling this laser system was investigated by optimizing the laser operation through maximizing the OPA alignment to improve its modal content, using longer length of fiber to increase the interaction length, and improving the beam quality of the mid-IR emissions. The highest pulse energy ever obtained in the 3 μm mid-IR region from the acetylene-filled HOFGLAS after applying the improvements is reported here, 1.4 μJ. Higher mid-IR pulse energies can be achieved by improving the pulse energy achievable from the OPA pump source and working with longer pulse duration to decrease the bandwidth of the OPA. This operation demonstrates many novel properties of the acetylene HOFGLAS. The excellent spatial beam quality at highest power and phenomenological scaling of saturation power and efficiency with pressure encourage for further power scaling, and motivate development of numerical models of the laser for deeper insight into these effects [87] . M^2 measurement method was used to examine spatial beam quality and it was found to be fiber-dependent [77], [25, 78]. For the improved setup, M^2 was investigated at several input pump powers in addition to the reproducibility checks [25, 78]. M^2 of 1.14 at the maximum output power motivates for beam combining to scale to higher power. The independence of efficiency on pressure is an evidence for reaching higher mid-IR power at a pressure where saturation behavior does not exist. achieving the highest mid-IR power to date, 1.14 μJ, encourages for building higher power OPA to produce high power mid-IR emissions. This laser exhibits novel behavior that motivates both numerical/theoretical investigation and further efforts to scale to higher powers.

5.1 Acetylene-filled HOFGLAS operation results

A 10.9 m negative curvature kagome HC-PCF is installed in the acetylene-filled HOFGLAS system. As it was discussed in chapter 3, the low loss of the kagome-structured HC-PCFs over broad bandwidths make them an appropriate choice for HOFGLAS systems that require a long interaction length. The core of these inhibited coupling kagome HC-PCF have a hypocycloidal shape with negative curvature. This enhances the coupling inhibition between the core and cladding modes [88-90]. The HC-PCF that is used in this experiment has an outer diameter of 360 µm and the hypocycloid inner core diameter varies between 60 µm and 72 µm, as shown in Figure 5.1.

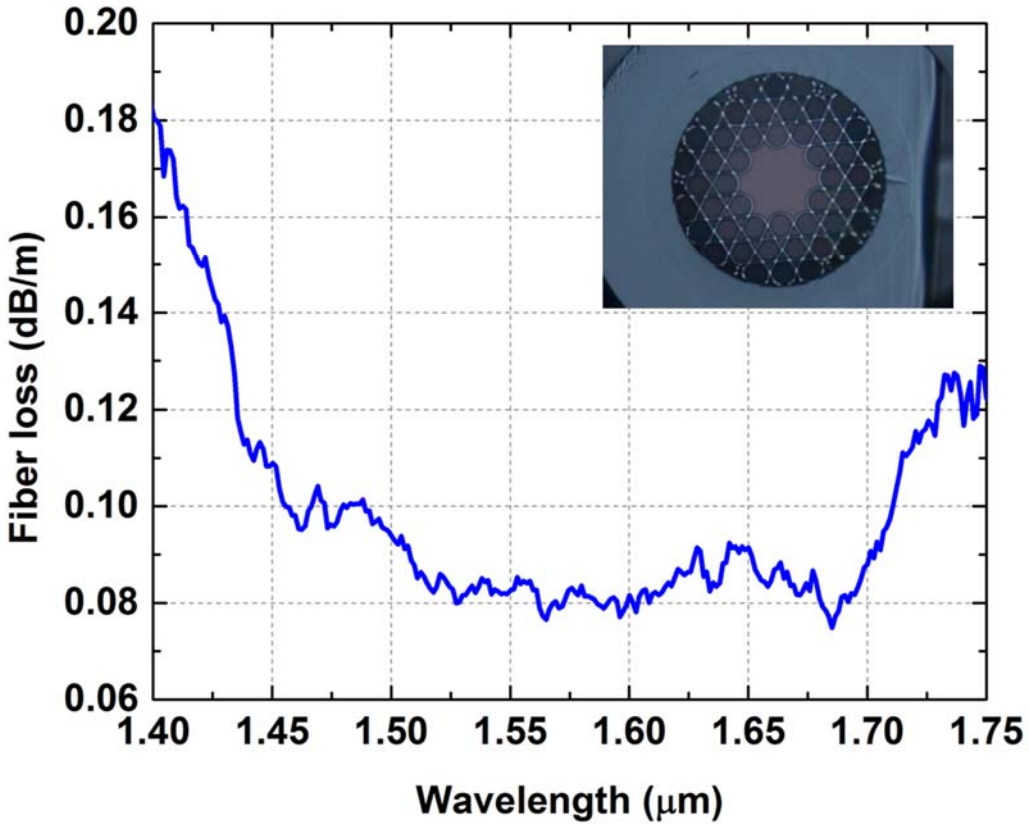

Figure 5.1:7 cell, 3 ring, hypocycloidal-core kagome fiber cross section and loss spectrum in near-IR, we are provided with data from Xlim research institute. 1.13±0.05 dB/m is the fiber loss at 3 µm and 0.08 dB/m is the fiber loss at the pump wavelength of 1.53 µm.

This is fiber #15 from Table 3.3 and we picked this because of the low loss at the pump and lasing wavelength. The fiber loss was measured to be 0.08 dB/m at the pump wavelength (1.53 μm) and 1.13±0.05 dB/m at the average lasing wavelength (3.1 μm). The loss at mid-IR was measured using the output of our acetylene HOFGLAS system. The measured loss is consistent with the empirical scaling laws for inhibited coupling into HC-PCF. Figure 5.2 shows the experimental setup of the acetylene-filled HOFGLAS, which is similar to Figure 4.1.

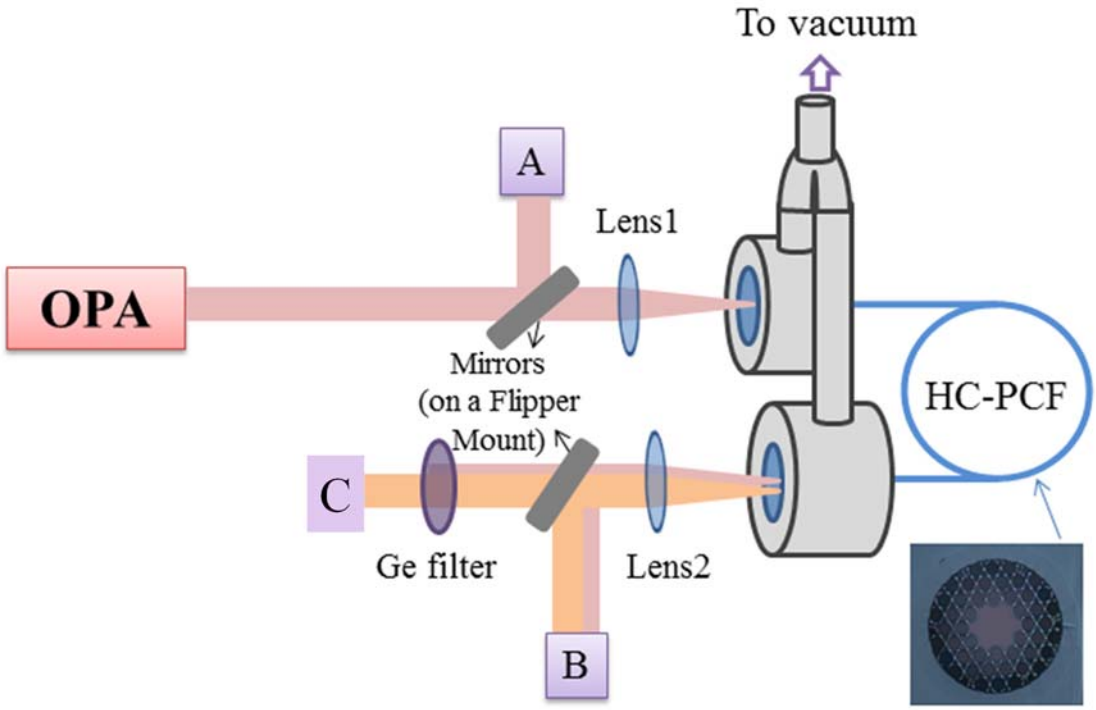

Figure 5.2: Experimental setup for pulsed operation of acetylene-filled HOFGLAS system.

A combination of half-wave plate and polarizing beam splitter are used as a variable attenuator to control the pump pulse energy. An anti-reflection (AR) coated BK7 lens with focal length 75 cm is used to couple the pump into the core of the HC-PCF. An AR coated BK7 window on one of the vacuum chambers was used to allow the pump pulses to be coupled into the HC-PCF

and a CaF_2 window on the other vacuum chamber allows both the pump and laser pulses to leave the vacuum chambers.

As discussed in section 4.3.3, improved modal content of the OPA output played an important role in achieving good energy coupling into the fiber. Average pump coupling efficiency is 52% after applying corrections for fiber loss at pump wavelength. The output beam is collimated with a CaF_2 lens (focal length 150 mm). A germanium filter is placed perpendicular to the beam at the output and it filters the residual pump and passes the produced mid-IR beam, enabling laser diagnostics. At several acetylene pressures, the performance of the laser is characterized in the fiber in terms of the produced mid-IR pulse energy and the results are discussed in the following sections. Also, the laser beam quality is investigated at various laser pulse energies.

5.1.1. Produced mid-IR pulse energy and laser efficiency

The OPA wavelength is tuned on resonance to the P(13) absorption line in acetylene, corresponding to the transition between the vibrational ground state and the $\nu_1+\nu_3$ rotational-vibrational excited state (1.53 μm), which is Doppler-broadened to ~475 MHz and additionally pressure-broadened by ~11 MHz/torr [91]. Appendix B gives the Python code for calculating the linewidth of the absorption feature at a given acetylene pressure and it shows the transmission feature for the given pressure and fiber length.

Population inversion between the rotational-vibrational states results in lasing at two mid-IR wavelengths (3.11 μm and 3.17 μm) which are related to the R(11) and P(13) lines in acetylene molecules. They correspond to the transitions between the $\nu_1+\nu_3$ rotational-vibrational excited state and the ν_1 vibrational state, as shown in Figure 4.25.

As discussed in section 4.6., using a more sensitive pyroelectric energy meter allows for better characterization of the laser. These energy meters are used to measure the 1.53 μm and 3

μm pulse energies at different positions in the laser configuration. As discussed in section 4.7., the germanium filter blocks the residual pump and makes the measurement of 3 μm laser pulse energies possible. It is possible to estimate the total pump pulse energy absorbed by gas experimentally. To do so, measurement of the input pump pulse energy before the vacuum chambers and the residual pump pulse energy after the vacuum chambers are needed in addition to careful consideration for coupling efficiency and fiber loss at pump wavelength. Figure 5.3, shows the 3 μm output pulse energy versus the pump pulse energy coupled into the fiber when a coupling lens of focal length f = 75 mm was used for several acetylene pressures. Saturation behavior is clearly observed below 9.8 torr.

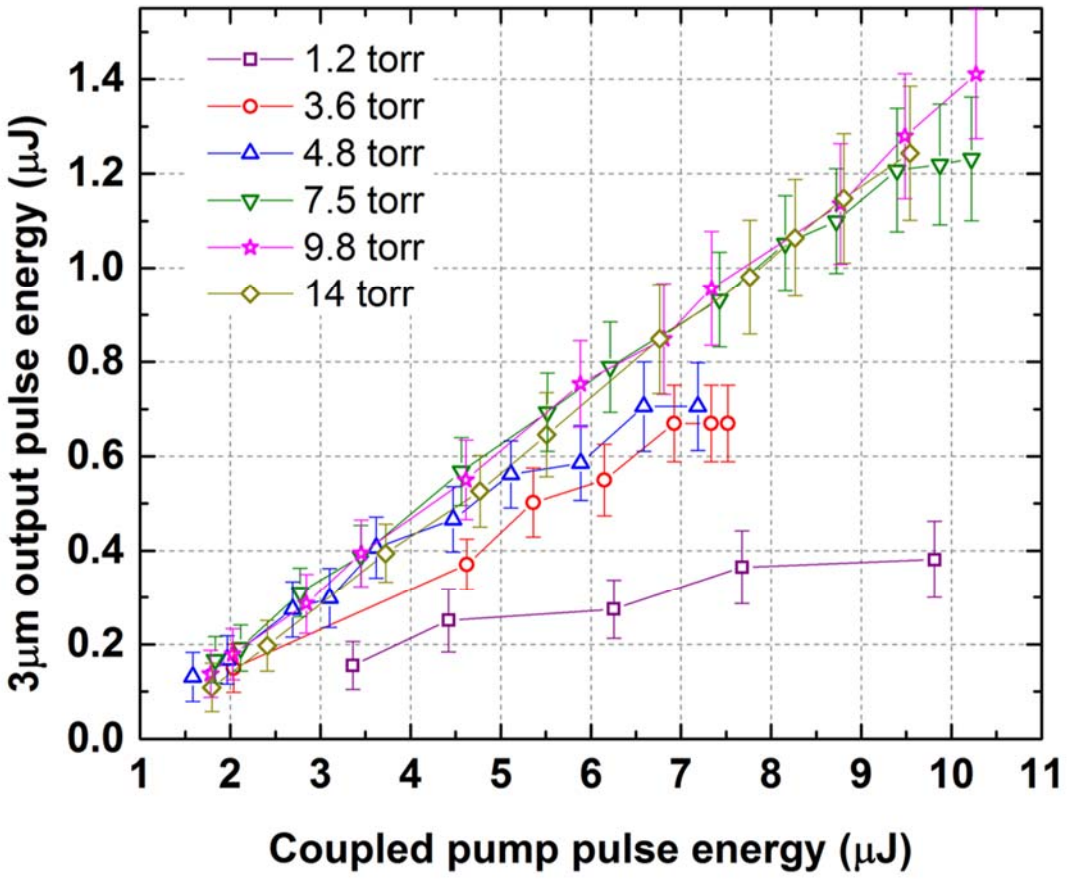

Figure 5.3: Plot of produced mid-IR pulse energy versus input pump pulse energy which is corrected for coupling efficiency of 52%.

By saturation behavior, I mean that as we increase the input pump pulse energy we observe no increase in produced laser pulse energy. We eliminated saturation behavior at most of the pressure ranges compared to our previous results. We believe this is due to the longer fiber, lower loss in the fiber itself, as well as improvements in the HOFGLAS setup discussed in section 4.3.3. Figure 5.4 shows the produced 3 μm pulse energy from the laser as a function of the total pump pulse energy absorbed by acetylene in the fiber. In similar plots from Andrew Jones' thesis [74], fiber loss was not taken into account for the absorbed pump energy. Therefore, his reports are for the total absorption by gas and lost due to imperfect fiber guidance. Figure 5.4 reflects our best understanding of those losses at this time.

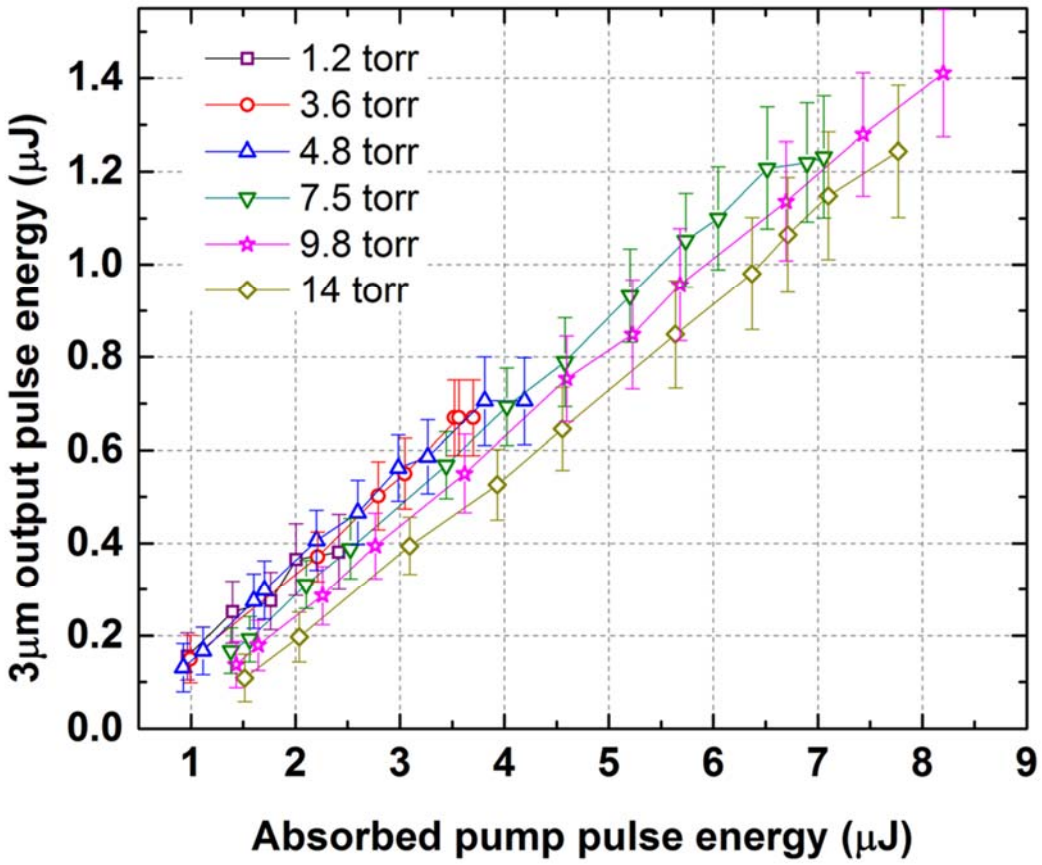

Figure 5.4: Plot of produced mid-IR pulse energy versus absorbed pump pulse energy only by gas which is corrected for fiber loss.

Figure 5.3 and Figure 5.4 show results of operation of acetylene-filled HOFGLAS for the range of pump pulse energies achievable from the current OPA, while 10.9 m of the HC-PCF is used. When acetylene is used at pressures above 9.8 torr, the laser operates without observing any saturation behavior, and produces a maximum 3 μm pulse energy of 1.41 μJ at 9.8 torr. At this highest output pulse energy the slope efficiency is ~ 17% and the overall efficiency with respect to the input pump pulse energy is ~ 14%. Figure 5.4 also illustrates that for pressures below 9.8 torr, the 3 μm output energy increases but eventually saturates as the absorbed pump pulse energy by the acetylene gas increases. The saturation points of mid-IR laser pulse energy are plotted against acetylene pressure in Figure 5.5. It clearly shows that the pump energy where saturation occurs increases as the acetylene pressure increases. This is a positive indicator for higher power operation. It is possible that this laser system is limited by the number of molecules available for excitation, which explains why the output energy scales with pressure. The linear fit in Figure 5.5 was extrapolated to higher fiber pressures. It suggests that the mid-IR laser may reach 2 μJ without saturation assuming we have a pump laser with sufficient energy. We expect this predicted power scaling at higher acetylene pressures if other factors, reduced transmission at pump and lasing wavelengths, pressure broadening, etc. do not limit the laser performance at the higher pump powers.

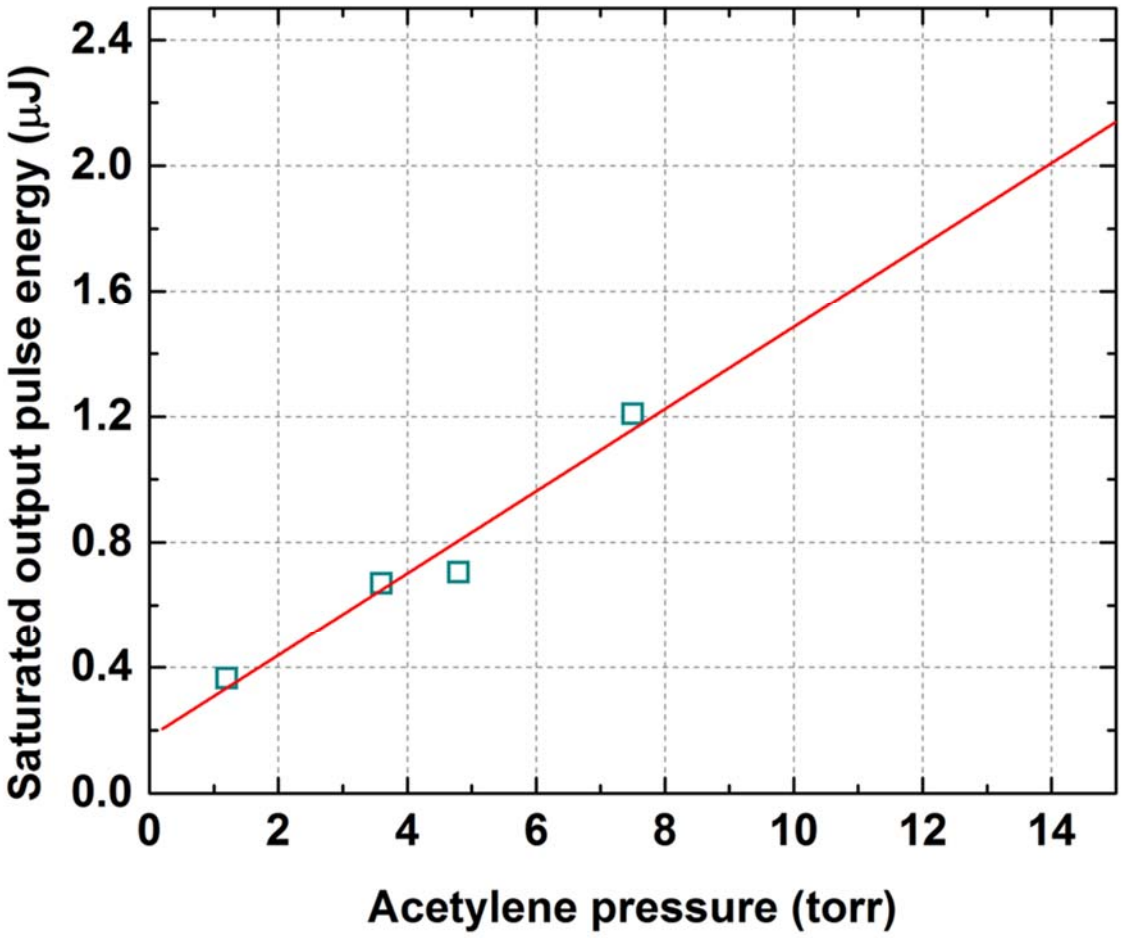

Figure 5.5: Observed saturation point versus acetylene pressure.

The slope efficiency of the laser is obtained by fitting the linear region of each curve in Figure 5.4. Then the slope efficiency is plotted against acetylene pressure in Figure 5.6 (purple squares).We compare our laser efficiency with that of a diode pumped HOFGLAS configuration reported in [3]. We reported that our observed slope efficiency was independent of pressure in the range we were working at. The slope efficiency is defined as the mid-IR laser output power divided by absorbed pump power. It can be seen that the laser efficiency of the diode-pumped configuration varies over a wide range from ~ 8% to ~ 30%. However, the slope efficiency of our OPA pumped HOFGLAS system remains close to ~ 20% over the same range of acetylene pressures for which

the laser performance was investigated. This indicates that collisional relaxation is not limiting our laser performance in this regime. This behavior suggest that we can scale the laser system by increasing the pump powers and pressures.

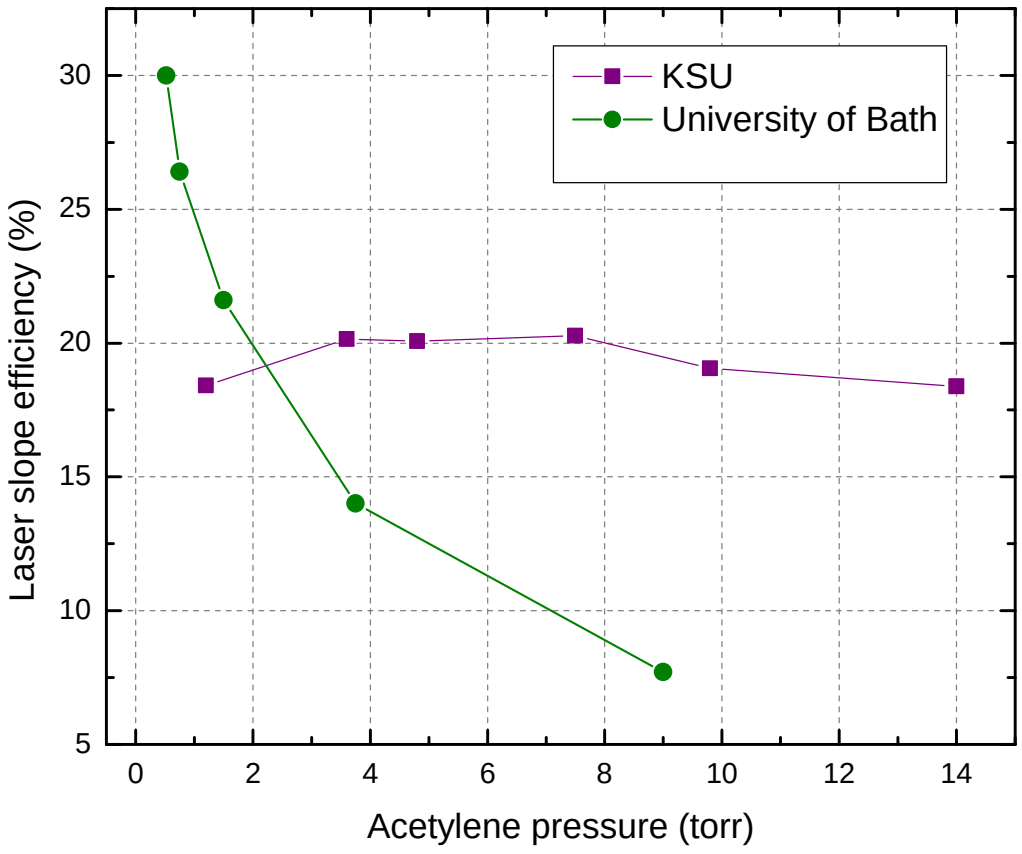

Figure 5.6: Laser slope efficiency versus acetylene pressure.

It is important to mention that we are in a regime of high pump saturation, meaning the amount of power absorbed by the gas varies along the length of the fiber, and with pressure, in a highly nonlinear way. This is seen in Figure 5 of Ratanavis et al, [37].

Threshold occurs when loss, including absorption of the gas, is equal to gain. As pressure increases in a fiber, more power must be absorbed in order to create a population inversion

throughout the fiber. However, the gain is not degraded, but rather increased, because there are more molecules contributing to lasing. It is reasonable to think that the gain will not degrade with increasing pressure because we are in a regime where the linewidth is dominated by Doppler broadening while collisional broadening is only a minor contribution. Therefore, as pressure increases, the peak of the absorption coefficient alpha still increases. We can observe this behavior by plotting absorbed pulse energy versus pressure in Figure 5.7. This plot resembles the curve for the absorption coefficient in CO_2 at 10.6 um as a function of CO_2 pressure shown in [92].

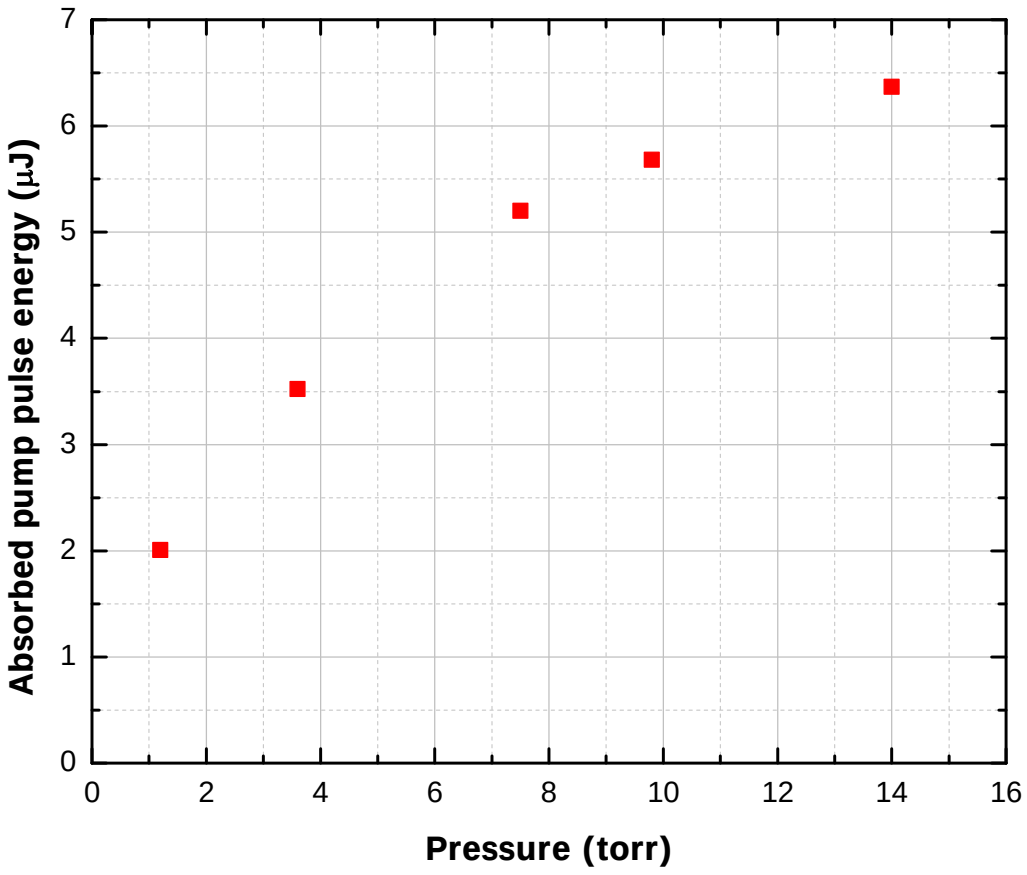

Figure 5.7: For a certain coupled input pump pulse energy, absorbed energy can be plotted versus pressure.

Indeed the nearly flat efficiency indicates that collisional losses do not dominate, and are probably slow compared to the other relevant laser lifetimes. Therefore, both absorbed power and gain have increased in a proportional way, and so the slope efficiency above threshold remains unchanged.

Threshold of lasing at each acetylene pressure was found by applying a linear fit to the linear regime of the graphs in Figure 5.4 and is shown in Figure 5.8.

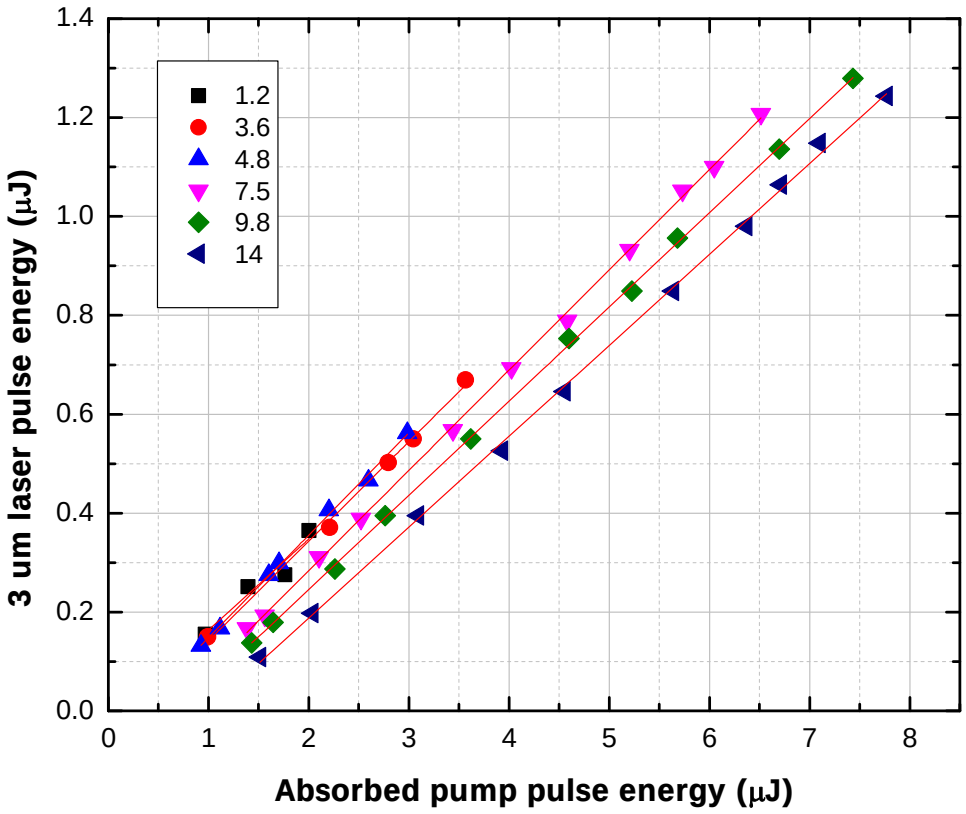

Figure 5.8: To find threshold of lasing at each acetylene pressure, linear fits have been applied to the plot of 3 μm power versus absorbed pump power.

The intercept (b) and slope (a) of each linear fit can be used to calculate threshold values as shown by Equation 5.1 and Equation 5.2.

$$y = ax + b \tag{5.1}$$

$$Threshold = -\frac{b}{a} \tag{5.2}$$

As shown in Figure 5.9, for our setup, lasing threshold increases linearly with pressure. Experimentally, it was not possible to acquire data exactly at threshold because the amount of power detected by energy meter was within the background noise level of the energy meter and usually lasers are noisy at threshold.

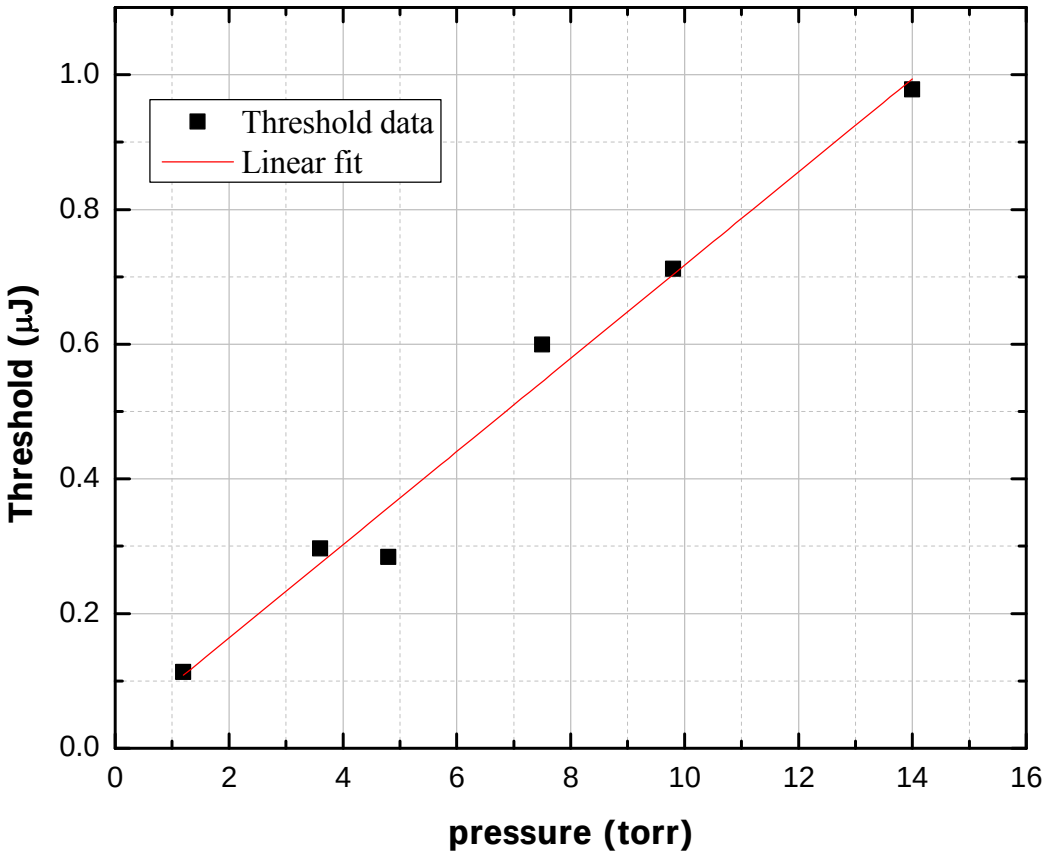

Figure 5.9: Threshold of lasing versus acetylene pressure.

Laser operation results are compared for the OPA pumped HOFGLAS and amplified modulated diode pumped HOFGLAS under the same condition (10 torr of acetylene pressure, ~ 10.5 m fiber length, and relatively similar fiber loss at pump wavelength) as shown in Figure 5.10.

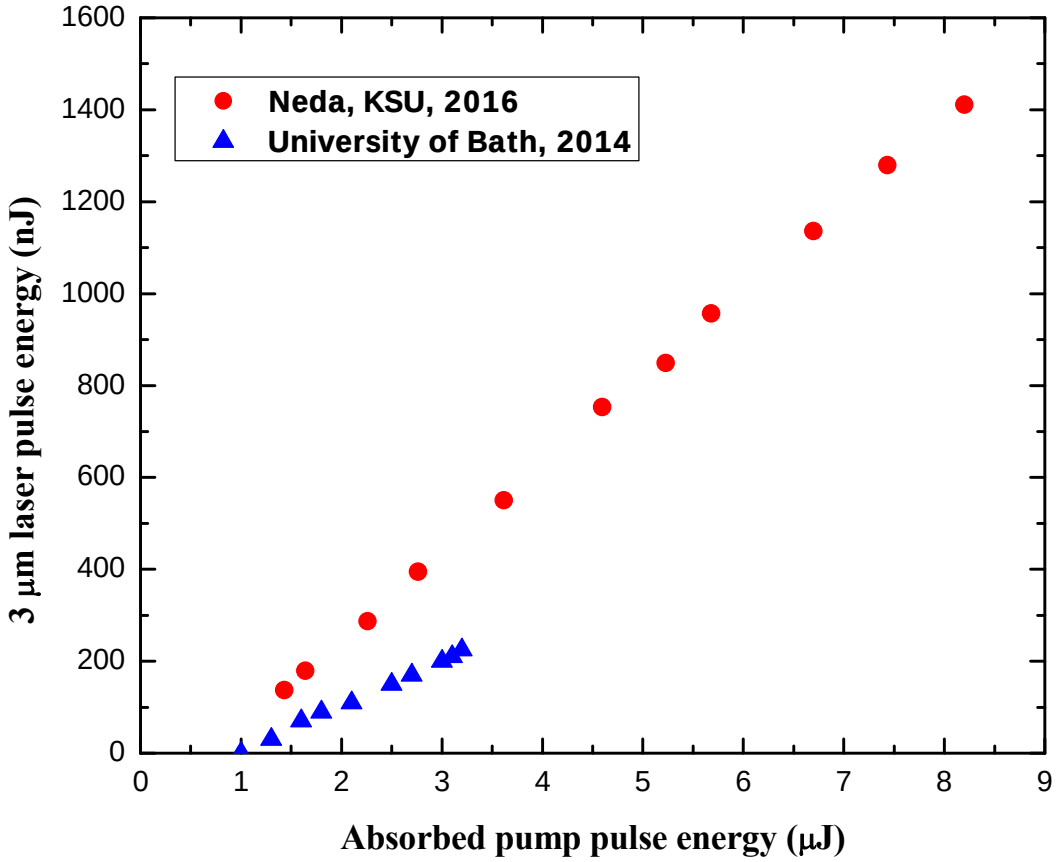

Figure 5.10: At 10 torr pressure and ~ 10.5 m of fiber, laser operation results for OPA-pumped (circle/ red plot) and amplified modulated diode-pumped (triangle/blue plot) have been compared together. The square/ black plot is the prior result of operating OPA-pumped HOFGLAS with a shorter length of fiber ~ 1.5 m.

Although fiber loss at 3 μm is reported about one order of magnitude smaller in the diode-pumped HOFGLAS compared to OPA pumped HOFGLAS (1.13 dB/m for KSU and 0.1 dB/m for University of Bath), the laser slope efficiency is higher for the OPA pumped HOFGLAS under the same condition. But higher slope efficiency is obtained from the diode-pumped case at lower

pressures (~1.5 torr) as shown in Figure 5.11. The performance of two laser systems are different from each other that can be related to properties of the two pump sources.

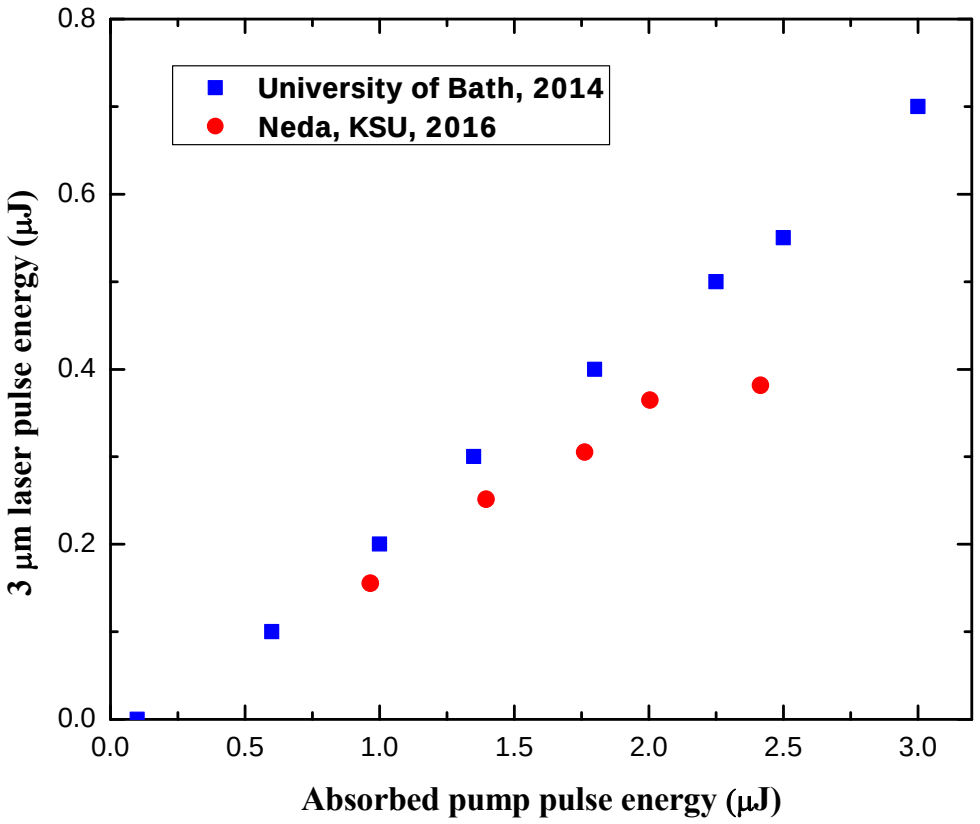

Figure 5.11: At ~1.5 torr of acetylene pressure and ~ 10.5 m fiber length, results from diode-pumped HOFGLAS and OPA-pumped HOFGLAS are compared.

Laser operation results are compared for OPA pumped HOFGLAS operation for two different fiber lengths as shown in Figure 5.12. At Figure 5.12 (a), both operations are at ~10 torr of gas pressure and 1.5 μm fiber loss are relatively similar (~0.1 dB/m). Loss at 3 μm for the prior operation is reported to be ~5 dB/m and for the recent operation is 1.13 dB/m. At Figure 5.12 (b), both operations are at ~5 torr. Improved laser slope efficiency for the recent operation can be observed from both plots.

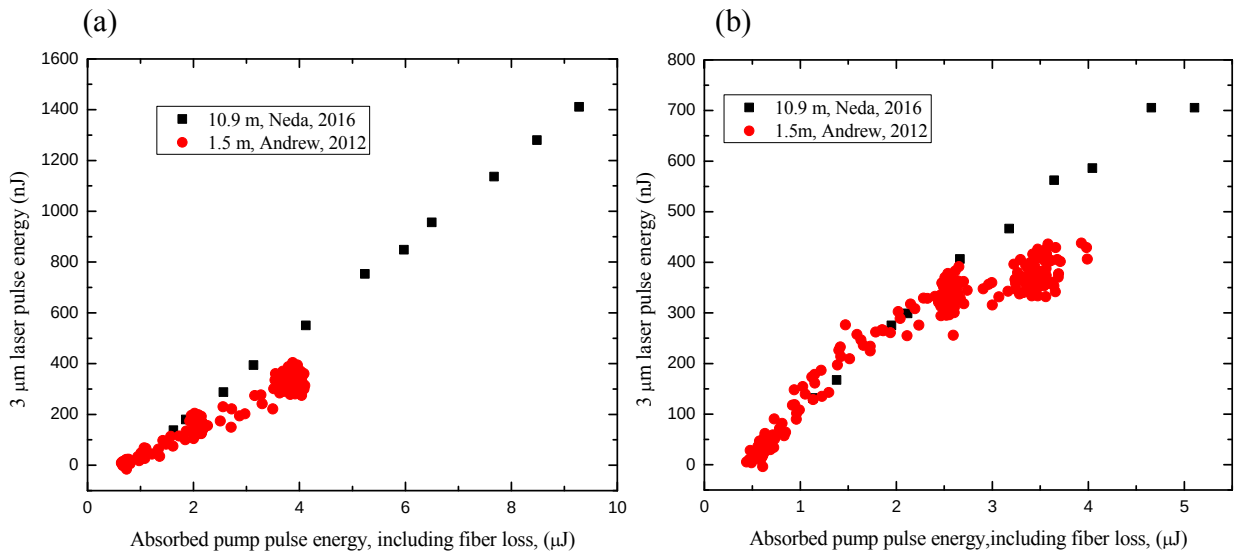

Figure 5.12: (a) At 10 torr pressure, but using different fiber lengths, laser operation results for OPA-pumped HOFGLAS have been compared together. The square/ black plot is the prior result of operating OPA-pumped HOFGLAS with a shorter length of fiber ~ 1.5 m and the circle/ red plot is the OPA- pumped HOFGLAS result using 10.9 m of fiber. (b) Operation at 5 torr acetylene pressure.

To study absorption linewidth in our acetylene HOFGLAS system, while pumping on P(13), I wrote a simple code in Python, Appendix B, to calculate absorption coefficient (α) and compare transmission through Acetylene-filled fibers versus frequency for different pressures and fiber lengths. The code uses a Voigt profile generated by "Lm fit" from Python (https://lmfit.github.io/lmfit-py/). The Voigt profile is used in the definition of absorption coefficient by Equation 5.3.

$$\text{absorption coefficient}\,(\nu) = S \times \frac{p}{k_b T} \times \text{voigt}\,(\nu) \tag{5.3}$$

Where, k_b is the Boltzman costant, p is the gas pressure and T is the gas temperature and S is the line strength that can be calculated in the code using NIST data [91] Then, we may use Beer's law, Equation 5.4, to plot transmission through gas-filled fiber versus frequency.

$$I = I_0 e^{(-\alpha L)} \tag{5.4}$$

Where α is the calculated absorption coefficient (ν) from Equation 5.3 and L is the fiber length. I applied the code for different sets of fiber lengths and pressures and the results are plotted in Figure 5.13. In my experiment, I was working with 10 torr and 10.9 m (blue curve) and it is obvious that fractional transmission through this long length of fiber at 10 torr is 100%.

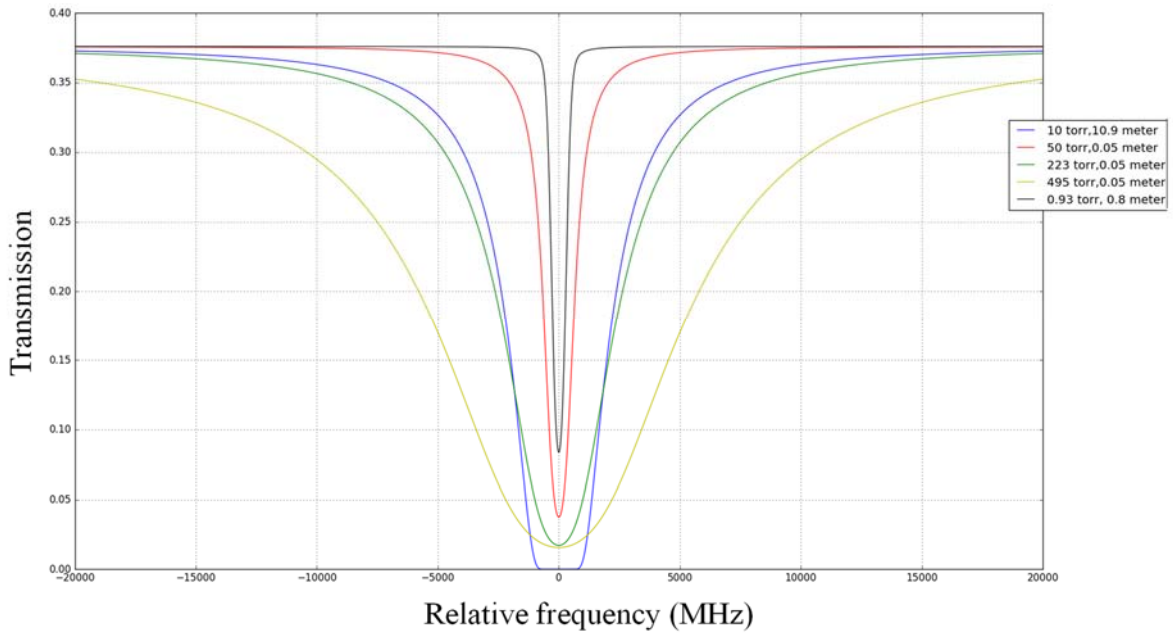

Figure 5.13: Compare transmission through gas cells with different gas pressures and different fiber lengths. Transmission (I) has the unit of V in this plot, where I_0 is 0.355 V.

5.1.2. Optimized focusing lens

In section 5.1.1., we used a focusing lens of 75 mm to couple the pump into the hollow-core fiber. The numeric aperture of the fiber matches with this focal length but in this section, we replaced the focusing lens with a 125 mm focal length lens. This focal length of the lens that couples the OPA pump beam into the fiber is chosen such that the mode of the OPA pump beam has maximum overlap with the fundamental mode of the fiber. Figure 5.14 shows the beam with diameter D, which is the $\frac{1}{e^2}$ intensity diameter of a collimated Gaussian beam, and d is the core diameter of fiber. Equation 5.5 should be used to find the optimum focal length of the lens for beam coupling into the hollow-core fiber [93]. In fact, numeric aperture of the beam ($\frac{\lambda}{\pi\omega_0}$) should be matched with numeric aperture of the fiber through the lens ($\frac{d}{2f}$). The factor 0.64 in Equation 5.5 comes from fundamental mode matching condition in Figure 5.15.

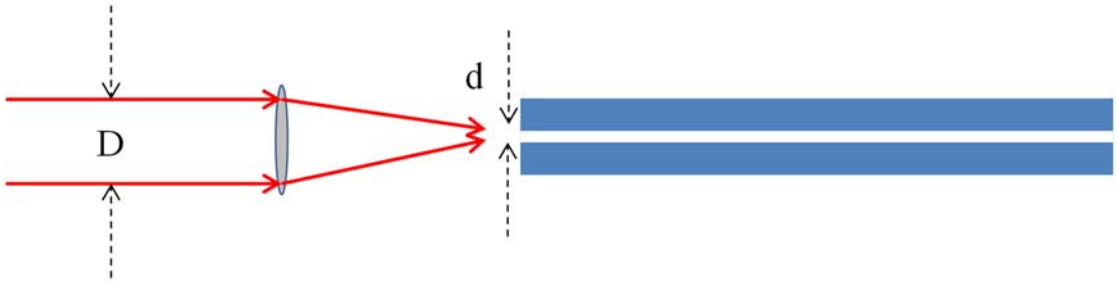

Figure 5.14: Beam coupling into hollow-core fiber. "D" is the beam diameter and "d" is the fiber core diameter.

$$\frac{4 \times f \times \lambda}{\pi \times D} \sim 0.64 \times d \tag{5.5}$$

From section 4.3.3., we know the beam sizes for the OPA output at 1532 nm and seed laser at 1532 nm do not match. Since we care about maximizing the OPA coupling into hollow-core fiber, "D" in the above equation is equal to OPA beam diameter for ~6mm. Inner core size of the hollow-core fiber is 60μm/72 μm. So, a lens with the focal length of 12.5 cm will help in coupling more of the fundamental mode of the OPA beam into the fiber.

After the light is focused at the fiber aperture, the free-space TEM_{00} mode width is proportional to the far-field divergence angle. In other words, since the plane where light leaves the fiber lies in the focal plane of the lens, the far field pattern is fed into the fiber. When the focal length is properly chosen, only the lowest order transverse mode has a low aperture loss, since the higher order transverse modes have greater angles of divergence [93]. In [93], the amplitude of a TEM_{00} beam with wavenumber k is defined ($E_{TEM_{00}}$) and then the fiber modes are represented by their amplitude distribution ($E_{EH_{1m}}$). The coupling of each fiber mode to the TEM_{00} mode is determined by the overlap integral, which is a function of the Gaussian width. Numerical analysis was performed to plot the percentage of coupled energy as a function of the TEM_{00} mode width. Figure 5.15 shows the optimum spot diameter of the free-space beam is ~ 0.64×d to couple $E_{EH_{11}}$. This is mostly single mode coupling but with ~98% of that light coupling into the fiber. It also shows that if we choose the focal length of the lens to give the free-space beam a spot diameter of ~ 0.5×d then a superposition of $E_{EH_{11}}$ and $E_{EH_{12}}$ will couple 99.85% of the light into the fiber.

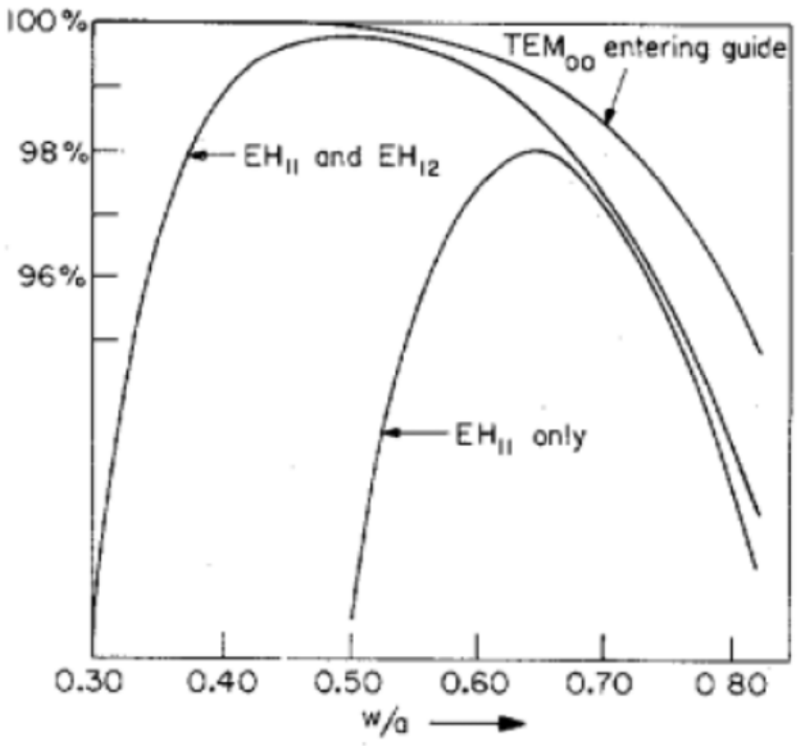

Figure 5.15: Plot of coupling efficiency of EH_{1m} mode into the hollow-core fiber with radius of a. Optimum spot diameter of free-space beam is ~ 0.64×d [93].

To apply the above modification, the acetylene-filled HOFGLAS system was operated one more time using the optimized focusing lens. The plot of laser pulse energy versus input pump pulse energy is shown in Figure 5.16.

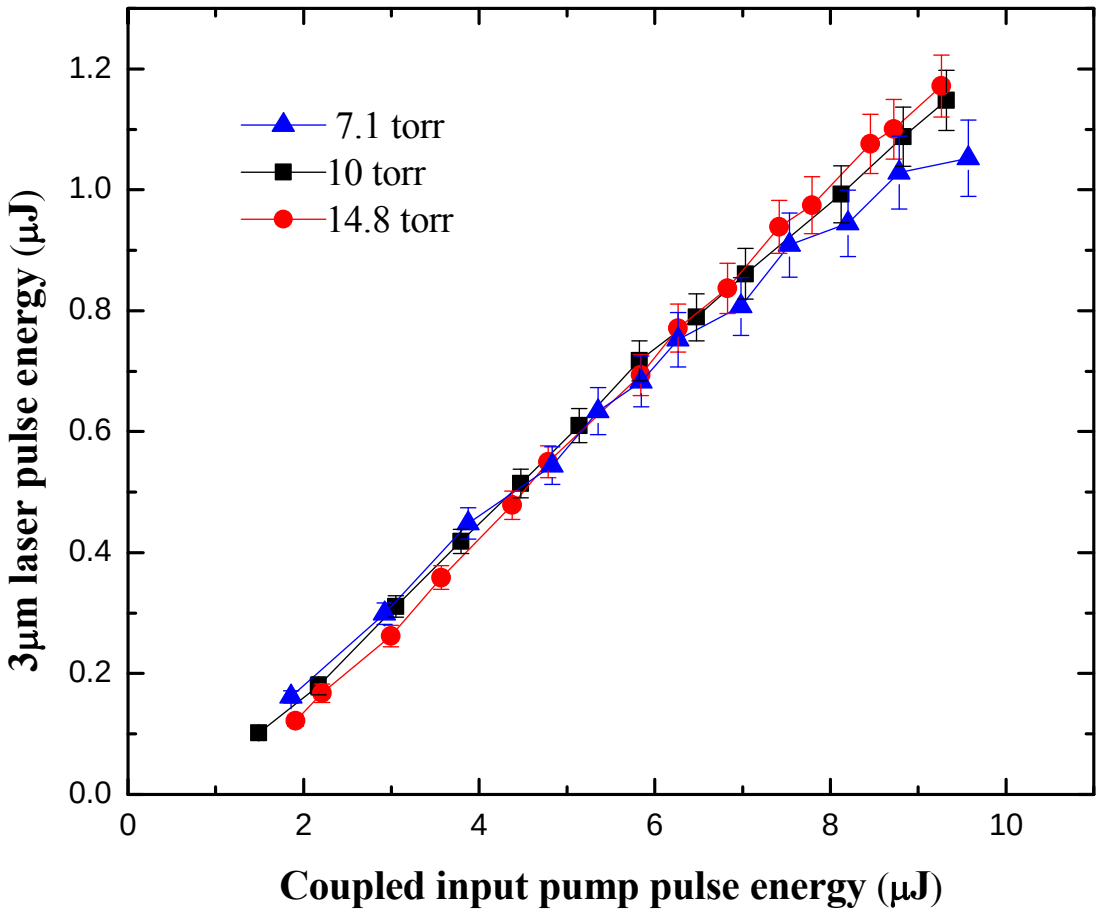

Figure 5.16: produced mid-IR laser pulse energy versus coupled input pump pulse energy.

Acetylene-filled HOFGLAS was operated at three pressures and observations of saturation and slope efficiency are the same as the previous operation as shown in Figure 5.17.

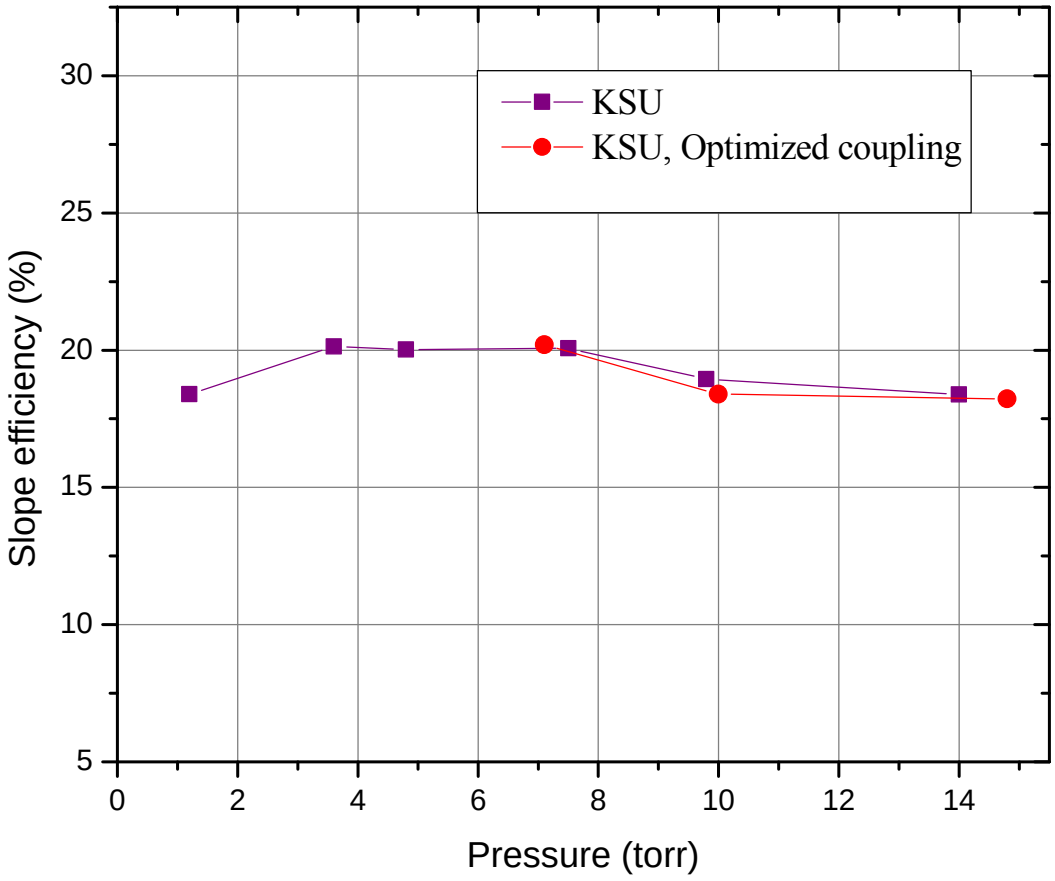

Figure 5.17: A plot of slope efficiency as a function of acetylene pressure, where slope efficiency is the ratio of mid-IR power over absorbed power by gas. The purple plot is for obtaining the highest power operation that is discussed in section 5.1.1. and the red plot is the operation of the same setup for obtaining the highest mode quality.

In Figure 5.18, the produced mid-IR pulse energy as a function of absorbed pump pulse energy is represented. The highest produced mid-IR laser pulse energy in this operation was ~ 1.17 μJ, which is evidence for more single mode operation of the laser system based on above explanation. In section 5.2.1., I performed M^2 measurement on the highest produced mid-IR laser beam while this focusing lens of 12.5 cm was installed inside laser system and M^2 value of 1.15 was obtained, demonstrating a near diffraction-limited operation of the laser system.

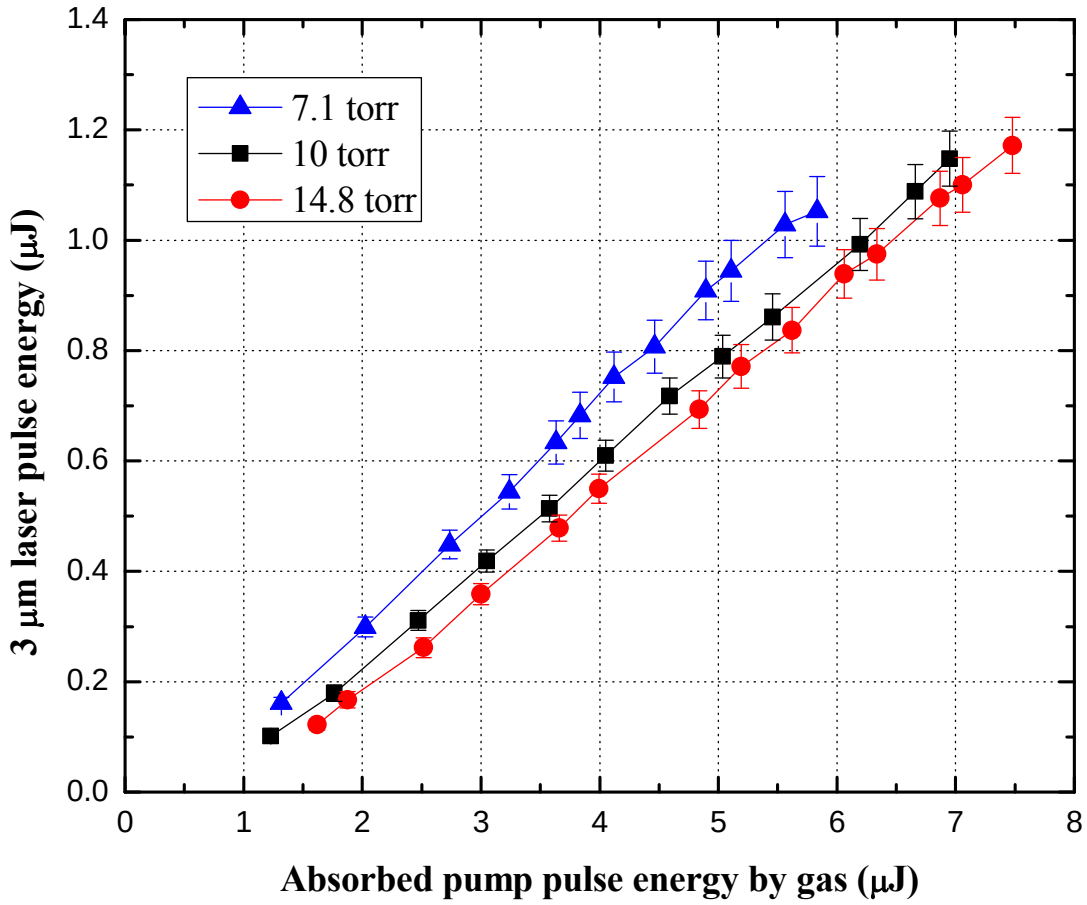

Figure 5.18: Plot of produced mid-IR laser pulse energy versus absorbed pump pulse energy only by gas.

5.2. M^2 measurement of 3 μm output beam

In this section, the mode quality of the produced mid-IR laser from acetylene-filled HOFGLAS will be investigated twice. Section 5.2.1. will present the near diffraction-limited performance of the laser system using the optimized focusing lens described in section 5.1. and 10.9 m of fiber # 15 in Table 3.3. [25]. Section 5.2.2., describe the first time investigation of mode quality of acetylene HOFGLAS using fiber #6 in Table 3.1. [77].

5.2.1. Near diffraction-limited performance of acetylene HOFGLAS

M^2 measurements were performed to characterize the laser mode quality. M^2 value provides information about the beam's propagation properties and achievable brightness. The laser was operated at 10 torr and 1.53 μm pump coupling was optimized for single mode operation, as described in section 5.1., and 1.17 μJ was the maximum observed 3 μm pulse energy.

The M^2 measurement was performed by taking several beam profiles of the 3 μm laser output at the Rayleigh range and further away from the Rayleigh range of the focus of a fixed position lens in free space. The Rayleigh range of a Gaussian laser beam is the distance from the beam waist position on propagation axis where the beam radius is $\sqrt{2}$ times bigger than the beam waist. The beam profiles were measured using a CaF2 plano-convex lens of 150 mm focal length and scanning a 20-μm wide slit across the transverse axis (x) of the output beam at different positions along the propagation axis (z). Figure 5.19 represents a series of mid-IR laser beam profiles that were measured at the highest 3-μm pulse energy produced by the laser at the focus of the 150 mm focal length lens. This method measuring the M^2 requires a few hours due to working with a low repetition rate laser (the 30 Hz repetition rate of our OPA is defined by the Nd:YAG laser which is the pump for the OPA). The laser operated stably through the measurement. The stable operation can be seen in the smoothness of the curves in Figure 5.19 and the small error bars in Figure 5.18. We also examined our data more closely for quantitative temporal stability information. The shot-to-shot variations on power were only about 10% as shown in the error bars of Figure 5.18. The 2% error bar on the large w values of Figure 5.20 are consistent with power fluctuations, since they are taken on 50 point averages and consequently should be $\frac{10\%}{\sqrt{50}}$ or 1.4% , assuming random noise. The statistical error bar on the resulting M^2 fit is only 0.014 at 1.15 μJ. Scaling this by the $\sqrt{50}$ gives $M^2 = 1.15 \pm 0.15$ for single-shot, assuming random noise. The

error bar shown in the plot reflects the uncertainty on the center wavelength of the 3 micron output, which dominates the uncertainty in the M^2.

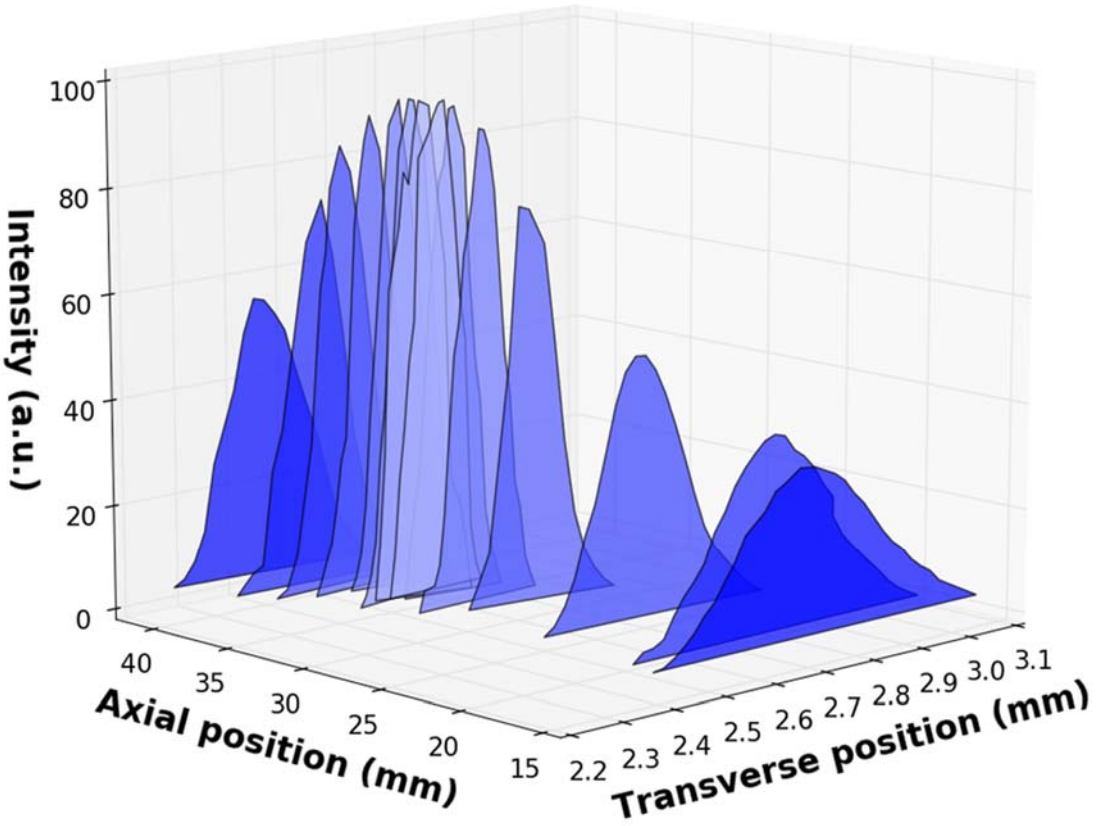

Figure 5.19: Beam profile measurements along several axial positions in the Rayleigh range and further away from the Rayleigh range of a focusing lens in front of the collimated 3 μm beam.

The beam widths for each profile in Figure 5.19 were obtained using the ISO standard D4σ method and were fitted to the definition of M^2 [38, 94] with an averaged wavelength of 3.143 μm. Figure 5.20 shows beam widths as a function of axial position and an M^2 value of 1.15±0.02 is obtained from fit to this data in a Matlab code, appendix C. The error in the M^2 value, as explained above, comes from fitting the measured beam widths to the definition of M^2 in [38] .

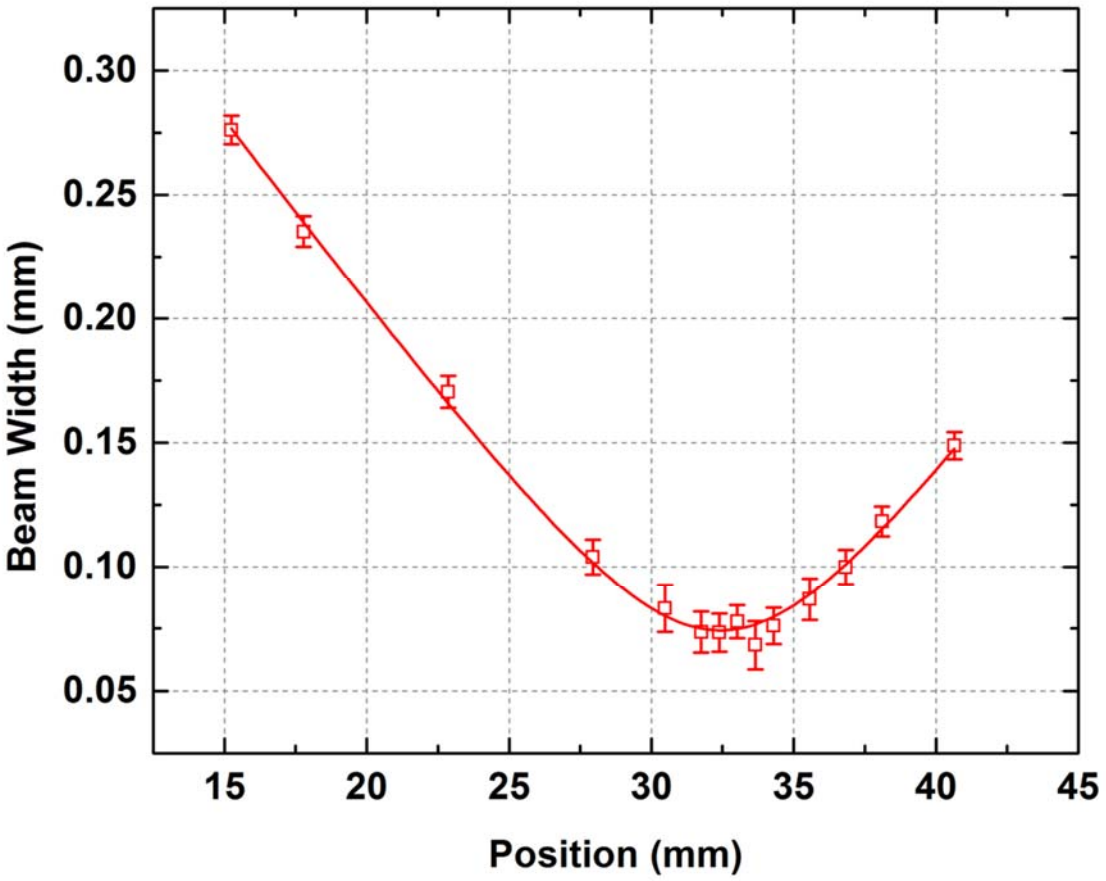

Figure 5.20: Beam waist values from the beam profile measurements are plotted versus axial position and fitted into the M^2 definition.

The M^2 of the laser output was also measured for other produced mid-IR energies and the HOFGLAS was operated at 10 torr of acetylene pressure, as shown in Figure 5.21. We observed that the beam quality of the laser was almost uncompromised and at the highest pulse energy, we obtained M^2 of 1.15±0.02. Then, the reproducibility of the M^2 measurement was checked at two powers using a 50 μm wide slit. In both cases, the M^2 values were reproduced, as shown in red at Figure 5.21. These results show the stable and near-diffraction limited performance of the acetylene-filled HOFGLAS system.

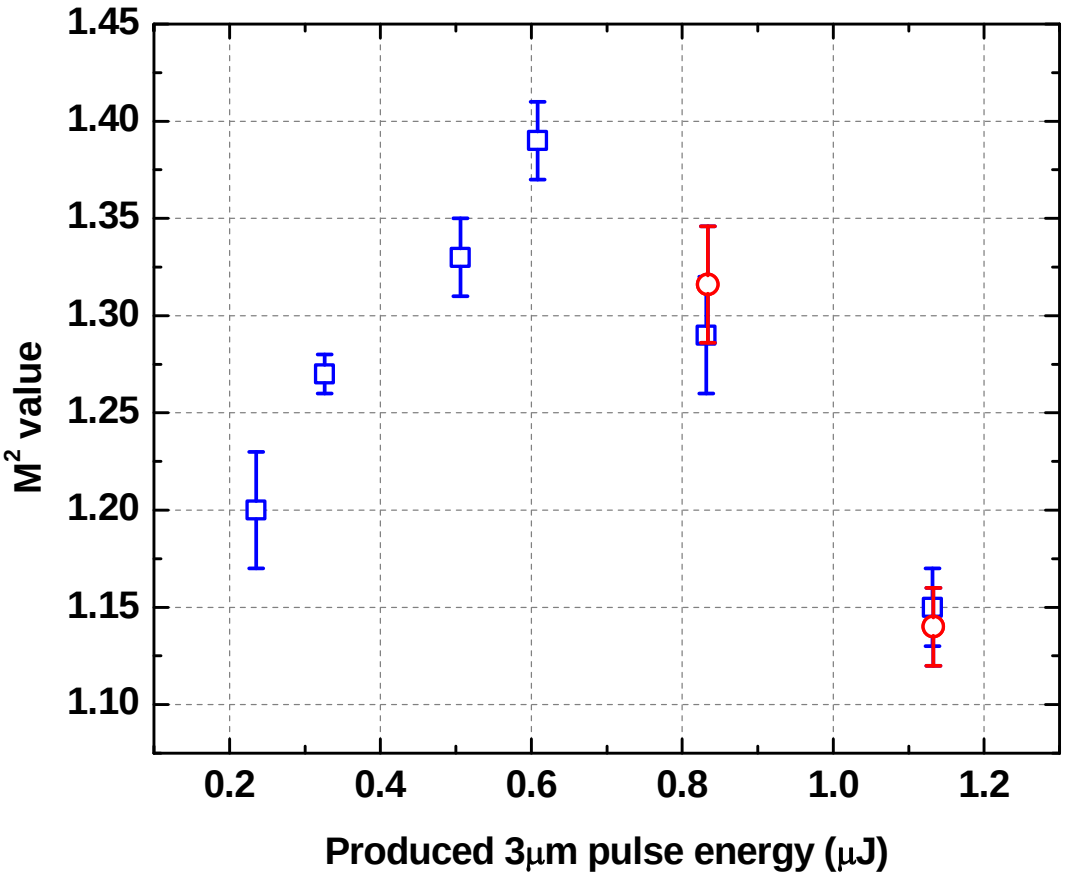

Figure 5.21: Plot of M^2 as a function of 3 μm laser pulse energy. At two produced laser pulse energies, M^2 reproducibility were checked under completely different laboratory situations.

5.2.3. First time investigation of Acetylene HOFGLAS mode quality

The First-time mode quality was investigated for fiber #6 in 2015 and an $M^2$of 1.71 ± 0.19 was obtained [77]. Then, attempts were made to use fibers with smaller core size and closer to single mode operation. In this section, I present the first results of beam quality measurements. We went through the same procedure as described in section 5.2.1, Figure 5.22 shows the results. A similar piece of the fiber was sent to Colorado and Andrew Jones performed an imaging using an InSb array on the passive guidance of a 3 μm beam through the fiber.

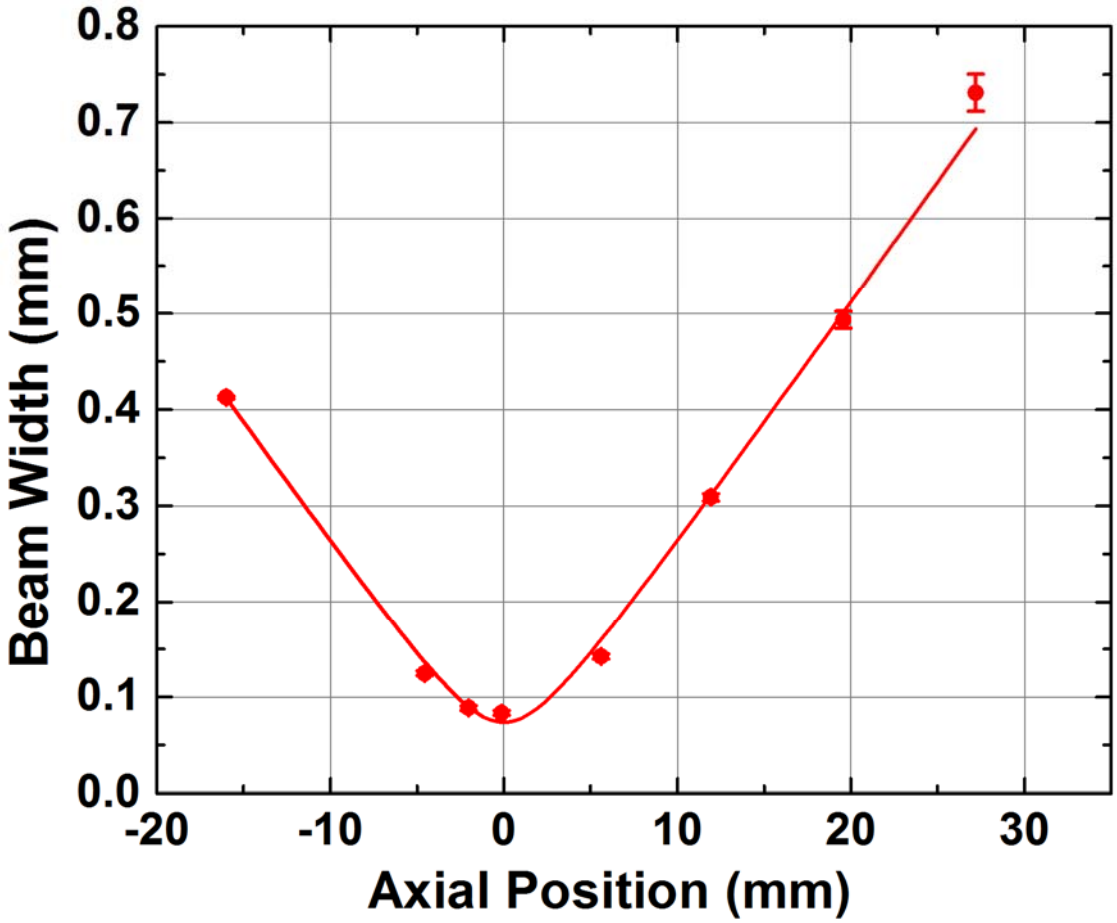

Figure 5.22: Beam widths versus axial position and the fit to data to find M^2 value.

He also checked that the modal content is not alignment sensitive. Since, our beam profile overlapped pretty well on the beam profile of his measurement and his measurement was not alignment sensitive, we concluded that our laser operation was fairly single mode, as shown in Figure 5.23. But, M^2 results showed a value of 1.71 ± 0.19 and to have a near diffraction-limited operation M^2 value it should be below 1.2 while an M^2 value of 1 is for a perfect Gaussian beam [40].

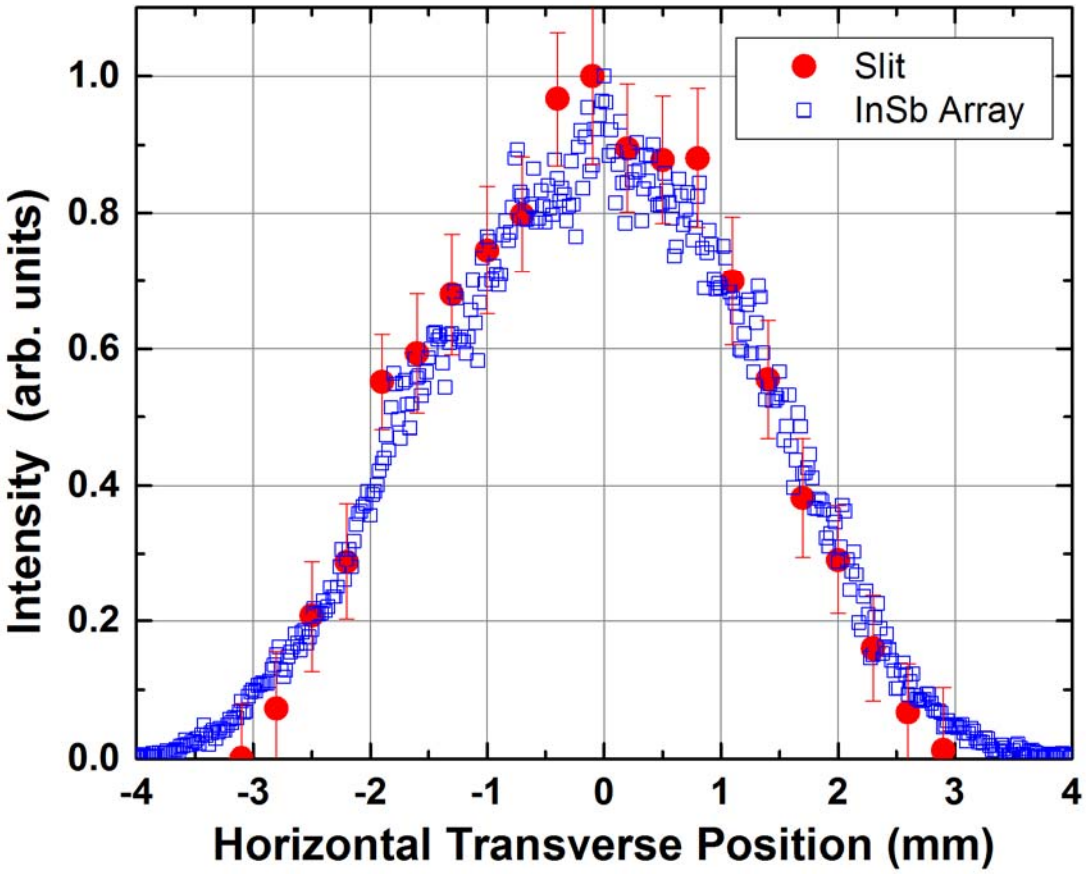

Figure 5.23: Red circles show the transverse beam profile for the mid-IR emissions from our acetylene HOFGLAS measured in JRM lab and blue squares shows the beam profile of a passive guidance of 3 μm beam through the same fiber and imaging it using a InSb array in NIST at Colorado.

It is important that a laser produces a beam with near diffraction-limited quality because a powerful method of scaling these laser systems to high power is through coherent beam combining of multiple acetylene HOFGLAS laser systems. This requires high mode quality and we were able to obtain the near diffraction-limited laser operation in our most recent results.

Chapter 6 - Continuous Wave HCN-filled HOFGLAS

6.1. Theory of HCN-filled HOFGLAS

Chapters 4 and 5 have focused on the produced mid-IR laser from acetylene-filled HOFGLAS. In this chapter, attempts toward first-time demonstration of HCN-filled HOFGLAS is presented and my contribution to this work is highlighted.

An analytical study of continuous wave HOFGLAS by our collaborators in University of New Mexico demonstrates the possibility of observing continuous wave lasing in HCN-filled HOFGLAS [37]. This laser is a small quantum cascade laser because the pump and laser wavelengths are different from each other for about 1% and the overall laser efficiency is predicted by numerical simulations to be ~55% for long interaction length of pump and gas medium. The possibility of obtaining high efficiencies for these lasers makes them a good candidate for coherent beam combining. The principle behavior of these small quantum defect lasers is defined by effective vibrational life times and rotational relaxation rates of the molecular gas [37]. HCN molecule has one bending (ν_2) mode and two stretching modes (ν_1 & ν_3). The three atoms in HCN molecule have different masses and that is why none of HCN normal modes has a definite symmetry as shown in Figure 6.1. In each vibrational state of HCN molecule, rotational states population follows a Boltzmann distribution [95-97]. The possibility of continuous wave lasing in a HCN-filled HOFGLAS system is investigated for tuning the pump on resonance with transition from $J = 8$ ground vibrational state (000) to $J + \Delta J = 9$ excited vibrational state (002), which is $2\nu_3$, and observing lasing from $j = 9$ rotational state in the excited vibrational state (002), which is $2\nu_3$, to $j + \Delta j = 10$ rotational state in the ground vibrational state (000) as shown in Figure 6.2.

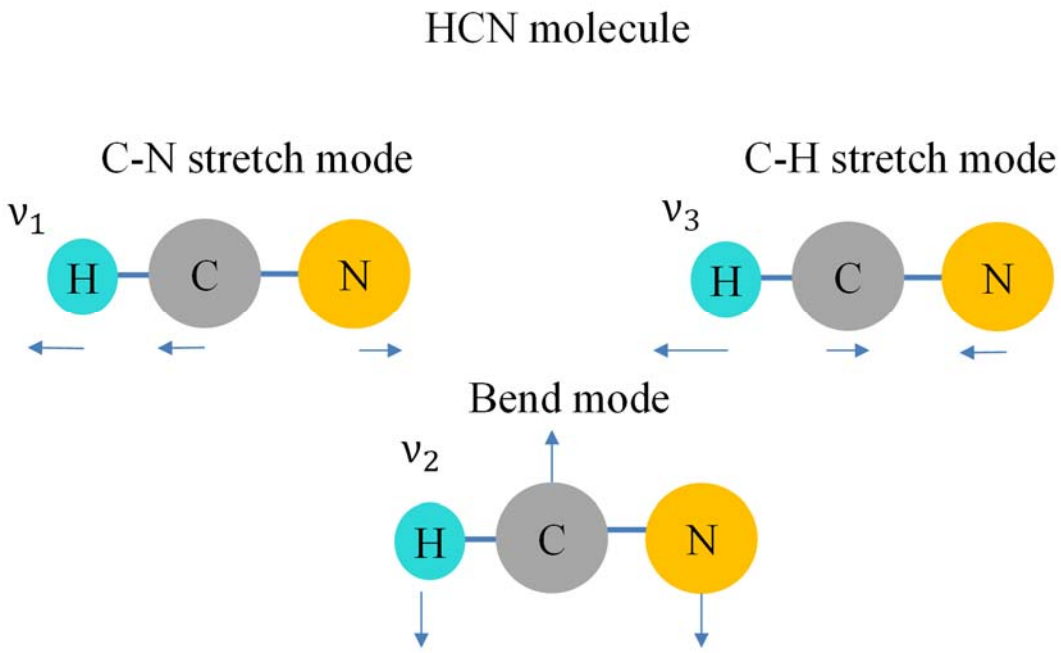

Figure 6.1: HCN normal modes. The motions of the molecule's atoms are indicated by small arrows around atoms.

Based on the numerical calculations [37], it is possible to obtain the maximum predicted lasing efficiency with 5 torr of HCN pressure inside 1.5 m of 20 μm PBGF of 0.02 dB/m and pump power of 5 W while output coupling loss will be ~ 25%.

One of the most important issues toward demonstration such a laser system is the resonator design. The resonator design can be based on dichroic optics or polarization optics. Dichroic optics may reflect the laser wavelength and transmit the pump wavelength however very sharp dichroic mirrors are needed to be used in this small quantum defect laser because pump wavelength is only about 1% shorter than lasing wavelength. On the other hand, polarization optics may allow pump light with a certain polarization to enter the cavity resonator where all optics are very reflective for orthogonal polarization. Andrew Jones worked on continuous wave acetylene-filled HOFGLAS

designs based on polarization optics [74] but no lasing was demonstrated because of alignment challenges and lack of high power pump source. In the next sections, my contribution toward demonstration of continuous wave HCN-filled HOFGLAS using sharp dichroic mirrors for the laser resonator will be discussed in details. Laser setup is built and stability condition calculation for the proposed cavity is investigated in addition to performing recoupling measurement outside of the laser setup.

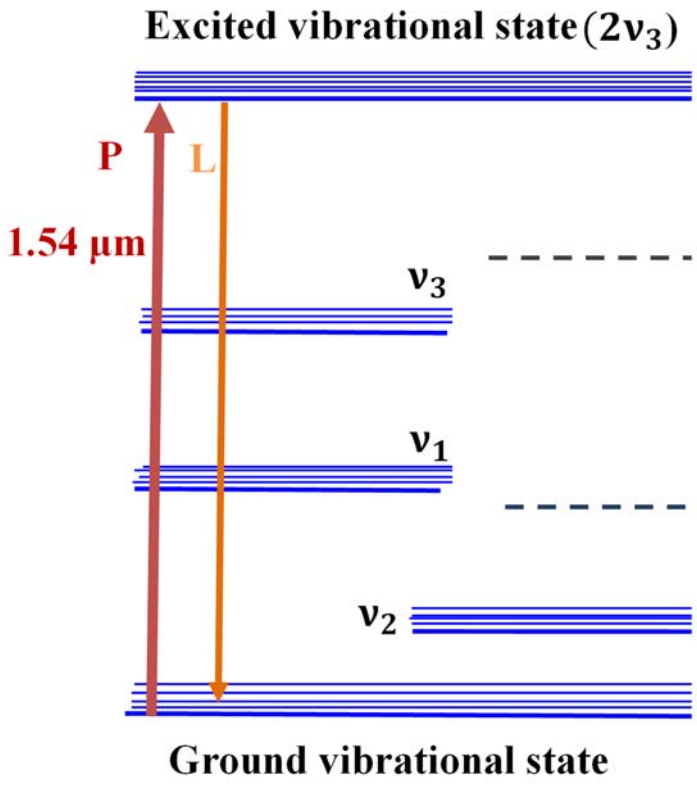

Figure 6.2: Energy level diagram for HCN molecule based on HITRAN information. Pumping candidate is from ground vibrational state to $2\nu_3$ excited state and there is the possibility of observing continuous wave quantum defect lasing.

6.2. HCN-filled HOFGLAS configuration

A new HCN-filled HOFGLAS setup was built after receiving sharp plano dichroic mirrors from Precision Photonics company to be used as the cavity resonator. The dichroic mirrors have different transmission and reflection at different wavelengths and they are made to be used in our specific laser system. Figure 6.3 is a schematic of the setup. Pump, fiber, and resonator will be discussed in details in the subsections. Pump is a collimated beam with 5 mm beam waist. A customized high power polarization-dependent Faraday isolator with the aperture size of 7 mm was purchased from Thorlabs Company and a combination of Quarter Wave Plate (QWP) and Half Wave Plate (HWP) were used to turn input polarization and maximize pump power after the isolator. To attenuate the pump at the alignment stage in addition to create a second pump beam path for backward coupling, a combination of Polarizing Beam Splitter (PBS) and a Half Wave Plate (HWP) are used after the isolator. A 15 mm aspherical coupling lens was selected to be used before and after the vacuum chambers based on matching the fundamental pump mode coupling into the 20 μm Photonic Band Gap (PBG) fiber from NKT Photonics Company (HC-1550-02), the concept has been described in chapter 5, section 5.1.2. After the laser cavity, another dichroic mirror has been used to distinguish pump from laser wavelengths and detect them using appropriate detection system that could be an Optical Spectrum Analyzer, a combination of large-area photodetector and scope, or a power meter. Maximum coupling efficiency of ~ 70% was achieved for pump coupling into the fiber. This reported coupling efficiency is the ratio of pump power at the output of the fiber and the input power recorded before the focusing lens at the entrance side of the fiber. So, corrections for passing through vacuum chamber windows, a spherical lens, and fiber loss have not been considered. Unfortunately, the only aspherical lenses with 15 mm focal length in the market have small aperture size (~ 5 mm) which is about the beam

size (5mm). So, the lens might clip the pump beam if the beam won't hit perfectly at the center of the lens. This might affect on the spatial intensity distribution of the pump beam and affect on the amount of pump coupling into the fiber. A telescope may not be used to solve this problem because a telescope changes the beam size and a new lens with adjusted focal length should be used to satisfy the perfect mode matching. The new lens will have a smaller focal length and physically it is not possible to put the lens closer to the fiber end because fiber end is inside vacuum chamber; however, lens is placed outside of the vacuum chamber. The thickness of the front window and flange thickness of the vacuum chambers are limitation for getting as close as we want to the fiber end.

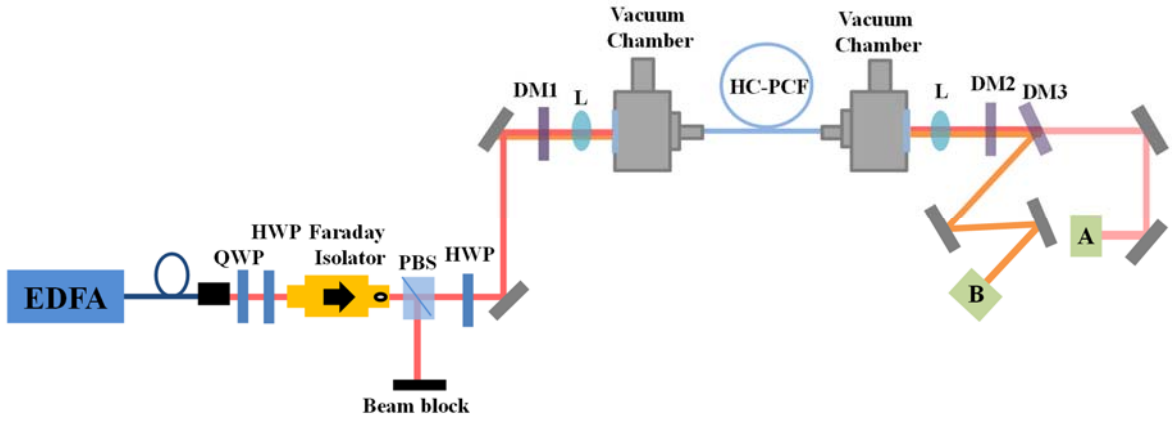

Figure 6.3:HCN-filled HOFGLAS setup. Pump is an Erbium Doped Fiber Amplifier at ~ 1.5 µm. A combination of Quarter Wave Plate and Half Wave Plate have been used to tune polarization of the incident pump light on the polarization dependent Faraday Isolator for maximum pump power. A combination of a Polarizing Beam Splitter and a Half Wave Plate are used for attenuating the pump in the alignment procedure. Dichroic Mirror1 and Dichroic Mirror 2 are used as cavity resonators. Focusing lenses (L) are used to focus the pump on the Hollow Core Photonic Crystal Fiber before the Vacuum Chamber and collimating beams after the Vacuum Chamber. Dichroic Mirror 3 is used to distinguish pump and laser beams to detect them at A and B using appropriate detection system.

Using Kagome fibers with very small core size like fibers with #s 11, 12, and 13 from Table 3.2., which are hypocycloidal core shape with 1 missing cell and 6 rings in the cladding,

might be a solution. Because their core size of ~ 28 μm almost match with the numerical calculation in [37]. In the numerical calculation using a 20 μm core diameter fiber and 5 W power has been assumed and if 28μm fiber will be used instead the power level should be scaled up to ~ 10 W for the same cavity with the certain amount of loss. I did not have access such fibers at the time of working on this setup and never tried it. In the following subsections, the pump, fiber, and cavity resonator, that are used the HCN-filled HOFGLAS, are discussed.

6.2.1. High power 1.5 μm continuous wave pump

A high power 1.5 μm continuous wave Erbium Doped Fiber Amplifier (EDFA) from Manlight company (HWT-EDFA-3RU-46-1) was used as the pump source for HCN-filled HOFGLAS operation. Figure 6.4 is a picture of the EDFA, which is a double clad fiber amplifier that can go up to 40 watts of CW power. Figure 6.5 shows a measured output power from the EDFA versus its current.

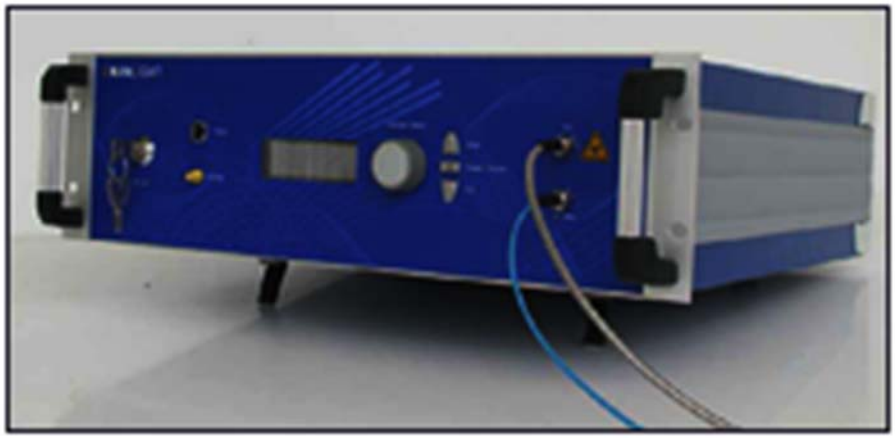

Figure 6.4: Picture of the high power (up to 40W) EDFA from Manlight company, 1.5 μm fiber amplifier, HWT-EDFA-3RU-46-1.

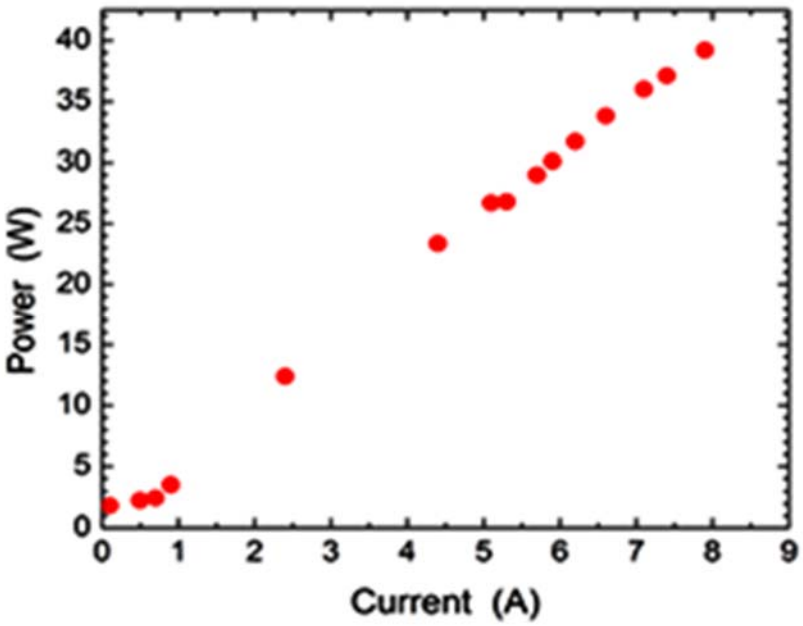

Figure 6.5: Measured output power from Manlight 1.5 µm fiber amplifier, HWT-EDFA-3RU-46-1.

In high power double clad amplifiers, the single mode core with small numeric aperture is surrounded by a lower index and higher numeric aperture cladding area. Therefore, cheaper multimode pump can be used. The signal wavelength, that should be amplified, is coupled into the single mode doped core and pump is mainly coupled into the cladding area to excite transitions in the core's dopant ions. The amplified signal light propagates through the fiber and there are Fiber Bragg Gratings (FBG) at the two ends of the fiber that act as cavity mirrors. The spectral contents related to the pump and amplified signal are dependent on the dopant material in the fiber, in our case Er. The Manlight EDFA that we used is a two-stage amplifier, i.e. a low power preamplifier stage and a high power amplifier stage. The preamplifier stage is for proper seeding of the second high power amplifier stage. In the preamplifier stage a single clad doped fiber is used and input coupled mW level CW power will be amplified to a hundred mW. If the high power stage won't be seeded appropriately, then Amplified Spontaneous Emission (ASE) in the high power stage

causes self-lasing. Self-lasing produces large spikes in output power and it may damage fiber due to nonlinear effects such as fiber-fuse.

The high power Manlight EDFA has a collimator at its output. The beam, which propagates in free space after the EDFA collimator, is then fiber-coupled and a small fraction of it is sent into an Optical Spectrum Analyzer (OSA). Figure 6.6 shows the measured spectrum of the EDFA output.

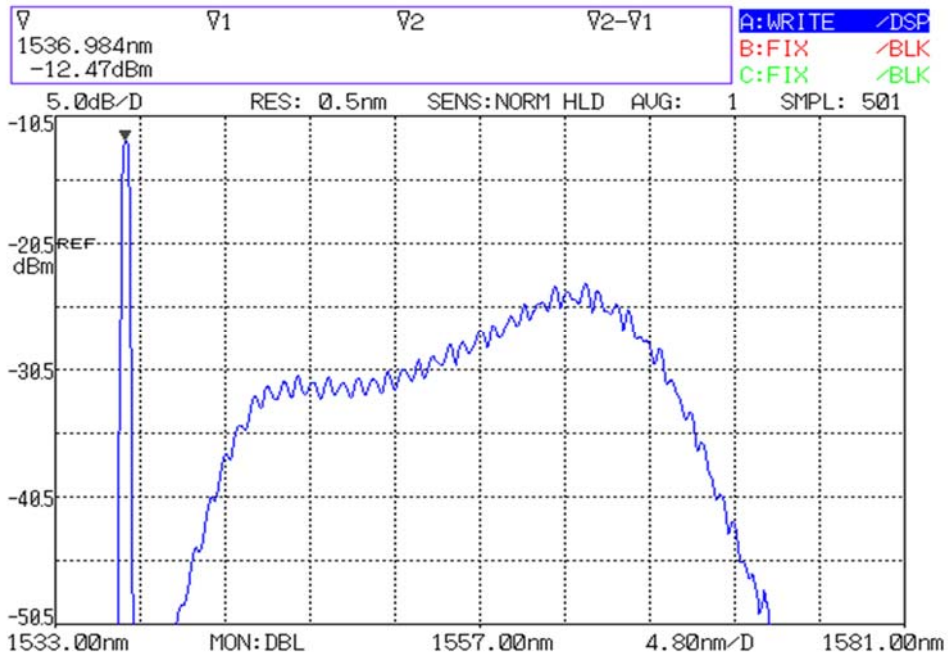

Figure 6.6: High power Manlight EDFA output spectrum, which is measured by OSA. The spectrum is recorded by Manasa Thirugnanasambandam.

We expected to observe most of the power at the desired wavelength of ~ 1537 nm for running the HCN-filled HOFGLAS but as the spectral content of the EDFA was investigated, it was found to be contaminated with ASE when seeded at wavelengths <1550nm. About 50% of the output power was distributed in the ASE wavelengths. Therefore, nearly 50 percent of the EDFA power can not be used as pump power in the fiber. But, still we may achieve 15-20W at ~1537nm

and should be able to hit pump power levels beyond the threshold of lasing in HCN-filled HOFGLAS based on the calculation [37].

The output of the EDFA is randomly polarized. On the other hand a polarization dependent faraday isolator must be used to protect the EDFA from back reflections. Therefore, combination of a Half Wave Plate (HWP), Quarter Wave Plate (QWP), and Polarizing Beam Splitter (PBS) were used to linearly polarize the EDFA output. There was a maximum of ~20% loss in the pump power as the beam passes through HWP, QWP, PBS, and the Faraday isolator.

6.2.2. Hollow-core fiber with small core size

The numerical calculation predicted an operation with 20 μm core size of a HC-PCF. We used a 10 μm core size PBG HC-PCF to make the setup work which lowers the required pump power. The fiber was purchased from NKT Photonics, HC-1550-02 and its cross section is shown in Figure 6.7. The fiber has low loss (0.015 dB/m) around 1.5 μm and its loss spectrum is shown in Figure 6.8.

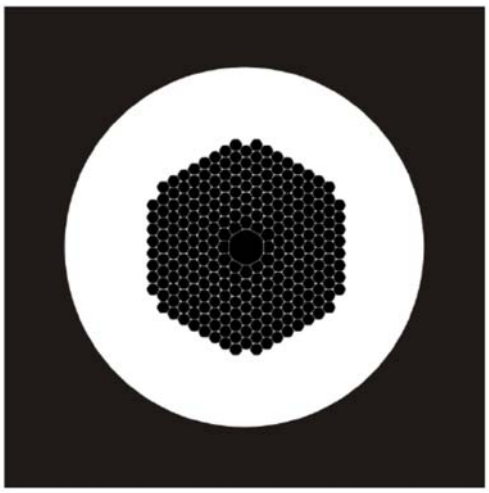

Figure 6.7: NKT Photonics, PBG fiber cross section. The fiber has 10 μm core sizer and fiber part number of HC-1550-02. The fiber can be filled with gas and the Numerical Aperture of this fiber is ~ 0.2.

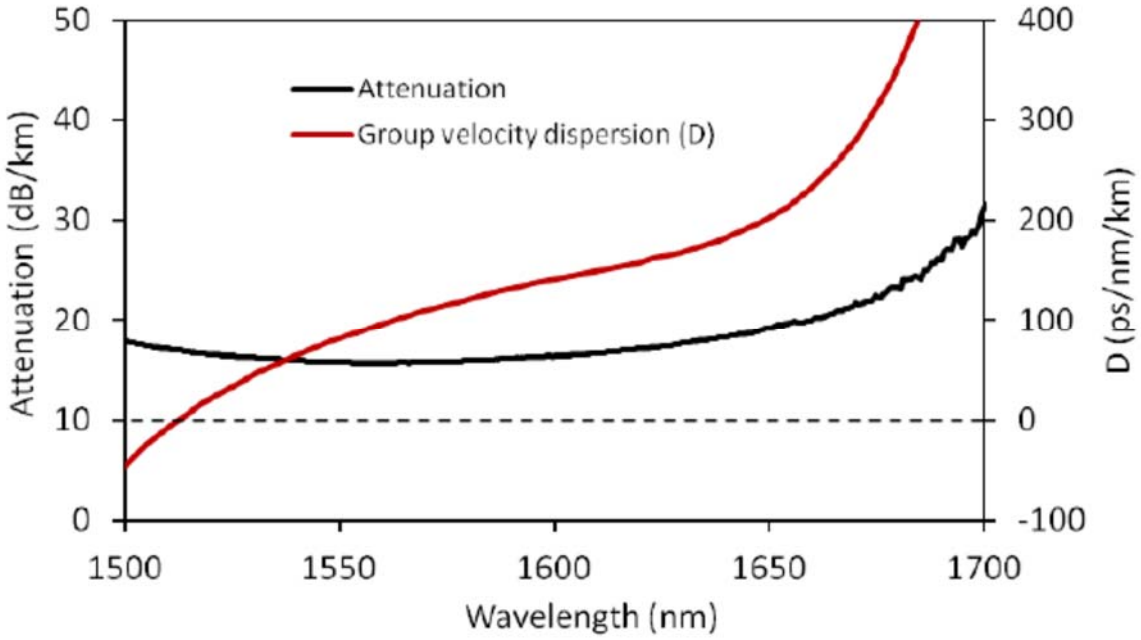

Figure 6.8: NKT Photonics, PBG fiber (HC-1550-02) loss around 1550 nm (black curve). The fiber has low loss around 0.015 dB/m.

The two ends of the fiber are installed inside vacuum chambers. Fiber holder design is shown in Figure 6.9. Two ultra-torr vacuum fitting adaptor, SS-1-UT-A-4, from Swagelok were purchased and welded to a cylindrical stainless steel tube from both sides. Then, the fiber holder was leak-checked before being used in vacuum chambers. For the side of fiber holder, inside vacuum chamber, the fiber slides through a drilled rubber cascade and the SS-1-UT-A-4 inner parts push against the rubber cascade for sealing purpose. The other side of the fiber holder, outside of vacuum chamber, is designed to keep the fiber straight and improve light coupling into the fiber. No rubber cascade and inner parts of SS-1-UT-A-4 are desired on this side to reduce the tension on the fiber. One S-50-KM from A & N Corporation is welded to the last flange of vacuum chambers in order to hold the fiber holder inside chamber and seal it from the atmosphere.

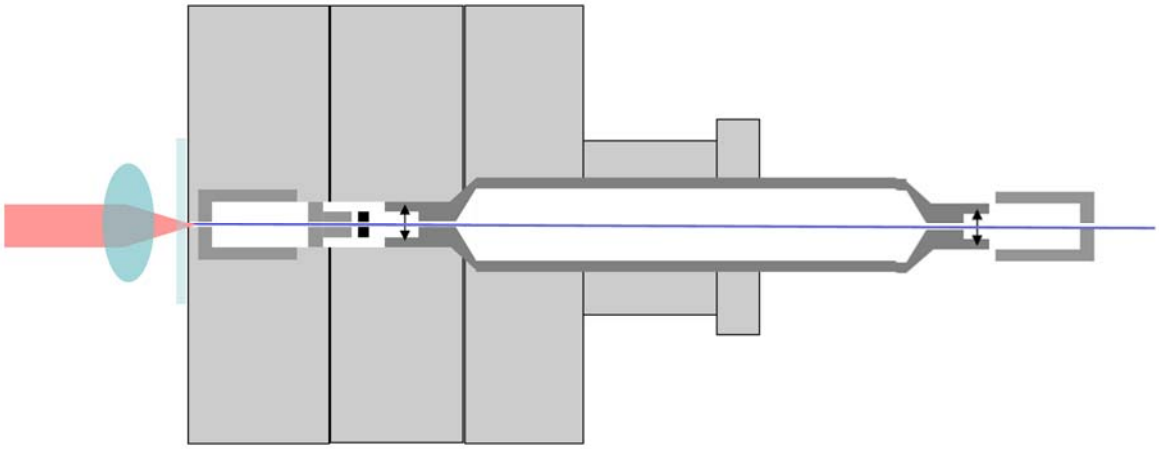

Figure 6.9: Fiber holder design: two ultra-torr vacuum fitting adaptor, SS-1-UT-A-4, from Swagelok were welded to a cylindrical stainless steel tube from both sides. For the side of fiber holder inside vacuum chamber, the fiber slides through a drilled rubber cascade and the SS-1-UT-A-4 inner parts push against the rubber cascade for sealing purpose. The other side of the fiber holder, outside of vacuum chamber, is designed to keep the fiber straight and improve light coupling into the fiber. No rubber cascade and inner parts of SS-1-UT-A-4 are desired on this side to reduce the tension on the fiber. One S-50-KM from A & N Corporation is welded to the last flange of vacuum chambers in order to hold the fiber holder inside chamber and seal it from the atmosphere. Little black double-sided arrows show where the threads are.

6.2.3. Resonator

Precision Photonics Company made a stack of sharp flat dichroic mirrors, whose transmission and reflection at our pump and lasing wavelengths are different. Transmission versus wavelength of a number of these mirrors are shown in Figure 6.10. Producing such mirrors is challenging because the pump and laser wavelengths are very close together, pump wavelength is 1536.7 nm and the lasing wavelength is 1547.4 nm. Among these mirrors, I selected the one with part number SN-46 because it has ~ 99% transmission at pump wavelength, ~1536.7 nm, and ~ 99% reflection at laser wavelength, 1547.4 nm. The transmission and reflection of SN-46 dichroic mirror are shown in Figure 6.11 and Figure 6.12 respectively.

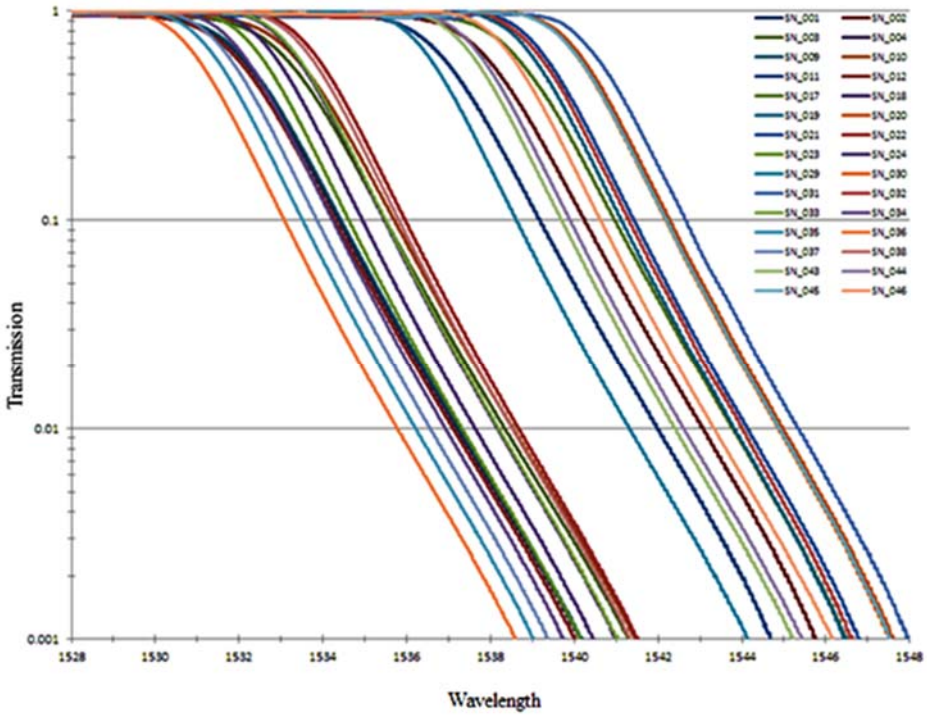

Figure 6.10: Transmission as a function of wavelength for the stack of sharp dichroic mirrors received from Precision Photonics Company in 2012.

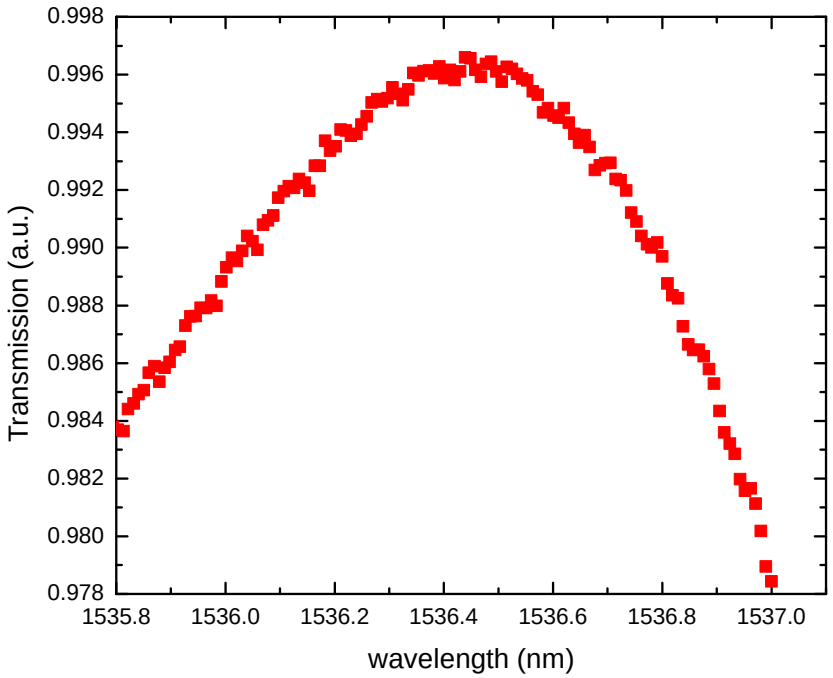

Figure 6.11: Transmission of SN-46 flat dichroic mirror around 1536 nm.

The SN-46 has ~ 99.5% transmission at ~1536.7 nm (pump wavelength) and ~ 99.9% reflection at ~ 1547.4nm (lasing wavelength). So, it is perfect to be used in HCN-filled HOFGLAS resonator.

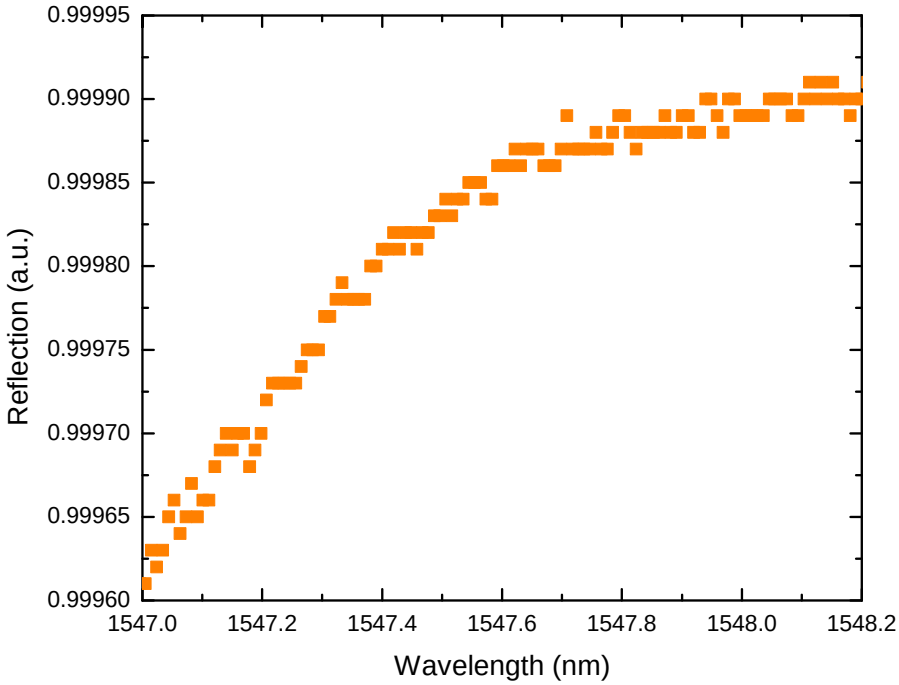

Figure 6.12: Reflection of SN-46 flat dichroic mirror around 1547 nm.

6.3. Stability conditions of HCN-filled HOFGLAS cavity

In this section, calculations for the stability condition of the proposed HCN-filled HOFGLAS is presented. The Ray Transfer Matrix (RTM) or ABCD matrix technique is usually used for optical designing and it is important to lasers community because it acts as a tool for analysis of the stability conditions of laser cavity [92]. Similar ABCD law can be used for Gaussian beams. The typical solution of fundamental TEM_{00} mode for the time-independent propagating optical Gaussian beam is shown in Equation 6.1.

$$\psi_0 = exp\{-j\left[P(z) + \frac{kr^2}{2q(z)}\right]\} \tag{6.1}$$

In Equation 6.1, q (z) can be defined in terms of elements of ABCD matrix as in Equation 6.2. [92].

$$q_z = \frac{Aq_1 + B}{Cq_1 + D} \tag{6.2}$$

Details about equations 6.1 and 6.2 can be find in [92]. So, I will proceed with discussing ABCD matrix role in understanding the stability of a laser cavity and specifically the laser cavity for our HCN-filled HOFGLAS system.

6.2.1. Cavity stability condition

In this section, stability condition for a typical optical resonator is discussed. This optical cavity consists of two mirrors with radius of curvatures R_1 and R_2 that are separated by distance L as shown in Figure 6.13. The ABCD matrix for a roundtrip (starts at mirror 1) inside this cavity given by matrix in Equation 6.3, where $g_i = 1 - \frac{L}{R_i}; i = 1,2$ [98].

$$ABCD = \begin{bmatrix} 2g_1g_2 - 1 & 2Lg_2 \\ [(2g_1g_2 - 1)^2 - 1]\,/2Lg_2 & 2g_1g_2 - 1 \end{bmatrix} \tag{6.3}$$

To see which type of resonator is stable and which is unstable, it is useful to look at the plot of a stability diagram of g_2 versus g_1 in Figure 6.14 [98].

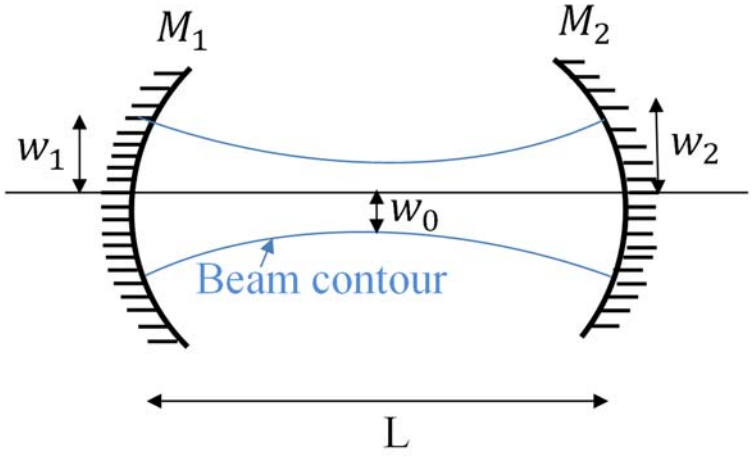

Figure 6.13: A typical cavity with two curved mirrors. M_1 and M_2 are the cavity mirrors and L is the distance between two cavity mirrors. Geometrical optics analysis provides information about the modal content of the output beam [99].

All cavity configurations are unstable unless they correspond to points that are located in the area which is highlighted. This area is enclosed by a branch of the hyperbola and the coordinate axes. The stability condition of a cavity can be expressed as Equation 6.4 [98].

$$-1 < g_1 g_2 < 1 \tag{6.4}$$

If the beam position stays close to the optical axis even after bouncing back and forth many times between the mirrors, the system is stable; if the beam naturally walks off one of the surfaces of the mirrors, it is unstable. Equation 6.4 which describes the stability condition for a laser cavity, can be represented in terms of the elements of ABCD matrix as shown in Equation 6.5.

$$-1 \leq \frac{A+D}{2} \leq 1 \tag{6.5}$$

Equation 6.5 can be written as Equation 6.6.

$$0 \leq \frac{A + D + 2}{4} \leq 1 \tag{6.6}$$

By deriving the ABCD matrix for the cavity configuration and solving Equation 6.6, stability condition for the optical cavity can be found.

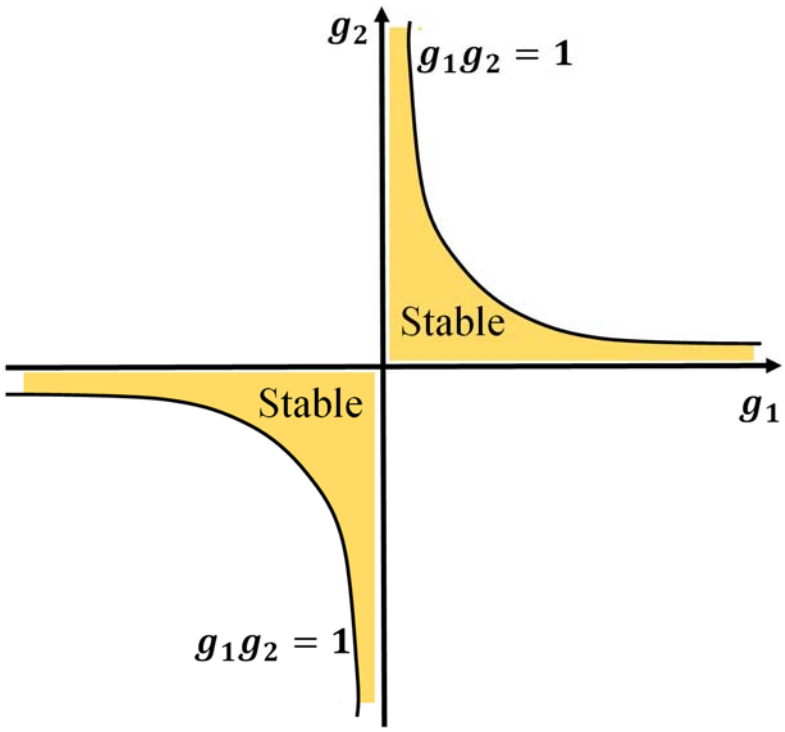

Figure 6.14: Stability diagram of a laser cavity, reproduced from Ref. [98].

6.2.2. HCN-filled HOFGLAS Cavity

The specific configuration for the cavity that we used is our HCN-filled HOFGLAS system is shown in Figure 6.15. It consists of two thin lenses, a HC-PCF, and a resonator.

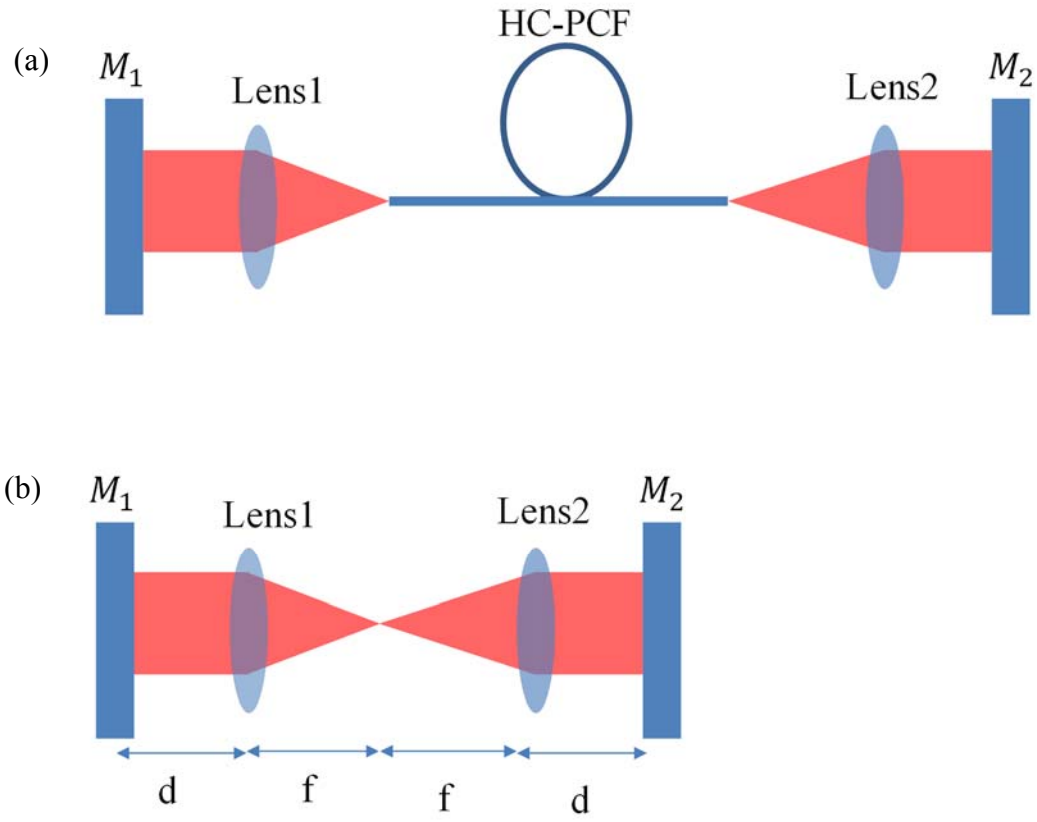

Figure 6.15: (a) HCN-filled HOFGLAS cavity with two intra-cavity thin lenses and the HC-PCF inside the cavity. (b) To write the ABCD matrix we may ignore the HC-PCF.

This cavity is a combination of flat mirror and lens instead of using curved mirrors. The laser beam gets started inside the cavity, it bounces back and forth between the two mirrors and during its propagation inside the cavity, it gets focused and also collimated by two aspheric lenses. To analyze the stability of such a cavity, first of all we may ignore the existence of the HC-PCF in the cavity because is delivers the beam from one point to another point with total internal reflection without affecting on its propagating properties. Then we may multiply the propagation matrixes through the free-space and lenses inside the cavity for one round-trip and we must care about the sequence of multiplication of matrixes together. The one-way ABCD matrix is represented by

Equation 6.7. The beam travel starts from M_1. It encounters a length "d" (free space matrix), reaches a focusing element with focal length "f", propagates for a distance equal to "f" in free-space, reaches an aperture, travels in free-space for distance "f", reaches another identical lens with focal length "f", and finally propagates for a distance "d" to reach the second mirror M_2.

$$ABCD = \begin{bmatrix} 1 & d \\ 0 & 1 \end{bmatrix} \begin{bmatrix} 1 & 0 \\ -\frac{1}{f} & 1 \end{bmatrix} \begin{bmatrix} 1 & f \\ 0 & 1 \end{bmatrix} \begin{bmatrix} 1 & 0 \\ 0 & 1 \end{bmatrix} \begin{bmatrix} 1 & f \\ 0 & 1 \end{bmatrix} \begin{bmatrix} 1 & 0 \\ -\frac{1}{f} & 1 \end{bmatrix} \begin{bmatrix} 1 & d \\ 0 & 1 \end{bmatrix} \tag{6.7}$$

Calculating the right hand side of Equation 6.7 will result in the ABCD matrix for one-way as shown by Equation 6.8.

$$ABCD = \begin{bmatrix} -1 & 2(f-d) \\ 0 & -1 \end{bmatrix} \tag{6.8}$$

It is interesting to know that instead of $\begin{bmatrix} 1 & 0 \\ -\frac{1}{f} & 1 \end{bmatrix} \begin{bmatrix} 1 & f \\ 0 & 1 \end{bmatrix} \begin{bmatrix} 1 & 0 \\ 0 & 1 \end{bmatrix} \begin{bmatrix} 1 & f \\ 0 & 1 \end{bmatrix}$, it is possible to use beam expander transfer matrix which is $\begin{bmatrix} -1 & 2f \\ 0 & -1 \end{bmatrix}$ for two identical focal lengths and if the focal lengths where not identical the transfer matrix becomes $\begin{bmatrix} -\frac{f_2}{f_1} & f_1 + f_2 \\ 0 & -\frac{f_1}{f_2} \end{bmatrix}$.

Now it is possible to compute the transmission matrix of a round-trip beam propagation for the unit cell as shown in Equation 6.9 and Equation 6.10.

$$ABCD = \begin{bmatrix} -1 & 2(f-d) \\ 0 & -1 \end{bmatrix} \begin{bmatrix} -1 & 2(f-d) \\ 0 & -1 \end{bmatrix} \tag{6.9}$$

$$ABCD = \begin{bmatrix} 1 & 4(d-f) \\ 0 & 1 \end{bmatrix} \tag{6.10}$$

Combining Equation 6.10 and Equation 6.6. will result in Equation 6.11.

$$\frac{A+D+2}{4} = 1 \tag{6.11}$$

Equation 6.11 means that for this specific configuration the cavity is always stable if the beam will be perfectly collimated and there will be perfect coupling between beam and fiber end. Analytical calculation for multiplication of matrixes is written in a Python code and has been attached in appendix D. The code also applies stability condition on the ABCD matrix for a roundtrip beam travel in the cavity.

For a beam which is not perfectly collimated or there is not ideal coupling between laser beam and fiber end, the left hand-side of Equation 6.11 will be equal to a complicated function of distances and focal lengths. We may simplify this function using some realistic values for d and f to get a better understanding of the stability condition. ABCD matrix in Equation 6.12 will be obtained for one way travel inside the laser cavity under the assumptions of having identical lenses and symmetry inside the optical cavity, if there won't be a perfect match between fiber end and focal point of the lens, the ABCD matrix will be described as Equation 6.12.

$$ABCD = \begin{bmatrix} 1 & d \\ 0 & 1 \end{bmatrix} \begin{bmatrix} 1 & 0 \\ -\frac{1}{f} & 1 \end{bmatrix} \begin{bmatrix} 1 & a \\ 0 & 1 \end{bmatrix} \begin{bmatrix} 1 & 0 \\ 0 & 1 \end{bmatrix} \begin{bmatrix} 1 & a \\ 0 & 1 \end{bmatrix} \begin{bmatrix} 1 & 0 \\ -\frac{1}{f} & 1 \end{bmatrix} \begin{bmatrix} 1 & d \\ 0 & 1 \end{bmatrix} \tag{6.12}$$

Where a is the distance between the focal point of one of the lenses and fiber end. ABCD matrix for a roundtrip beam propagation inside the cavity can be calculated using Equation 6.12.

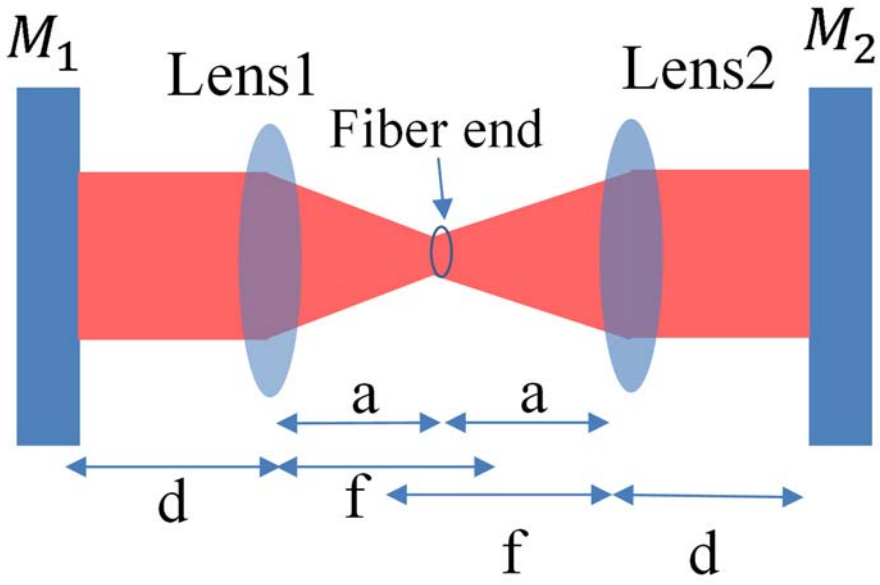

Figure 6.16: HCN-filled HOFGLAS cavity with two intra-cavity thin lenses and the HC-PCF inside the cavity. To write the ABCD matrix, the HC-PCF is being ignored. The picture is for not perfectly collimated beam.

Using the Python code for values of 15 mm focal length, and d equal to 5 mm, the stability condition can be simplified. From the results, it is clear that when the value of a is very close to f the cavity is stable (less than ~1 mm different). The code has also been checked for different values of d. The cavity is always stable for the perfectly collimated beam. But, the imperfect coupling of the beam into the fiber make the cavity unstable. It is interesting to know that in this case, distance between mirror and lens matters. For using a lens with focal length 15 mm d should not be more than 30 mm to have a stable cavity with slightly imperfect coupling. Experimentally, we should be very creative to put lens and cavity mirror that close together.

6.3. Recoupling measurement

Prior to running the HCN-filled HOFGLAS setup, a recoupling measurement was performed and the setup for this measurement is shown in Figure 6.17. Commercial continuous wave 1.5 μm laser which is tunable diode laser from Santec Company is being fiber-coupled to an optical circulator and the wavelength is being set on ~1547nm (HCN HOFGLAS lasing wavelength). An optical circulator is a fiber optic device that may separate optical beams that propagate in opposite directions inside an optical fiber. Our optical circulator has 3 ports and it is designed in a way that beam entering any port exits from the next. Optical circulator is a non-reciprocal optics that means properties of beam changes as it passes through the device in the opposite direction. This may happen by breaking the symmetry for example using a magnetic field or Faraday rotator, which is a polarization rotator based on the Faraday effect. The circulator I used was very lossy itself and I took into account the amount of its loss for propagations from at port 1 to port 2 and from port 2 to port 3 for calculating recoupling efficiency, the amount of loss in each transmission is ~ 4.8 dB.

Laser is connected to port 1 of circulator and the exit beam at port two passes through a splice of the SMF port to a 10 μm PBG fiber. There is an estimated splice loss for the amount of 2.8 dB. Then the beam is collimated in free-space by an 15 mm focal length aspheric lens the dichroic mirror is being used to recouple the beam back into the circulator. The beam is detected and optimized at port 3 of the circulator using a fiber-coupled large area photo detector. Recoupling efficiency of 98% is obtained. The focal length of the lens plays an important role in the recoupling efficiency. The lens should match the beam diameter in free space with the fiber numeric aperture as well as coupling more of the fundamental mode into the hollow core fiber using Equation 5.5.

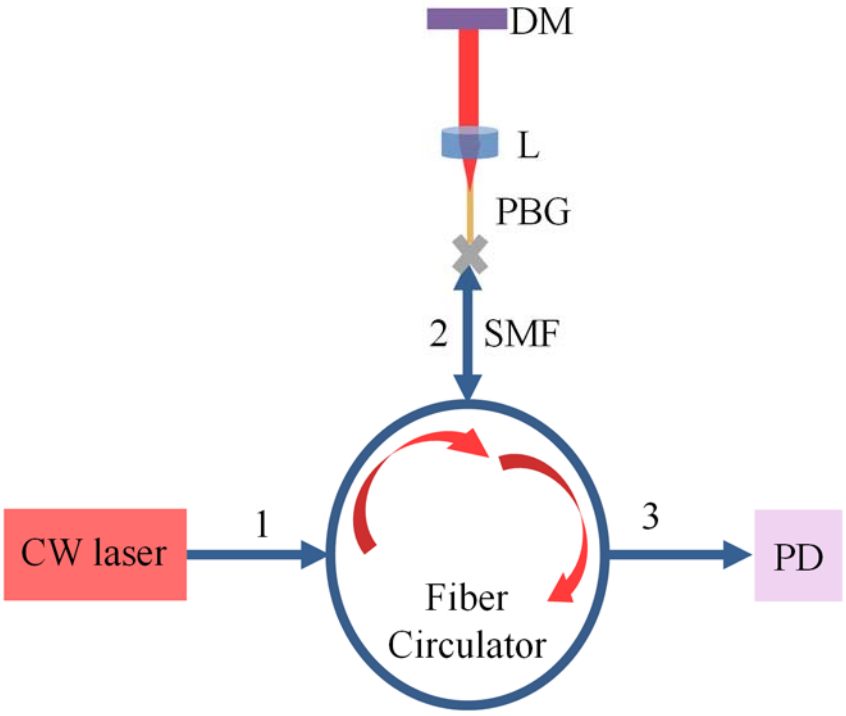

Figure 6.17: Recoupling measurement setup. An optical fiber-coupled circulator with three SMF ports is used. CW laser is connected to port 1. SMF fiber in port 2 is spliced to a PBG fiber and beam leaves PBG fiber to free-space through a 15 mm focal length aspheric lens. The collimated beam gets reflected at the Dichroic Mirror and gets recoupled into the circulator and leaves the circulator through port 3 and gets detected by a fiber-coupled large area Photo Detector.

6.4. Challenges in HCN-filled HOFGLAS operation

Alignment of the setup has been a big issue because of interference of the forward and backward beams inside the laser cavity. We experimentally understood that tapping continuously on an optics mount may help in observing the interference pattern on the scope and working toward optimizing the recoupled beam. Unfortunately, no lasing was observed from this laser system so far. Currently, Manasa Thirugnanasambandam, postdoc in our research group, in continuing the work on this laser setup and she has even faced some new challenges as it is described in the future work of this laser system in the next chapter.

Chapter 7 - Future work

7.1. Future work for acetylene-filled HOFGLAS

7.1.1. Further power-scaling

As shown in this dissertation, OPA pumped acetylene-filled HOFGLAS is exhibiting novel behaviors such as excellent beam quality at highest power and efficiency independent of pressure. All these properties are encouraging for further power scaling. One way to scale the laser system to higher power is to access to higher power pump. Our pump is a homebuilt one stage OPA with a PPLN crystal. Kushan Weerasinghe, graduate student in our research group, is working toward building a two stage OPA by holding the current OPA as the first stage and using a KTP crystal in the second stage.

7.1.2. Laser modeling

Phenomenological scaling of saturation power and efficiency with pressure that we observe motivate further development of detailed numerical models of the laser for deeper insight into these effects. These lasers are complicated, and that to explain them requires an accurate numerical model. One of the most important considerations in the laser modeling should be pump saturation. We are in a regime of high pump saturation, meaning the amount of power absorbed by the gas varies along the length of the fiber, and with pressure, in a highly nonlinear way.

7.2. Future work for HCN-filled HOFGLAS

7.2.1. Thermal damage of the fiber at higher power

As mentioned at the end of chapter 6, alignment of the setup due to interference of forward and backward beams inside cavity is still a big issue and should be solved. Manasa

Thirugnanasambandam, postdoc in our research group, in continuing the work on this laser setup and she has faced some additional challenges as described here.

100 mW of pump power was used for alignment of the HCN-filled HOFGLAS setup initially. The pump power was increased in steps to check for power dependent coupling. At ~2W of pump power (EDFA seeded at 1537nm), the PBG fiber, mounted in the typical vacuum-compatible fiber holders, was damaged as shown in Figure 7.1 and the pump coupling into PBG fiber was power dependent as shown in Figure 7.2.

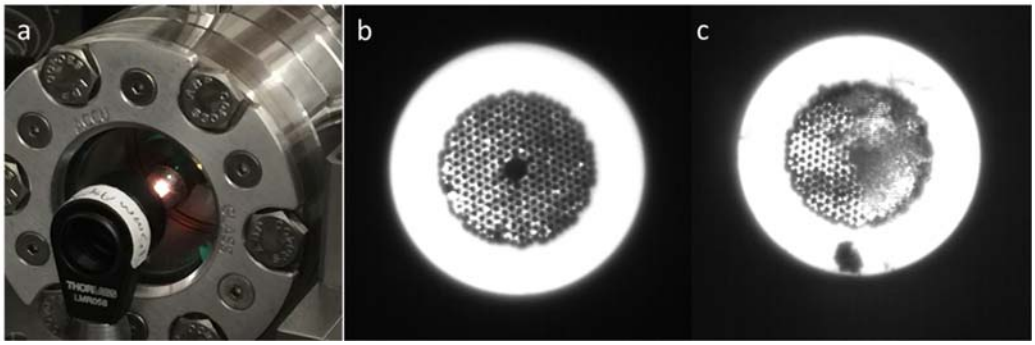

Figure 7.1: a_0The burning end of HC-PCF when 2W of pump power at 1532 nm was coupled into the fiber. The ends of the HC-PCF as seen under a camera b_0 before and c0 after damage. The pictures are taken by Manasa Thirugnanasambandam.

Figure 7.1 shows the burning end of a 10 μm diameter PBG at ~2 W of pump at 1537 nm. The cleaved ends of the fiber before and after damage are compared in Figure 7.1 as well. A series of test experiments were performed to find the cause of the damage. The damages are attributed to the minor imperfections in the mode matching between the pump laser mode and the fundamental mode of the fiber along with the pump power lost due to free-space coupling using aspheric lenses causes heating of the stainless steel vacuum-compatible parts of typical fiber holders used in HOFGLAS systems so far. This results in irreversible damage to the ends of the HC-PCF which

was observed at ~2W of pump power. The damage to the fiber ends could be avoided by using heat shields or cooling the fiber holders.

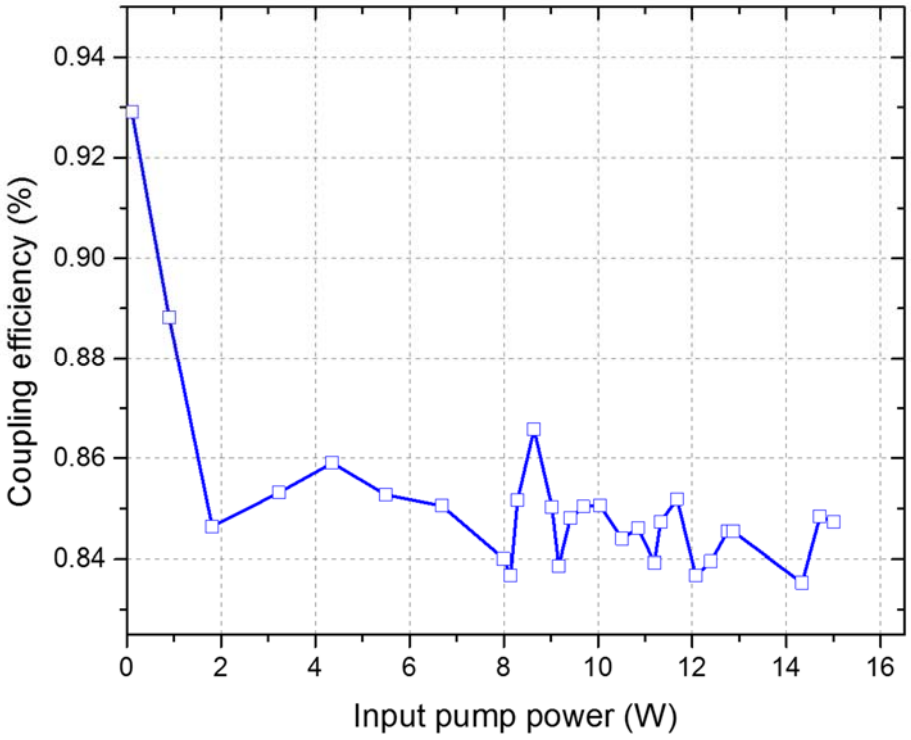

Figure 7.2: The pump coupling efficiency as a function of pump power incident on the fiber when a heat shield was used in front of the fiber holder.

A test experiment was done in free-space by heat shielding the fiber holder using an iris and it was possible to couple pump powers upto ~15W into the HC-PCF without any damage. Efforts are underway to redesign the vacuum compatible fiber holders that are typically used in the HOFGLAS setup.

7.2.2. Other pumping configurations

Alternate pumping configurations can be considered as well. New pump configuration should help us win on the pump intensity given our limits on the input pump power that can be coupled into the fiber based on damage thresholds. Bidirectional pumping configuration is an option. In bidirectional pumping configuration, pump power is coupled from both ends of the fiber

therefore the overall pump power increases. We may also work on the possibility of quasi-continuous wave pumping, which will help reduce the average power without compromising on the pump intensities required for population inversion and lasing. Consequently, it may solve the problem of the thermal damage on the fiber.

List of publications

PEER-REVIEWED PUBLICATIONS

- "Near diffraction-limited performance of an OPA pumped acetylene-filled hollow-core fiber laser in the mid-IR", N. Dadashzadeh, M. Thirugnanasambandam, K. Weerasinghe, B. Debord, M. Chafer, F. Gérôme, F. Benabid, B. R. Washburn, and K. L. Corwin, Optics Express, vol. 25, Issue 12, pages 13351-13358 (2017).
- "Near-Gaussian Spatial Mode from a Mid-IR Acetylene-filled Hollow-Core Fiber Laser", N. Dadashzadeh, M. Thirugnanasambandam, K. Weerasinghe, B. Debord, M. Chafer, F. Gérôme, F. Benabid, B. R. Washburn, and K. L. Corwin, Frontiers in Optics/ Laser Science Conference (2016).
- "Power-scaling a Mid-IR OPA-pumped Acetylene-filled Hollow-Core Photonic Crystal Fiber Laser", N. Dadashzadeh, M. Thirugnanasambandam, K. Weerasinghe, B. Debord, M. Chafer, F. Gérôme, F. Benabid, B. R. Washburn, and K. L. Corwin, CLEO, STh4O.1 (2016).
- "Hollow-core Optical Fiber Gas Lasers (HOFGLAS): a review [Invited]", A. V. Vasudevan Nampoothiri, A. M. Jones, C. Fourcade-Dutin, C. Mao, N. Dadashzadeh, B. Baumgart, Y.Y. Wang, M. Alharbi, T. Bradley, N. Campbell, Fetah Benabid, B. R. Washburn, K. L. Corwin, and W. Rudolph, Optical Materials Express, 2, 948 (2012).

NON-PEER-REVIEWED PUBLICATIONS

- "Near-Gaussian spatial mode from an optically pumped acetylene-filled hollow-core fiber laser in the mid- IR", N. Dadashzadeh, M. Thirugnanasambandam, K. Weerasinghe, B. Debord, M. Chafer, F. Gérôme, F. Benabid, B. R. Washburn, and K. L. Corwin, KS-NE

Symposium on Imaging and Controlling Ultrafast Dynamics of Atoms, Molecules, and Nanostructures, poster presentation, (2017).

- "Towards realizing a hollow core optical fiber gas laser with small quantum defect", M. P. Thirugnanasambandam, **N. Dadashzadeh**, B. R. Washburn, and K. L. Corwin, ICTP Winter College on Optics, Trieste, Italy, Poster presentation, (February 2016).
- "Mode Profile of a Mid-IR Gas-filled Hollow-Core Photonic Crystal Fiber Laser", **N. Dadashzadeh**, K. Weerasinghe, A. Jones, B. Debord, F. Gerome, F. Benabid, B. Washburn, and K. Corwin, Optical Society of America, Frontiers in Optics/ Laser Science Conference, LTh4I. 4 (2015).

Appendix A - Tips for loss measurements with monochromator

a) Appropriate ND filters should be used to keep the signal amplitude observed from Photo Detector (PVI-2TE Series, Boston Electronics) between 10 and 20 mV.

b) Always should park motor, that controls the grating, at home position using the HyperTerminal program at the end of the day. In this case, if there will be a power outage in the lab, we will be still confident about grating position in the following day. The number of steps per nanometer for the monochromator can be checked by transmitting 1.5 μm laser beam through the monochromator and finding the motor positions related to the first and second order diffraction positions and then calculate the steps per nanometer.

$$m = \frac{41250 - 4650}{1533} = 23.87$$

Where m is the number of steps per nanometer. If accidentally any unreasonable number is entered in the HyperTerminal, disconnect a white wire that is attached to the motor chip. In this way, the HyperTerminal runs the program; however, the grating position does not actually move. Then the hyperterminal can be sent to the previous position again while the wire is still disconnected and then recalibration for the monochromator can be performed at this point.

Appendix B –Fractional transmission through acetylene-filled fiber

```
"""
By Neda Dadashzadeh and Brian Washburn

This is a Python code.
Calculates FWHM of voigt abosrption profile for acetylene at certain pressure.
absorption(v)=S*(p/(kb*T))*Voigt(v) where S is line strength (see references
2 & 4). NIST SRM data of 10% transmission through a 5 cm
acetylene cell of 50 torr in pressure was used to calculate line strength.

References
[1] Swann et al., Applied Optics vol 17, (2000)
[2] NIST special publication 260-133, 2001 edition
[3] Jun Ye Ph.D. thesis
[4] Hennigsen et al, Opt. Express 13 (2005)
[5] Olivero, J. J.; R. L. Longbothum (February 1977).
"Empirical fits to the Voigt line width: A brief review".


All units in meters, kilograms, seconds, except pressure in units of torr

"""
import numpy as np
from matplotlib import pyplot as plt
from lmfit.models import VoigtModel

plt.close('all')
print ' '

# universal constants
kb = 1.3806503*1e-23  # J/K, Boltzmann constant
amu=1.66054e-27       # atomic mass unit in kg
c = 2.99792458*1e8    # m/s, speed of light
NA= 6.022140857*10**23 #Avogadro's number

#------------------------------------------------------------------------
# Define functions

# Lorentian gamma as a function of pressure (in torr)
def gL(p):
    a=11.479e6  # 11.4 MHz per torr, from Ref [1], Table 4
    return (a*p+58.529e6)/2 # 58.529MHz comes from intercept of linear fit to data from
Ref[1]
```

```
# Gaussian FWHM as a function of temperature (in Kelvin), and frequency
def FWHMG(T,f0):
    # m is acetylene molecular [mass/amu] which is 26 for acetylene
    #Gaussian fwhm = f0*[2*sqrt(2)*sqrt(NA*kb)/c]*sqrt(T/NA*M) where NA*M=m
    # 2*sqrt(2)*sqrt(NA*kb)/c=7.16*10**(-7)
    return f0*7.16*10**(-7)*np.sqrt(T/26)

#to go from Gaussian fwhm to Gaussian sigma use the following ratio
ra=2*np.sqrt(2*np.log(2))


# Voigt absorption profile of acetylene
def av(p,T,f):
    # determine frequency dependent absorption based on a Voigt profile
    # Functional form: absorption(v)=S*(p/(kb*T))*Voigt(v)  (see Ref. [4])
    # use nist data Ref[2] to determine line strength S
    # nist measured 0.1 transmission thru 5 cm cell of acetylene at 50 torr

    f0=f[f.size/2]     # center frequency in Hz

    mod = VoigtModel()      # create model class
    ra=2*np.sqrt(2*np.log(2)) #to go from Gaussian fwhm to Gaussian sigma

    # use nist data to compute the line strength S
    p_nist=50.0         # nist pressure in torr
    T_nist=298.0        # nist temperature in Kelvin
    a_nist=-(1/0.05)*np.log(0.1) # compute gas absorption (in 1/m) from Ref[2]
    fwhmG_nist=FWHMG(T_nist,f0) # Gaussian FWHM of nist data
    sig_nist=fwhmG_nist/ra #Gaussian sigma of nist data
    gam_nist=gL(p_nist) # Lorenztian gamma of nist data

    # create voigt based nist data to compute S
    av_nist=mod.eval(x=f, amplitude=1, center=f0, sigma=sig_nist, gamma=gam_nist)
    # compute line strength
    S=a_nist/(((p_nist*133.32)/(kb*T_nist))*av_nist[(f==f0)][0])

    # create absorption as a function of pressure and temperature
    fwhmG=FWHMG(T,f0)      # gaussian FWHM at given temperature
    sig=fwhmG/ra
    gam=gL(p)           # lorenztian gamma at given pressure
    # evaluate model
    y=mod.eval(x=f, amplitude=1, center=f0, sigma=sig, gamma=gam)
    return S*(p*133.32)/(kb*T)*y

def voigt_fwhm(gfwhm,lfwhm):
```

```
        # use approximate express to relate voigt fwhm to gaussian and lorenzian fwhm
        # expression from [5]
            return 0.5346*lfwhm + np.sqrt(0.2166*lfwhm**2 + gfwhm**2)

        def compute_fwhm(x,y):
        # compute the fwhm of a function y(x)
            ymax=max(y)       # peak absorption at line center
            x0=y.argmax(axis=0)
            y=y/ymax
            index1 = 0
            index2 = 0
            for i in range(len(y)):
                if y[i] >= 0.5 and index1 == 0:
                    if abs(y[i] - 0.5) > abs(y[i-1] - 0.5):
                        index1 = i -1
                    else:
                        index1 = i
                elif y[i] <= 0.5 and index1 > 0:
                    if abs(y[i] - 0.5) > abs(y[i-1] - 0.5):
                        index2 = i - 1
                    else:
                        index2 = i
                    break
            bx1 = x[index1]
            bx2 = x[index2]
            return abs(bx1-bx2)

        #------------------------------------------------------------------------

        # system parameters
        l0=1532.83042e-9          # center wavelength in m
        f0=c/l0               # center frequency in Hz
        T=298.0               # temperature in Kelvin
        pressure_set=np.array([     10,     50.254154,  222.768414, 495.04092,  0.93])              #
pressure in torr (10 torr)
        fiber_length_set=np.array([ 10.9,   0.05,       0.05,       0.05,       0.8])
        p=10
        # define frequency array for absorption feature
        numf=1e6            # number of frequency points
        ran=1.0e11            # frequency range about center frequency
        df=ran/numf
        f=(np.linspace(1,numf,numf)-numf/2-1)*df+f0


        fwhmG=FWHMG(T,f0)      # gaussian FWHM at given temperature
        gam=gL(p)          # lorenztian gamma at given pressure
```

```
ra=2*np.sqrt(2*np.log(2)) #to go from Gaussian fwhm to Gaussian sigma
sig=fwhmG/ra        # gaussian sigma at given temperature
fwhmL=gam*2           # lorenztian fwhm at given pressure

def transmission(pressure, fiber_length):
    ab=av(pressure,T,f)          # Voigt absorption as a function of frequency
    # Using the value of half of the maximum (b), I could find two related
    # frequencies and then calculate fwhm:
    I0=0.376 # input power is linearly dependent to initial voltage signal
    return I0*np.exp((-1)*ab*fiber_length)

voltage_signal_set = np.zeros(shape=(6,1000000))
for i in range(len(pressure_set)): #len(pressure_set)
    voltage_signal = transmission(pressure_set[i],fiber_length_set[i])
    #print 'voltage_signal is %0.3f' %voltage_signal
    voltage_signal_set[i] = voltage_signal

ab=av(p,T,f)          # Voigt absorption as a function of frequency

# Using the value of half of the maximum (b), I could find two related
# frequencies and then calculate fwhm:

ag=ab[(f==f0)][0]      # peak absorption at line center
b=ag/2
index1 = 0
index2 = 0
for i in range(len(ab)):
    if ab[i] >= b and index1 == 0:
        if abs(ab[i] - b) > abs(ab[i-1] - b):
            index1 = i -1
        else:
            index1 = i
    elif ab[i] <= b and index1 > 0:
        if abs(ab[i] - b) > abs(ab[i-1] - b):
            index2 = i - 1
        else:
            index2 = i
        break

bx1 = f[index1]
bx2 = f[index2]
fwhmv=abs(bx1-bx2)
I0=0.376 # input power is linearly dependent to initial voltage signal

# compute voigt FWHM from approximate equation
fwhmVapprox = voigt_fwhm(fwhmG,fwhmL) # compute from approximate equation
```

```
        #-------------------------------------------------------------------------
        print
'_____________________________________________________________________________'
        """print '# space steps: %d' % numz"""
        print ' '
        print 'Pressure = %0.3f torr' % p
        print 'Frequency resolution of %0.5f MHz' %(df/1e6)
        print ' '
        print 'Gaussian FWHM = %0.3f MHz' % (fwhmG/1e6)
        print 'Gaussian sigma = %0.3f MHz' % (sig/1e6)
        print 'Lorentzian gamma = %0.3f MHz' % (gam/1e6)
        print 'Lorentzian FWHM = %0.3f MHz' % (fwhmL/1e6)
        print ' '
        print 'voigt FWHM= %0.3f MHz' % (fwhmv/1e6)
        print 'voigt FWHM= %0.3f MHz from approximate equation' % (fwhmVapprox/1e6)
        print ' '
        # to be able to plot experiment data and theory data on the same graph have to go from absolute frequency to the relative frequency
        #to go from absolute frequency to relative frequency that corresponds to data, I shiftet the frequency with respect to seperation of two peaks of experimental data and theory
        # number 195579966241375.28 Hz comes from the shift between experiment data dip and theory optical power dip
        def f1(f):
           return [(x - f0) /1e6 for x in f]
        relativefrequency= f1(f)

        print
'_____________________________________________________________________________'


        # plot data
        """plt.figure(1)
        plt.plot(relativefrequency,ab)
        #plt.xlim((f0-1e9)/1e12,(f0+1e9)/1e12)
        plt.xlim(-2000,4000)
        plt.grid(True)"""

        #filename='experiment data vs freq.txt'
        #directory='R:\\LUMOS (Corwin)\\Researchers\\Neda Dadashzadeh\\'
        #pathname=  directory + filename

        #   Set each variable: (time,Ramp,cell,ring,ref) equal to a column of the data
        #frequency, transmission = np.loadtxt(pathname, delimiter='\t', usecols=(0,1), unpack=True)
```

```
plt.figure(2)
plt.plot(relativefrequency,voltage_signal_set[0],'b',label='Neda Calc.,10 t,10.9m')
plt.plot(relativefrequency, voltage_signal_set[1],'red', label='Swann,50.254 t,0.05m')
plt.plot(relativefrequency, voltage_signal_set[2],'g', label='Swann,222.768 t,0.05m ')
plt.plot(relativefrequency, voltage_signal_set[3],'y', label='Swann,495.041 t,0.05m')
plt.plot(relativefrequency, voltage_signal_set[4],'black', label='Rajesh,0.93 t, 0.8m')
plt.plot(relativefrequency, voltage_signal_set[5],'orange', label='Nist,50 torr, 0.05m')
plt.xlabel('relative frequency  (MHz)')
plt.ylabel('Voltage signal (V)')
#plt.ylabel('Voltage signal2 (V)')
#plt.ylabel('Voltage signal3 (V)')
#plt.ylabel('Voltage signal4 (V)')
#plt.ylabel('Voltage signal5 (V)')
#plt.ylabel('Voltage signal6 (V)')
#plt.xlim((f0-1e9)/1e12,(f0+1e9)/1e12)
plt.xlim(-20000,20000)
plt.grid(True)
plt.legend(bbox_to_anchor=(1.05, 1), loc=9, borderaxespad=9.)
```

Appendix C – Beam width calculation / Matlab code

```
%Written by Kushan and Neda.
% This is a Matlab code.
% The code calculates the beam waist of a laser beam using the slit scan data
% beam waist for ideal slit w = 4*<x^2>
% but for realistic slit w= 4* (<x^2> - f /12); where f is the slit width
% <x^2> = ( intergration (I(x,y)*x^2)dx )/ integration (I(x,y) dx) this
% defines for distribution where <x> =0 ;
% therefor we need to find <x> of our data set and take that in to account
% for our calculation


% include your data in an excell file. Both mathlab file and excell file
% should be in same folder otherwise you have to specify the path for
% excell file
% use second columon to include your position (x value) and 3rd column for
% power values


% if you are manually enter the data please use line 29 and 34 to enter x
% values and powers respectivly. If you do so, lines 24,25,27and 28 should be
commented


%_____________________________________________________________________________
_____________%

clc;
clear;
close all;

% choose data path.

filename= 'R:\LUMOS (Corwin)\Researchers\Kushan Weerasinghe\M^2 data\M^2 5-9-
2016\point12.xlsx' % if excell file in a different folder use this line

%filename= 'test16.xlsx' ;% include the excell file name here

A=xlsread(filename);

x=A(:,2); % position
p=A(:,3); % power

%x=[10.7    10.8    10.9    11  11.1    11.2    11.3    11.4    11.5    11.6
11.7    11.8    11.9    12  12.1    12.2    12.3    12.4    13];
%x=[7:.05:5.6];  % enter your micro meter readings here

y=zeros(1,length(x)); % for store relative positions
y(1)=0; % setting staring point as zero

sw=.02; % slit width in mm
```

```
%p=[5   13.5    26.5    45.4    62.2    77.2    91.2    98.8    102.4   98
92.8    84.4    73.6    57.6    45.6    30.8    20.8    13.2    7.8]; % enter
your volatges here

for i=1:length(x)-1
    y(i+1)=x(1)-x(i+1); %geting the position relatively to the starting point
end
%Calculating mean of postion <x>
meanx=0;
inte1=0;
% meanx= integration (I(x,y)*x)/ integration (I(x,y))
for i=1:length(x)
    px(i)=((p(i)/1.6)*(y(i)))*10^-3 ;

end
for i=1:length(x)

    pt(i)=(p(i)/1.6)*10^-3;
end
% using trapizoidal method to calculate integraion
for j=1:length(x)-1
meanx=meanx+(.5*(px(j)+px(j+1))*(x(j+1)-x(j)));
inte1=inte1+(.5*(pt(j)+pt(j+1))*(x(j+1)-x(j)));
end
meanx=meanx/inte1;
%_____________________________________________%
%calculating second moment <x^2>

for i=1:length(x)
  pxx(i)=((p(i)/1.6)*(y(i)-meanx )^2)*10^-3 ;

end
pmax=max(pt);
pmax2=pmax/(exp(1));
for k=1:length(x)
    w(k)=pmax2; % *(1/e position)
end
% plotting results to see whether these make sense or not.

subplot(2,1,1)
,plot(x,pt,'*r',x,w,'b'),xlabel('position(mm)'),ylabel('voltage(mV)'),legend(
'experimental data','1/e line')
subplot(2,1,2),plot(y,pxx,'*')
inte=0;
inte1=0;
% using trapizoidal method to calculate integraion
for j=1:length(x)-1
inte=inte+(.5*(pxx(j)+pxx(j+1))*(x(j+1)-x(j)));
inte1=inte1+(.5*(pt(j)+pt(j+1))*(x(j+1)-x(j)));
end
x2=inte/inte1; %second moment
w=sqrt(4*x2);
ws=sqrt((x2-(sw^2/12))*4);%beam waist (1/e, HWHM)
figure(2)
```

```
plot(x,pt,'*r')
xlabel('position(mm)')
title('Beam profile')
ylabel('voltage(V)')
formatSpec='beam waist is %0.4f mm (HWHM at 1/e)';
fprintf(formatSpec,w)
formatSpec='beam waist with slit correction is %0.4f mm (HWHM at 1/e)';
fprintf(formatSpec,ws)
```

Appendix D – ABCD matrix calculation and cavity stability condition, Python code

```
"""
@author: Neda Dadashzadeh

Created on Mon Jul 17 19:12:13 2017

This code, defines ABCD transfer matrixes and multiplies them together
for one way travel in a defined laser cavity and then it calculates ABCD matrix
for a roundtrip travel in the laser cavity.  The stability condition is then
investigated: 0<(A+D+2)/4<1.
This is an analytical solution.

"""

import sympy as sp
from sympy import *
import numpy as np
from matplotlib import pyplot as plt


#Define matrix elements

f = sp.IndexedBase('f')

w, x, y, z = sp.symbols('w x y z', cls=sp.Idx)


f1_new = -1/f[w]
f2_new = -1/f[x]
# f_bazar = -(f[z]+f[y])/(f[y]+f[z])
b = sp.Symbol('b')
a = sp.Symbol('a')
d = sp.Symbol('d')
e = sp.Symbol('e')

# define matrixes

A = sp.Matrix([[1,5],[0,1]])
B = sp.Matrix([[1,0],[(-1/15),1]])
C = sp.Matrix([[1,a],[0,1]])
#D = sp.Matrix([[1,0],[f_bazar,1]])
E = sp.Matrix([[1,a],[0,1]])
F = sp.Matrix([[1,0],[(-1/15),1]])
```

```
G = sp.Matrix([[1,5],[0,1]])

# multiply matrixes for one way trip

ZZ = (A*(B*(C*(E*(F*G)))))

# calculate roundtrip travel for symmetric cavity

final_matrix = ZZ * ZZ

# simplify the solution

simple = sp.simplify(final_matrix)

# Stability condition

result= (2+simple[0,0] + simple[1,1])/4

# stability condition should be between zero and 1.


N = 1000

x = np.linspace(0, 15, N)

def g(x):
  return 64*x**2 - 144*x + 81

plt.plot(x,g(x))

gg=g(x)

# figure out for what x values stability condition is between zero to 1.
index1 = 0
index2 = 0

for i in range(len(gg)):
   if gg[i] >= 0 and index1 == 0:
      if  1 >= abs(gg[i]):
         index1 = i


xx1 = x[index1]
```

References

1. Hecht, J., *Looking back/Looking forward: Gas lasers: Durable survivors evolve new forms.* LaserFocusWorld, 2015.

2. Dadashzadeh, N., et al. *Power-scaling a mid-IR OPA-pumped acetylene-filled hollow-core photonic crystal fiber laser*. in *Lasers and Electro-Optics (CLEO), 2016 Conference on*. 2016. IEEE.

3. Wang, Z., et al., *Efficient diode-pumped mid-infrared emission from acetylene-filled hollow-core fiber.* Optics express, 2014. **22**(18): p. 21872-21878.

4. Hassan, M.R.A., et al., *Cavity-based mid-IR fiber gas laser pumped by a diode laser.* Optica, 2016. **3**(3): p. 218-221.

5. Nampoothiri, A., et al., *CW hollow-core optically pumped I 2 fiber gas laser.* Optics letters, 2015. **40**(4): p. 605-608.

6. Nampoothiri, A.V., et al., *Hollow-core optical fiber gas lasers (HOFGLAS): a review.* Optical Materials Express, 2012. **2**(7): p. 948-961.

7. Jones, A., et al. *Characterization of mid-infrared emissions from C2H2, CO, CO2, and HCN-filled hollow fiber lasers*. in *Proc. SPIE*. 2012.

8. Jones, A.M., et al., *Mid-infrared gas filled photonic crystal fiber laser based on population inversion.* Optics Express, 2011. **19**(3): p. 2309-2316.

9. Willet, C.S., *Introduction to gas lasers.* Population Inversion Mechanisms (Pergamon Press, Oxford, 1974), 1974.

10. Bridges, W.B., *Laser oscillation in singly ionized argon in the visible spectrum.* Applied Physics Letters, 1964. **4**(7): p. 128-130.

11. Krupke, W.F., *Diode pumped alkali lasers (DPALs)—A review (rev1).* Progress in Quantum Electronics, 2012. **36**(1): p. 4-28.

12. Zhdanov, B., T. Ehrenreich, and R. Knize, *Highly efficient optically pumped cesium vapor laser.* Optics Communications, 2006. **260**(2): p. 696-698.

13. Krupke, W.F., et al., *Resonance transition 795-nm rubidium laser.* Optics Letters, 2003. **28**(23): p. 2336-2338.

14. Ehrenreich, T., et al. *Diode pumped cesium laser*. in *Conference on Lasers and Electro-Optics*. 2005. Optical Society of America.

15. Ehrenreich, T., et al., *Diode pumped caesium laser.* Electronics Letters, 2005. **41**(7): p. 415-416.

16. Schlossberg, H. and H. Fetterman, *Optically pumped vibrational transition laser in OCS.* Applied Physics Letters, 1975. **26**(6): p. 316-318.

17. Chang, T. and O. Wood, *An optically pumped CO 2 laser.* IEEE Journal of Quantum Electronics, 1972. **8**(6): p. 598-598.

18. Chang, T. and T. Bridges, *Laser action at 452, 496, and 541 μm in optically pumped CH3F.* Optics Communications, 1970. **1**(9): p. 423-426.

19. Nampoothiri, A., et al., *Molecular C 2 H 2 and HCN lasers pumped by an optical parametric oscillator in the 1.5-μm band.* Optics express, 2010. **18**(3): p. 1946-1951.

20. Miller, H.C., D.T. Radzykewycz, and G. Hager, *An optically pumped mid-infrared HBr laser.* IEEE journal of quantum electronics, 1994. **30**(10): p. 2395-2400.

21. McCord, J.E., et al., *Frequency-tunable optically pumped carbon monoxide laser.* IEEE journal of quantum electronics, 2000. **36**(9): p. 1041-1052.

22. McCord, J.E., et al., *Experimental investigation of an optically pumped mid-infrared carbon monoxide laser.* IEEE journal of quantum electronics, 1999. **35**(11): p. 1602-1612.

23. Kletecka, C., et al., *Cascade lasing of molecular HBr in the four micron region pumped by a Nd: YAG laser.* IEEE journal of quantum electronics, 2004. **40**(10): p. 1471-1477.

24. Nampoothiri, V., et al. *Mid-IR laser emission from a C2H2 gas filled hollow core photonic crystal fiber*. in *Proceedings of SPIE-The International Society for Optical Engineering*. 2010. University of Bath.

25. Dadashzadeh, N., et al., *Near diffraction-limited performance of an OPA pumped acetylene-filled hollow-core fiber laser in the mid-IR.* Optics Express, 2017. **25**(12): p. 13351-13358.

26. Moulton, P.F., et al., *Tm-doped fiber lasers: fundamentals and power scaling.* IEEE Journal of Selected Topics in Quantum Electronics, 2009. **15**(1): p. 85-92.

27. Jackson, S.D., *Cross relaxation and energy transfer upconversion processes relevant to the functioning of 2 μm Tm 3+-doped silica fibre lasers.* Optics Communications, 2004. **230**(1): p. 197-203.

28. Jackson, S.D., *High-power and highly efficient diode-cladding-pumped holmium-doped fluoride fiber laser operating at 2.94 μm.* Optics letters, 2009. **34**(15): p. 2327-2329.

29. Tokita, S., et al., *Stable 10 W Er: ZBLAN fiber laser operating at 2.71–2.88 μm.* Optics letters, 2010. **35**(23): p. 3943-3945.

30. Faucher, D., et al., *20 W passively cooled single-mode all-fiber laser at 2.8 μm.* Optics letters, 2011. **36**(7): p. 1104-1106.

31. Jackson, S.D., A. Sabella, and D.G. Lancaster, *Application and Development of High-Power and Highly Efficient Silica-Based Fiber Lasers Operating at 2$\mu $ m.* IEEE Journal of Selected Topics in Quantum Electronics, 2007. **13**(3): p. 567-572.

32. Ionin, A., *Electric discharge CO lasers.* Gas Lasers, 2007: p. 201-237.

33. Zhdanov, B.V., T. Ehrenreich, and R.J. Knize, *Highly efficient optically pumped cesium vapor laser.* Optics Communications, 2006. **260**(2): p. 696-698.

34. Zweiback, J., A. Komashko, and W.F. Krupke. *Alkali-vapor lasers*. 2010.

35. Nampoothiri, A.V.V., et al., *Molecular C2H2 and HCN lasers pumped by an optical parametric oscillator in the 1.5-μm band.* Optics Express, 2010. **18**(3): p. 1946-1951.

36. Dawson, J.W., et al., *Analysis of the scalability of diffraction-limited fiber lasers and amplifiers to high average power.* Optics Express, 2008. **16**(17): p. 13240-13266.

37. Ratanavis, A., N. Campbell, and W. Rudolph, *Feasibility study of optically pumped molecular lasers with small quantum defect.* Optics Communications, 2010. **283**(6): p. 1075-1080.

38. Chapple, P.B., *Beam waist and M2 measurement using a finite slit.* Optical Engineering, 1994. **33**(7): p. 2461-2466.

39. Standard, I., *Lasers and laser-related equipment-test methods for laser beam widths, divergence angles and beam propagation ratios.* ISO Standard, 2005: p. 11146-2.

40. Fan, T.Y., *Laser beam combining for high-power, high-radiance sources.* IEEE Journal of selected topics in Quantum Electronics, 2005. **11**(3): p. 567-577.

41. Chann, B., et al., *Near-diffraction-limited diode laser arrays by wavelength beam combining.* Optics letters, 2005. **30**(16): p. 2104-2106.

42. Serebryakov, V., et al., *Medical applications of mid-IR lasers. Problems and prospects.* Journal of Optical Technology, 2010. **77**(1): p. 6-17.

43. Chutjian, A. and T.C. James, *Intensity Measurements in the B 3 Π 0 u+− X 1 Σ 0+ g System of I2.* The Journal of Chemical Physics, 1969. **51**(3): p. 1242-1249.

44. Buck, J.A., *Fundamentals of optical fibers*. 2nd ed. 2004, Wiley-interscience.

45. C. Kao and G.A. Hockham, *Dielectric-fibre surface waveguides for optical frequencies* IEEE Proceedings, 1986(133): p. 191-198.

46. Jenkins, F.A. and H.E. White, *Fundamentals of optics*. 1957: New York: McGraw-Hill.

47. Thorlabs, *https://www.thorlabs.com/newgrouppage9.cfm?objectgroup_id=334*.

48. Ranka, J.K., R.S. Windeler, and A.J. Stentz, *Optical properties of high-delta air–silica microstructure optical fibers.* Optics Letters, 2000. **25**(11): p. 796-798.

49. Russell, P.S.J., *Photonic-Crystal Fibers.* Journal of Lightwave Technology, 2006. **24**(12): p. 4729-4749.

50. Renn, M.J., et al., *Optical-dipole-force fiber guiding and heating of atoms.* Physical Review A, 1997. **55**(5): p. 3684-3696.

51. Stone, J., *Optical transmission loss in liquid-core hollow fibers.* IEEE Journal of Quantum Electronics, 1972. **8**(3): p. 386-388.

52. Mach, P., et al., *Tunable microfluidic optical fiber.* Applied Physics Letters, 2002. **80**(23): p. 4294-4296.

53. Kieu, K., et al., *Integrated liquid-core optical fibers for ultra-efficient nonlinear liquid photonics.* Optics Express, 2012. **20**(7): p. 8148-8154.

54. Lopez-Cortes, D., O. Tarasenko, and W. Margulis, *All-fiber Kerr cell.* Optics Letters, 2012. **37**(15): p. 3288-3290.

55. Ohashi, M., K. Shiraki, and K. Tajima, *Optical loss property of silica-based single-mode fibers.* Journal of Lightwave Technology, 1992. **10**(5): p. 539-543.

56. Roberts, P.J., et al., *Ultimate low loss of hollow-core photonic crystal fibres.* Optics Express, 2005. **13**(1): p. 236-244.

57. Alsberg, D.A., J.C. Bankert, and P.T. Hutchison, *WT4 Millimeter Waveguide System: The WT4/WT4A Millimeter-Wave Transmission System.* Bell System Technical Journal, 1977. **56**(10): p. 1829-1848.

58. Garmire, E., T. McMahon, and M. Bass, *Flexible infrared waveguides for high-power transmission.* IEEE Journal of Quantum Electronics, 1980. **16**(1): p. 23-32.

59. Cregan, R.F., et al., *Single-Mode Photonic Band Gap Guidance of Light in Air.* Science, 1999. **285**(5433): p. 1537-1539.

60. Marcatili, E.A.J. and R.A. Schmeltzer, *Hollow Metallic and Dielectric Waveguides for Long Distance Optical Transmission and Lasers.* Bell System Technical Journal, 1964. **43**(4): p. 1783-1809.

61. John, S., *Strong localization of photons in certain disordered dielectric superlattices.* Physical Review Letters, 1987. **58**(23): p. 2486-2489.

62. Benabid, F., *Hollow-core photonic bandgap fibre: new light guidance for new science and technology.* Philosophical Transactions of the Royal Society A: Mathematical, Physical and Engineering Sciences, 2006. **364**(1849): p. 3439-3462.

63. Benabid, F., et al., *Stimulated Raman scattering in hydrogen-filled hollow-core photonic crystal fiber.* Science, 2002. **298**(5592): p. 399-402.

64. von Neumann, J. and E.P. Wigner, *Über merkwürdige diskrete Eigenwerte*, in *The Collected Works of Eugene Paul Wigner: Part A: The Scientific Papers*, A.S. Wightman, Editor. 1993, Springer Berlin Heidelberg: Berlin, Heidelberg. p. 291-293.

65. Couny, F., F. Benabid, and P.S. Light, *Large-pitch kagome-structured hollow-core photonic crystal fiber.* Optics Letters, 2006. **31**(24): p. 3574-3576.

66. Overton, G., *Kagome-- more than a woven basket* Laser focus world 2015. *http://www.laserfocusworld.com/articles/2015/04/kagome-more-than-a-woven-basket.html.*

67. Wang, Y.Y., et al. *Low loss broadband transmission in optimized core-shape Kagome hollow-core PCF*. in *CLEO/QELS: 2010 Laser Science to Photonic Applications*. 2010.

68. Gérôme, F., et al., *Simplified hollow-core photonic crystal fiber.* Optics Letters, 2010. **35**(8): p. 1157-1159.

69. Pryamikov, A.D., et al., *Demonstration of a waveguide regime for a silica hollow - core microstructured optical fiber with a negative curvature of the core boundary in the spectral region > 3.5 μm.* Optics Express, 2011. **19**(2): p. 1441-1448.

70. Kosolapov, A.F., et al., *Demonstration of CO2-laser power delivery through chalcogenide-glass fiber with negative-curvature hollow core.* Optics Express, 2011. **19**(25): p. 25723-25728.

71. Yu, F., W.J. Wadsworth, and J.C. Knight, *Low loss silica hollow core fibers for 3–4 μm spectral region.* Optics Express, 2012. **20**(10): p. 11153-11158.

72. Urich, A., et al., *Flexible delivery of Er:YAG radiation at 2.94 μm with negative curvature silica glass fibers: a new solution for minimally invasive surgical procedures.* Biomedical Optics Express, 2013. **4**(2): p. 193-205.

73. Jaworski, P., et al., *Picosecond and nanosecond pulse delivery through a hollow-core Negative Curvature Fiber for micro-machining applications.* Optics Express, 2013. **21**(19): p. 22742-22753.

74. Jones, A.M., *Realizing a mid-infrared optically pumped molecular gas laser inside hollow-core photonic crystal fiber*. 2012, Kansas State University.

75. Harner, M., *Characterization of the mid-infrared wavelength dependent loss in hollow core photonic crystal fibers*. 2015, Kansas State University.

76. Cisco, *http://www.cisco.com/c/en/us/support/docs/optical/synchronous-digital-hierarchy-sdh/29000-db-29000.html.* 2005.

77. Dadashzadeh, N., et al. *Mode Profile of a Mid-IR Gas-filled Hollow-Core Photonic Crystal Fiber Laser*. in *Frontiers in Optics 2015*. 2015. San Jose, California: Optical Society of America.

78. Dadashzadeh, N., et al. *Near-Gaussian Spatial Mode from a Mid-IR Acetylene-filled Hollow-Core Fiber Laser*. in *Frontiers in Optics 2016*. 2016. Rochester, New York: Optical Society of America.

79. Dadashzadeh, N., et al. *Power-scaling a mid-IR OPA-pumped acetylene-filled hollow-core photonic crystal fiber laser*. in *2016 Conference on Lasers and Electro-Optics (CLEO)*. 2016.

80. Nampoothiri, A.V.V., et al., *Hollow-core Optical Fiber Gas Lasers (HOFGLAS): a review [Invited]*. Optical Materials Express, 2012. **2**(7): p. 948-961.

81. Boyd, R.W., *Nonlinear optics*. 2003: Academic press.

82. Baumgartner, R. and R. Byer, *Optical parametric amplification.* IEEE Journal of Quantum Electronics, 1979. **15**(6): p. 432-444.

83. Myers, L.E., et al., *Multigrating quasi-phase-matched optical parametric oscillator in periodically poled LiNbO3.* Optics Letters, 1996. **21**(8): p. 591-593

.

84. Breunig, I., D. Haertle, and K. Buse, *Continuous-wave optical parametric oscillators: recent developments and prospects.* Applied Physics B: Lasers and Optics, 2011. **105**(1): p. 99-111.

85. Herman, M., et al., *Vibrational Spectroscopic Database on Acetylene, X̃ 1 Σ g+(12 C 2 H 2, 12 C 2 D 2, and 13 C 2 H 2).* Journal of physical and chemical reference data, 2003. **32**(3): p. 921-1361.

86. Maki, A., et al., *Infrared transitions of H 12 C 14 N and H 12 C 15 N between 500 and 10000 cm− 1.* Journal of molecular spectroscopy, 1996. **180**(2): p. 323-336.

87. Lane, R.A. and T.J. Madden. *Energy Loss in Gas Lasers Operating in Hollow-Core Optical Fibers*. in *Proc. of SPIE Vol*. 2017.

88. Wang, Y.Y., et al., *Low loss broadband transmission in hypocycloid-core Kagome hollow-core photonic crystal fiber.* Optics Letters, 2011. **36**(5): p. 669-671.

89. Debord, B., et al., *Hypocycloid-shaped hollow-core photonic crystal fiber Part I: Arc curvature effect on confinement loss.* Optics Express, 2013. **21**(23): p. 28597-28608.

90. Debord, B., et al., *Ultralow transmission loss in inhibited-coupling guiding hollow fibers.* Optica, 2017. **4**(2): p. 209-217.

91. Swann, W.C. and S.L. Gilbert, *Pressure-induced shift and broadening of 1510–1540-nm acetylene wavelength calibration lines.* JOSA B, 2000. **17**(7): p. 1263-1270.

92. Verdeyen, J.T., *Laser Electronics.*

93. Roullard, F. and M. Bass, *Transverse mode control in high gain, millimeter bore, waveguide lasers.* IEEE Journal of Quantum Electronics, 1977. **13**(10): p. 813-819.

94. Standard, I., *11146,"*. Lasers and laser-related equipment–Test methods for laser beam widths, divergence angles and beam propagation ratios, 2005.

95. Clary, D.C., *Product CN Rotational Distributions from the H+ HCN reaction.* The Journal of Physical Chemistry, 1995. **99**(37): p. 13664-13669.

96. Ebenstein, W.L. and J. Muenter, *Dipole moment and hyperfine properties of the ground state and the C–H excited vibrational state of HCN.* The Journal of chemical physics, 1984. **80**(9): p. 3989-3991.

97. Herzberg, G., *Molecular spectra and molecular structure*. Vol. 1. 2013: Read Books Ltd.

98. Siegman, A.E., *An introduction to lasers and masers*. 1971: McGraw-Hill.

99. Kogelnik, H. and T. Li, *Laser beams and resonators.* Proceedings of the IEEE, 1966. **54**(10): p. 1312-1329.